

ABSTRACT

Title of Dissertation: FREE-SPACE OPTICAL COMMUNICATION
LINK ACROSS 16 KILOMETERS TO A
MODULATED RETRO-REFLECTOR
ARRAY

Mark Lewis Plett, Doctor of Philosophy in
Electrical Engineering, 2007

Dissertation Directed By: Professor Julius Goldhar, Department of
Electrical and Computer Engineering

Free-space optical (FSO) links provide secure, high bandwidth data communications. Links to retro-reflectors have the advantage of a simple retro-reflector terminal design. However, the simplicity of the retro-reflector terminal comes at the cost of the complexity of the interrogator terminal. This paper describes a 16 km free-space laser communications link between a high power interrogator terminal and a modulated retro-reflector array at 2 Mbps. This link was the longest high data rate (>1 Mbps) modulated retro-reflector link ever reported at the time this paper was written.

The 16 km free-space optical link to a modulated-retro-reflector was a tremendous technical challenge. The link range was substantially longer than previous similar FSO links. The extreme link range resulted in much higher link losses than incurred on shorter links. The higher link losses were mitigated through interrogator strategies that included a high power Erbium doped fiber amplifier (EDFA) transmitter, an extremely small transmitter divergence, and sophisticated pointing and tracking. To maximize the optical power projected across the link, the transmitter divergence was only 100 μ rad. The small transmitter divergence required stringent optical alignment, and high speed pointing and tracking. The high speed pointing and tracking system was a custom design employing two fast steering mirrors and a tone tracking quadcell detector. The link losses were also mitigated by the use of an array of 3 modulated retro-reflectors. The array both increased the optical link margin as well as reduced the atmospheric channel fading. The interrogator terminal was developed by the author at the Laboratory for the Physical Sciences. The author was also responsible for the link calculations and logistics. The modulated retro-reflector array was developed by researchers at the Naval Research Laboratory under the supervision of William Rabinovich.

This paper describes the 16 km FSO link scenario, the interrogator system, the modulated retro-reflector array, as well as link performance results. The link performance results presented include pointing and tracking performance, channel fading due to atmospheric scintillation, and the communication link performance using various data protocols.

FREE-SPACE OPTICAL COMMUNICATION LINK ACROSS 16 KILOMETERS
TO A MODULATED RETRO-REFLECTOR ARRAY

By

Mark Lewis Plett

Dissertation submitted to the Faculty of the Graduate School of the
University of Maryland, College Park, in partial fulfillment
of the requirements for the degree of
Doctor of Philosophy in
Electrical Engineering
2007

Advisory Committee:
Professor Julius Goldhar, Chair
Professor Christopher Davis
Professor Thomas Murphy
Professor Gilmer Blankenship
Professor Robert Gammon

© Copyright by

Mark Lewis Plett

2007

Dedication

To Rachael.

Acknowledgments

I thank my advisor Dr. Julius Goldhar for his critical assistance in my return to Ph.D. studies. Dr. Goldhar aided me through my entire graduate education and that aide is greatly appreciated. I would like to thank the members of my committee, Dr. Goldhar, Dr. Davis, Dr. Murphy, Dr. Blankenship, and Dr. Gammon for their interest and helpful discussions. I thank Chris Richardson for invaluable input and discussions on this paper.

I would like to thank Norman Moulton, Geroqe Metze, Bernedette Preston, Bill Klomparens, Glen McWright, Andrew Culhane, Cathy Bracey-Tynes, Michael Prin, Marshal Saylors, Barry Barker, and Ken Ritter for their support of my work. I would also like to thank Chris Bles and Thomas Salter.

I would like to thank the FSO team at the Naval Research Laboratory. The NRL team was essential to the completion of my work. Many members of this team suffered through the field work presented here and their contributions are very much appreciated. I thank Will Rabinovich, Rita Mahon, Mike Ferraro, Peter Goetz, Chris Moore, Mena Stell, Michele Suite, and Ray Burris.

Finally, I thank my supportive wife, Rachael, for all she has done to help me during the writing of this dissertation.

Table of Contents

Dedication.....	ii
Acknowledgments.....	iii
Table of Contents.....	iv
List of Tables.....	viii
List of Figures.....	ix
List of Illustrations.....	xiii
Abbreviations.....	xiv
Chapter 1 Introduction.....	1
1.1 Modulated retro-reflector links.....	4
1.2 Carrier wavelength.....	5
1.3 Optical design.....	6
1.4 Pointing and tracking	8
1.4.1 Alignment detectors.....	9
1.4.2 Tracking controller.....	11
1.4.3 Alignment mechanisms.....	11
1.5 Transmitters and receivers	13
1.6 Atmospheric effects.....	14
1.7 Dissertation Overview.....	16
Chapter 2 Link description.....	18
2.1 Link parameters.....	19
2.2 Link budget.....	21

2.3 Link acquisition	28
2.4 Eye-safety.....	31
Chapter 3 Modulated retro-reflector array.....	34
3.1 Cat's-eye modulated retro-reflector.....	35
3.2 Communication system.....	36
Chapter 4 Interrogator system description.....	39
4.1 Transmitter optical train.....	41
4.2 Receiver optical train.....	41
4.2.1 Solar background.....	42
4.2.2 Acquisition cameras.....	43
4.3 Pointing and tracking system.....	44
4.4 Communication system.....	45
4.5 Bi-static versus mono-static optical design.....	46
Chapter 5 Tracking system design.....	51
5.1 Tone tracking.....	53
5.2 Quadrant detector.....	54
5.3 Data converter subsystem.....	61
5.4 Digital signal processor.....	63
5.5 Fast steering mirror.....	64
Chapter 6 Tracking system software design.....	66
6.1 Tone tracking phase locked loop.....	66
6.2 Quadcell automatic gain control.....	71
6.3 Fast steering mirror controller.....	71
6.4 User interfaces.....	82

Chapter 7	Tracking performance.....	85
7.1	Phase-locked loop.....	85
7.2	Quadcell automatic gain control (AGC).....	86
7.3	Pointing mirror control loop.....	89
7.3.1	Pointing mirror time domain controller optimization.....	90
7.3.2	Pointing frequency domain controller optimization.....	94
7.4	Tracking mirror control loop.....	100
7.4.1	Tracking time domain controller optimization.....	100
7.4.2	Tracking frequency domain controller optimization.....	106
7.5	Tracking atmospheric turbulence.....	111
7.6	Link point-ahead performance.....	113
Chapter 8	Atmospheric effects.....	116
8.1	Weather.....	116
8.2	Atmospheric effects measurements.....	119
8.3	Atmospheric attenuation.....	123
8.4	Scintillation statistics.....	124
8.5	Spatial diversity.....	128
8.6	Angle of arrival variance.....	130
Chapter 9	Communications channel performance.....	134
9.1	Video link performance with redundant transmission.....	137
9.2	Half-duplex data link performance.....	138
Chapter 10	Conclusions.....	142
Appendix A	144
Appendix B	148

Appendix C.....	152
Appendix D.....	155
Bibliography.....	158

List of Tables

Table 1.1: Modulated retro-reflector free-space optical link parameters.....	3
Table 2.1: Terminal optical loss budgets.....	21
Table 2.2: Link budget for the 16 km MRR FSO link.....	27
Table 2.3: Laser eye-safety MPE for the IEC 60825.1 and the ANSI136.1 laser safety standards.....	31
Table 4.1: Mono-static design stray light measurements.....	47
Table 4.2: Quadcell sensitivity versus background illumination.....	47
Table 5.1: Quadcell noise contributions and expected signal level for comparison....	59
Table 7.1: Tracking error comparison in the presence of a 5 Hz disturbance.....	103
Table 7.2: Tracking error comparison in the presence of atmospheric angle of arrival error.....	110
Table 8.1: Example METAR data from KNAK (Naval Academy) weather station..	115
Table 8.2: FSO link atmospheric effects data summary.....	119
Table 8.3: Scintillation index and received optical power for 1 to 3 array elements measured on 4 separate days.....	127
Table 8.4: Angle of arrival data statistics.....	130
Table 9.1: Bidirectional link performance statistics.....	138

List of Figures

Figure 1.1: FSO terminal alignment mechanisms.....	12
Figure 2.1: Free-space optical link installation map.....	17
Figure 2.2: Interrogator terminal pointed across the Chesapeake Bay towards Tilghman Island.....	20
Figure 2.3: Calculated diffracted return beam intensity projected on the receiver aperture	24
Figure 2.4: Dynamic RX range loss due to array interference.....	25
Figure 2.5: Rough alignment camera images.....	28
Figure 2.6: Green LED indicates the tracking tone is detected through the fog.....	29
Figure 2.7: IR camera images of retro-reflector target returns.....	30
Figure 3.1: Modulated retro-reflector array installed on Tilghman Island.....	33
Figure 4.1: Interrogator terminal installed at Chesapeake Bay Deployment laser link test range.....	38
Figure 5.1: Quadcell board.....	54
Figure 5.2: Quadcell transimpedance amplifier noise model.....	56
Figure 5.3: Data converter board.....	62
Figure 5.4: Fast steering mirror driver board.....	64
Figure 6.1: Phase locked loop block diagram.....	65
Figure 6.2: PLL lock-in performance for various PLL loop bandwidths.....	67
Figure 6.3: PLL lock-in performance in the presence of noise (SNR = 0.5).....	69
Figure 6.4: Fast steering mirror transfer function Bode magnitude plot.....	74

Figure 6.5: Tracking control loop Bode plots from modeling predictions and measured closed loop tracking performance.....	77
Figure 6.6: Closed loop controller model root locus for loop gain K_o	78
Figure 6.7: Pointing control loop Bode plots from modeling predictions and measured closed loop pointing performance.....	80
Figure 6.8: Pointing and tracking DSP command line interface.....	82
Figure 7.1: Measurement of the phase-locked loop achieving lock.....	83
Figure 7.2: Quadcell AGC performance for various step sizes.....	85
Figure 7.3: Quadcell signal power spectral density plots for various AGC step sizes....	86
Figure 7.4: Open loop fast steering mirror step response.....	88
Figure 7.5: Pointing fast steering mirror step responses for various proportional gain values.....	89
Figure 7.6: Pointing fast steering mirror step response curves for various derivative gain values.....	90
Figure 7.7: Controlled fast steering mirror step response with optimized controller gain settings.....	91
Figure 7.8: Pointing closed loop transfer function for various proportional gain values	94
Figure 7.9: Pointing controller transfer functions for various derivative gain values..	95
Figure 7.10: Pointing controller transfer functions for various overall loop gains.....	96
Figure 7.11: Pointing control loop Bode plots from modeling predictions and measured closed loop pointing performance.....	97
Figure 7.12: Tracking controller step response for various proportional gain values..	99

Figure 7.13: Tracking FSM controller step response curves for various derivative gain values.....	100
Figure 7.14: Tracking disturbance rejection.....	101
Figure 7.15: Tracking compensation power spectral density plots, with tracking (ii), and without tracking (i) for various values of overall loop gain.....	102
Figure 7.16: Tracking closed loop transfer functions for various proportional gains	105
Figure 7.17: Tracking closed loop transfer functions for various derivative gains....	106
Figure 7.18: Tracking closed loop transfer functions for various overall loop gains	107
Figure 7.19: Tracking control loop Bode plots from modeling predictions and measured closed loop tracking performance.....	108
Figure 7.20: Tracking compensation of atmospheric angle of arrival error for various loop gain values.....	109
Figure 7.21: Point-ahead system response to a static pointing error.....	112
Figure 8.1: METAR weather station locations.....	114
Figure 8.2: FSO link atmospheric measurements.....	121
Figure 8.3: Scintillation index and Thomas Point weather buoy data.....	122
Figure 8.4: Scintillation power spectral density curves for various scintillation index values.....	125
Figure 8.5: Received optical signal for various MRR array element counts.....	128
Figure 8.6: Angle of arrival error summary with air-water temperature differential and wind speed as recorded at the Thomas Point weather station.....	131
Figure 8.7: Angle of arrival error power spectral density and cumulative power spectral density.....	132

Figure 9.1: PINFET receiver photodiode sample output.....	133
Figure 9.2: Video link frames transferred across the 16 km MRR FSO link over the Chesapeake Bay.....	135
Figure 9.3: Prerecorded video frame transmitted over FSO link with frame redundancy.....	136
Figure 9.4: Bidirectional data transfer statistics in graphical representation.....	140

List of Illustrations

Illustration 1.1: Modulated retro-reflector free-space optical link diagram.....	2
Illustration 1.2: Bi-static FSO terminal block diagram.....	6
Illustration 1.3: Mono-static FSO terminal block diagram.....	7
Illustration 1.4: Quadcell illumination diagram.....	10
Illustration 1.5: Control loop diagram for FSO tracking system.....	11
Illustration 1.6: FSO beam propagation through atmospheric turbulence.....	15
Illustration 2.1: Modulated retro-reflector FSO link scenario diagram.....	19
Illustration 3.1. Cat's-eye modulated retro-reflector.....	34
Illustration 3.2. Modulated retro-reflector array block diagram.....	36
Illustration 4.1: Interrogator system diagram.....	39
Illustration 4.2: Mono-static interrogator back-end optical system.....	46
Illustration 5.1: Pointing and tracking control system block diagram.....	51
Illustration 5.2: Quadcell amplifier chain block diagram.....	54
Illustration 5.3: Data converter block diagram.....	60
Illustration 5.4: Fast steering mirror driver block diagram.....	64
Illustration 6.1: Tracking control loop diagram.....	72
Illustration 6.2: Pointing fast steering mirror control diagram.....	79
Illustration 7.1: Pointing controller system diagram with measurement test ports.....	93
Illustration 7.2: Tracking control loop diagram.....	104

Abbreviations

ADC	Analog to digital converter
APD	Avalanche photo-detector
CBD	Chesapeake Bay Detachment
CCD	Charge coupled device
CW	Continuous wave
DAC	Digital to analog converter
DFB	Distributed feedback laser
DPSK	Differential phase shift keying
DSP	Digital signal processor
EDFA	Erbium doped fiber amplifier
FOV	Field of view
FSM	Fast steering mirror
FSO	Free-space optics
IR	Infrared
kbps	Kilobits per second
LPS	Laboratory for the Physical Sciences
Mbps	Megabits per second
MPE	Maximum permissible exposure
MRR	Modulated retro-reflector
NHZ	Nominal hazard zone
NRL	Naval Research Laboratory
PCB	Printed circuit board
PID	Controller with proportional, integral, and differential inputs
PLL	Phase-locked loop
PPM	Pulse position modulation
SNR	Signal to noise ratio
TIA	Trans-impedance amplifier
VGA	Variable gain amplifier

Chapter 1 Introduction

Free-space optical (FSO) communication links transmit data by projecting a modulated laser through free-space to an opposing receiver [1][2]. Free-space laser communication links may connect satellites [3], deep-space probes [4], offices [5], and vehicles [6]. Many of the advantages of free-space optical links derive from the extremely high carrier frequency of the communication laser beam. The extremely high carrier frequency enables extremely large antenna gain as well as extremely high data rates [7]. Free-space optical links are often used in scenarios where conventional RF links are undesirable for either bandwidth or interference reasons [8]. Since RF and optical links do not interfere with each other, hybrid links have been proposed to utilize the high link availability of RF links and the high data rate of FSO links [9]. Free-space optical links also provide some secondary advantages such as improved link security, fewer licensing restrictions, and reduced link interference. These unique secondary advantages can often be the deciding factor in the decision to employ an FSO link.

Free-space optical links to modulated retro-reflectors (MRRs) operate differently from standard point-to-point links. Typical point-to-point links use similar terminals on both ends of the link. Links to modulated retro-reflectors are asymmetric links. MRR links are composed of two different terminals. On one end of the link there is the MRR. The opposing terminal is an interrogator. The interrogator projects a CW beam out to retro-reflector. The modulated retro-reflector modulates the CW beam with the input data stream. The beam is retro-reflected back to the interrogator. The interrogator receiver collects the return and reconstructs the

data stream. If bidirectional (duplex) data transfer is desired, a photodetector can be added to the MRR terminal to receive half-duplex data from the interrogator. For bidirectional data transfer, the MRR should only modulate the beam with data when the interrogator beam is CW (no data present). Hence, both terminals share the interrogator beam as the communications channel in a half-duplex manner. A MRR FSO link is shown in Illustration 1.1.

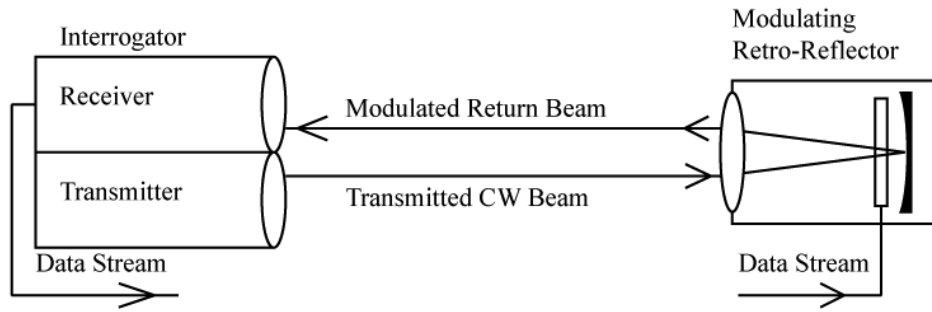


Illustration 1.1: Modulated retro-reflector free-space optical link diagram

The major advantage of the MRR FSO link is the simplicity of the MRR terminal. There is no light source on the MRR side of the FSO link. Further, due to the retro-reflection of the interrogation beam, neither pointing nor tracking is required on the MRR side of the link. The elimination of the transmitter and the tracking make the MRR terminal very simple. A great deal of complexity and electrical power is removed from the MRR terminal and is instead delegated to the interrogator terminal.

This dissertation describes a free-space optical link across 16 km to a modulated retro-reflector array. The terminals used for this link were a modulated retro-reflector array and a high power interrogator. The interrogator terminal

transmitted a 6 W continuous wave (CW) beam at 1550 nm out to the retro-reflector array. The transmitted beam was Class 1M eye-safe due to the large transmitter aperture diameter [10][11]. The modulated retro-reflector array consisted of an array of 3 cat's-eye retro-reflectors which modulated the interrogator beam with a multiple-quantum-well electro-absorption modulator. The array imprinted the data stream on the beam from the interrogator which was then retro-reflected back to the interrogator. The interrogator collected the return beam onto a photoreceiver to complete the data transfer from the MRR array. The interrogator incorporated a bi-static optical design with active pointing and tracking. Listed in Table 1.1 are the major parameters of the FSO link.

Link Range	16 km
Data Rate	2 Mbps
Link Wavelength	1550 nm
Transmitter Power	6 W
Link Margin	13 dB
Receiver Sensitivity (2 Mbps)	-57 dBm
Transmitter Divergence	100 μ rad
Receiver Field of View	150 μ rad
Quadcell Field of View	4 mrad
Coarse Alignment Camera	53 mrad
Fine Alignment Camera	4 mrad

Table 1.1: Modulated retro-reflector free-space optical link parameters

Several cutting edge technologies were used to achieve the highly challenging task of completing the 16 km FSO link. This link employed a novel retro-reflector array in combination with a sophisticated interrogator terminal. The interrogator terminal utilized high-precision pointing and tracking to deliver a high power interrogator beam on the MRR array. This pointing and tracking was made possible

by a highly sensitive quadcell angle sensor. This sensitivity was achieved through phase-locking a 20 kHz tracking tone [7][12]. The combination of the MRR array and the high power interrogator enabled a FSO link that could provide high quality video stream as well as bidirectional data transfers at 2 Mbps. The remainder of this introduction will present the state-of-the-art in the free-space optics technologies relevant to the 16 km FSO link.

1.1 Modulated retro-reflector links

There have been previously demonstrated a variety of retro-reflector FSO links. The most famous retro-reflector link is the moon retro-reflector placed by Apollo 11 [13]. This non-modulated retro-reflector link is the longest laser retro-reflector link deployed. Modulated retro-reflector links have been demonstrated to weather balloons at distances up to 31 km at data rates of 1.2 kbps [14]. Terrestrial MRR data links have only previously been demonstrated up to 7 km [15]. This is due in part to the higher data rates desired for modern data systems. The link presented in this dissertation provided 2 Mbps at 16 km to enable video transmission over the link. This was the longest high speed (>1 Mbps) MRR link reported to date. Previously, short range video links had been presented by a small number of researchers [16][17].

The modulating retro-reflectors used in the 16 km FSO link were cat's-eye multiple-quantum-well modulators [18][19]. Various researchers have presented alternative retro-reflector designs using either acousto-optic modulators [20], electro-optic phase modulators [21], or MEMs modulators [22]. The acousto-optic and electro-optic phase modulators are undesirable for FSO links due to their sensitivity to atmospheric phase errors. The MEMs modulators suffer low reflectivity. The

modulated retro-reflectors developed at NRL have been used successfully in a variety of FSO links [18][19][15].

1.2 Carrier wavelength

The wavelength for the 16 km FSO link was chosen to be 1550 nm for several reason. Primarily, 1550 nm was chosen to provide the capability to use a high power amplifier for the transmitter while still maintaining Class 1M eye-safety [23]. In addition, 1550 nm should provide superior performance in scintillation as opposed to the near-IR wavelengths, 785nm and 850 nm [24]. It has been shown however that fog absorption for the IR and near-IR wavelengths is essentially equivalent [25][26]. Many researcher have investigated long wavelength far-IR wavelengths for use in FSO links [27]. There have been many theoretical studies indicating the potential for reduced fog absorption as well as reduced scintillation at wavelengths longer than 1550 nm [28][29]. These studies have been hotly disputed by conflicting researchers' modeling results [30]. These models are highly dependent on assumptions concerning the fog particulate size. Some empirical measurements have indicated reduced absorption in heavy fog at long wavelengths [31]. However, this reduction in absorption is not sufficient to warrant the use of a wavelength for which the receivers are not very sensitive. Ultimately, the lack of sensitive, high bandwidth, receivers make the long wavelength solutions impractical.

1.3 Optical design

Conventional free-space optical terminals can typically be categorized into two classes. These classes of terminal are bi-static and mono-static optical designs.

Bi-static designs separate the transmit and receive optical paths as shown in Illustration 1.2. The advantage of a bi-static optical design is the large amount of optical isolation provided by the separate transmit and receive optical paths. The primary disadvantage of a bi-static optical system is that the pointing and tracking of the transmit and receive beams must be done either via gimbals for the entire terminal or through duplicate beam correction optics. Bi-static optical terminals are the most common FSO terminal designs due to the simplicity of the design.

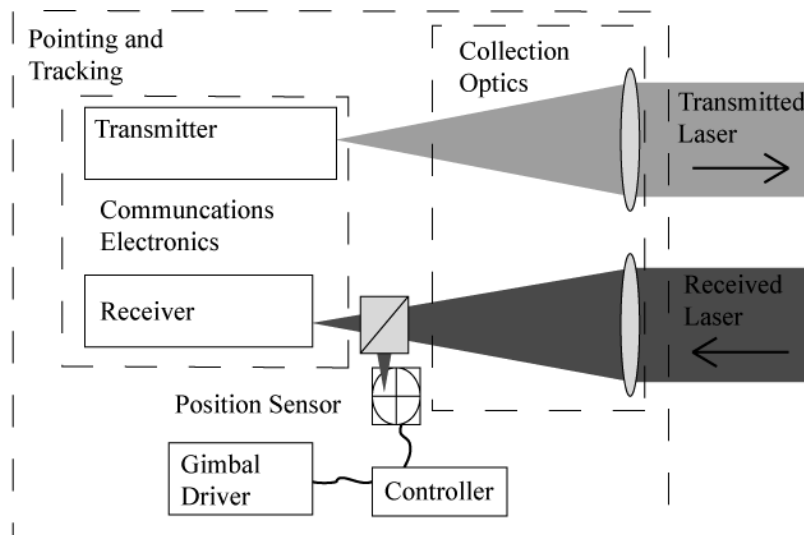


Illustration 1.2: Bi-static FSO terminal block diagram

Mono-static optical designs employ a common optical path for the transmit and receive beams across the link. The transmit and receive beams are internally separated through either wavelength, time, or polarization division [32]. The primary advantage of a mono-static optical system is an inherent co-alignment of transmitter and receiver beams which enables high bandwidth (accurate) pointing through accurate tracking. Depicted in Illustration 1.3 is a mono-static FSO terminal that

employs a fast steering mirror to provide the simultaneous high accuracy pointing and tracking. A disadvantage of a mono-static terminal design is the increased complexity of the optical design relative to a bi-static design. Also, sufficient optical isolation of the transmit and receive beams can be difficult to achieve. Mono-static designs are often employed in more sophisticated FSO terminals such as employed in inter-satellite links. The improved pointing and tracking performance of mono-static designs is often a desired attribute in long range link terminals due to their reduced transmit beam divergence.

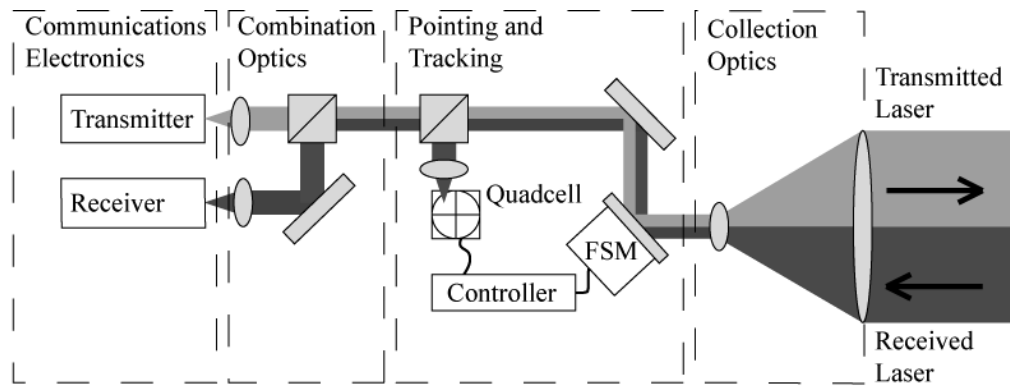


Illustration 1.3: Mono-static FSO terminal block diagram

The interrogator terminal was chosen to be a bi-static optical design. A mono-static design was initially favored for the interrogator for the improved pointing and tracking performance. However, optical isolation issues forced the optical design to be changed to a bi-static design. The choice of optical design will be described in detail in Chapter 4.

1.4 Pointing and tracking

Pointing and tracking is a vital component to FSO terminals. The high antenna gain (low beam divergence) requires accurate pointing and tracking to maintain the alignment of the link laser. Most pointing and tracking system employ an alignment detector to detect the angle of arrival of the incoming beam. The angle of arrival error is processed by a controller to determine the required beam correction to maintain link alignment. The beam correction is usually achieved by moving an optical element such as a fast steering mirror or using gimbals to move the entire optical terminal.

There is a great body of research on laser tracking techniques [33][34]. A great deal of this research relates to target tracking for laser weapons [35][36]. These systems employ advanced imaging systems for target identification and tracking [37][38]. The tracking system employed for the 16 km link more closely resembles the style of tracking system employed for inter-satellite [39] and high altitude air-to-air laser communications links [40][41]. These links have small divergence transmitters and additional point-ahead fast steering mirrors similar to the 16 km interrogator terminal [42][43].

The requirements for the pointing and tracking system was derived from the expected vibration and atmospheric turbulence environments. The terminal base motion due to vibration may be as high as 25 μrad [44]. The frequency content in various installation environments is typically around 10 Hz [44][45]. Atmospheric tip tilt is typically 15 μrad and may be as large as 100 μrad [46][24]. The frequency content of this error is typically 10 Hz but may be as high as 100 Hz [47][48]. The

closed loop tracking bandwidth of the 16 km interrogator was 125 Hz to compensate both base motion vibration and atmospheric turbulence. This bandwidth is similar to that found in commercial FSO terminals [49].

1.4.1 Alignment detectors

Alignment detectors are sensors that detect the error in the optical alignment of the link. These sensors include quadrant detectors [50], lateral effect cells [51], CCD arrays, inertial sensors, and beam nutation [34]. Most alignment detectors convert a focal plane intensity distribution into signals relating to the alignment of the link. The angle of arrival error, θ_{Az} , is related to the focal plane displacement (Δx) by equation (1.1), where F is the effective focal length of the receiver optics. A commonly employed alignment sensor is the quadrant detector. The quadrant detector, or quadcell, is commonly employed due to its relatively high sensitivity and bandwidth.

$$\theta_{Az} = \frac{\Delta x}{F} \quad (1.1)$$

Quadrant detectors output 4 signals proportional to the received optical power on a 2x2 array of photo detectors. Depicted in Illustration 1.4 is a received beam focused into a spot on a quadcell displaced in the focal plane. The normalized centroid of the received optical power can then be approximated by equations (1.2) and (1.3). These equations are often referred to as the quadcell math equations. Equation (1.2) determines the azimuth quadcell error and equation (1.3) determines the elevation quadcell error.

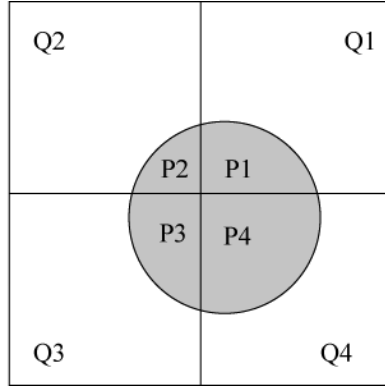


Illustration 1.4: Quadcell illumination diagram

$$E_{Az} = \frac{(P_1 + P_4) - (P_2 + P_3)}{(P_1 + P_2 + P_3 + P_4)} \quad (1.2)$$

$$E_{El} = \frac{(P_1 + P_2) - (P_3 + P_4)}{(P_1 + P_2 + P_3 + P_4)} \quad (1.3)$$

The optical sensitivity of the tracking sensor can be augmented through tone tracking.[7] Tone tracking employs a low frequency tone modulated onto the laser to differentiate the link laser from the solar background. The tone modulation is made small so as to minimize any effect on the data. A tone tracking system uses coherent detection of the tracking tone thereby enabling much greater sensitivity than direct DC tracking.

1.4.2 Tracking controller

The basic feedback control diagram for a FSO tracking system is illustrated in Illustration 1.5. There are several controller implementations that could be used to close the feedback from the alignment sensor to the alignment mechanism.[50] The

pointing and tracking for the 16 km link was performed with a classic Proportional-Integral-Derivative (PID) controller [52]. The PID was relatively simple and the second order nature of the PID is convenient for the control of second order mechanisms such as fast steering mirrors and gimbals.

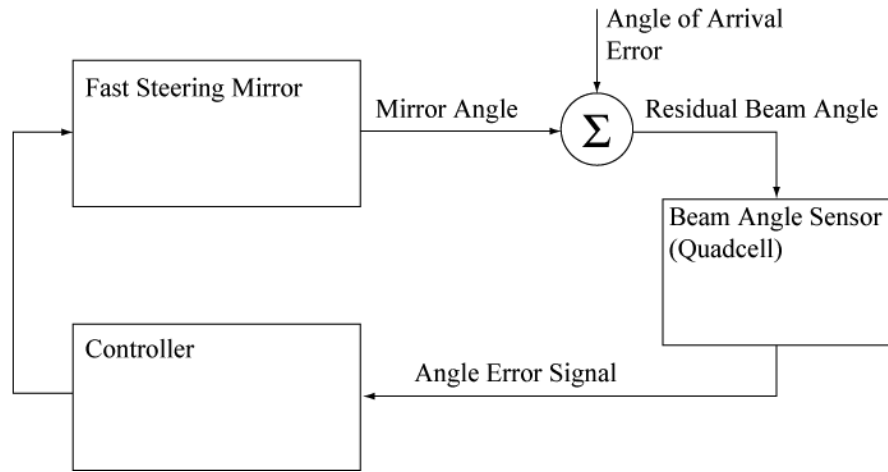


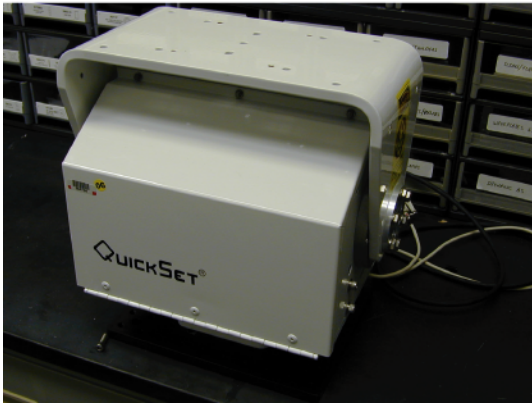
Illustration 1.5: Control loop diagram for FSO tracking system

1.4.3 Alignment mechanisms

There are many technologies that can be used for link alignment mechanisms. These technologies can be classified into two major categories; mechanical and electro-optical. Mechanical alignment mechanisms position an optical element to correct the beam alignment. Mechanical alignment mechanisms include gimbals and fast steering mirrors [53]. Gimbals are typically used for slower pointing requirements and are used to manipulate the entire terminal [54][55]. Fast steering mirrors are integral to the terminal optical design and are used for faster (>1 Hz) pointing and tracking requirements [56]. Shown in Figure 1.1 are gimbals and a fast

steering mirror. The interrogator terminal was equipped with two Newport FSM-320 fast steering mirrors to correct high speed vibration and atmospheric disturbances. Manual gimbals were used for coarse terminal pointing.

a) Gimbals for FSO terminal



b) Fast steering mirror

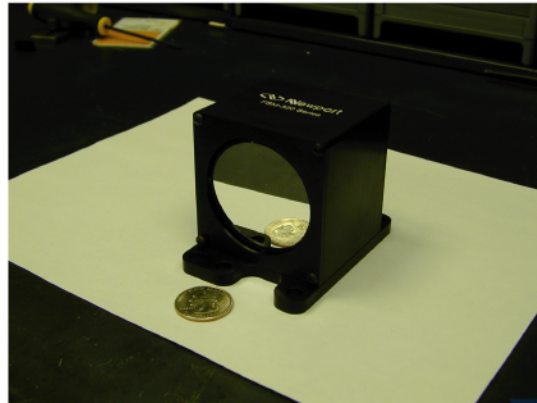


Figure 1.1: FSO terminal alignment mechanisms

a) Gimbals, b) Fast steering mirror

Electro-optical alignment mechanisms may also be employed to adjust the beam alignment without mechanically moving optics. Electro-optical alignment mechanisms include Bragg cells (acousto-optical actually, but still no moving parts) and liquid crystal spatial light modulators. These mechanisms are often used when high reliability is important to the terminal design. Mechanical mechanisms are more often used due to lower costs [38].

1.5 Transmitters and receivers

Free-space optical links typically employ fiber optic photonic components for the transmitter and receiver. This is due to the low cost and high reliability of these parts. Free-space transmitters are typically DFB or Fabry-Perot laser diodes. Erbium

doped fiber amplifiers (EDFAs) may be used for additional transmit power. The interrogator terminal employed a tunable laser and a 20 W EDFA for the transmitter. A typical goal of free-space transmitters is to provide a large amount of signal while minimizing the spatial coherence of the beam. Reduced spatial coherence mitigates undesirable coherence effects (scintillation) on beams propagated through the atmosphere. This coherence reduction is typically done via multiple transmitters, low coherence sources (LEDs), or mode scramblers (multi-mode fiber) [57].

Free-space receivers are typically avalanche photodiodes (APDs). These detectors are often used in the fiber optics industry for their excellent sensitivity and bandwidth. APDs are small ($<200\text{ }\mu\text{m}$) to provide high bandwidth. Therefore, focusing all the collected light onto the APD is a challenge for free-space optical receiver design. Various optical designs have been employed to maximize the light collection onto small detectors. These designs include focal reducing optics and non-imaging optics. The interrogator terminal had a $100\text{ }\mu\text{m}$ core fiber coupled PINFET receiver.

Free-space optical links are physical layer links and many communication protocols and modulation formats have been employed over these links. On-off keying (OOK) is the most common modulation format [58]. OOK was the modulation used on the 16 km FSO link. Pulse position modulation (PPM) and differential phase shift keying (DPSK) are also employed in FSO links [59][60]. OOK is typically used for higher data rates while PPM is used for lower rates in strong background environments. In addition to the traditional modulation formats, a

few novel formats have been proposed specifically for FSO links. These modulations include polarization encoding and time delayed redundancy [61][62].

1.6 Atmospheric effects

Atmospheric effects complicate the design of all terrestrial free-space links. Atmospheric effects cause both static and dynamic losses. The static losses in the atmosphere come from molecular absorption as well as scattering losses. The dynamic losses can be due to changing aerosol content like fog, rain and snow, or coherent effects like scintillation. Atmospheric turbulence induced scintillation can greatly increase the bit error rate (BER) of the FSO link [58][63]. The characteristic time scales of the dynamic losses vary greatly. Fog causes losses that vary over hours and scintillation can cause sudden signal fades as fast as a millisecond.

Scintillation is the result of the coherent addition of light traversing various paths through the turbulent atmosphere. These various paths are created by packets of air with varying temperature that act as lenses in the beam path. This concept is depicted in Illustration 1.6. The coherent addition of the light traversing the various paths creates constructive and destructive interference at the receiver. Thus, scintillation results in dynamic changes in the received optical power that must be accounted for in the link margin.

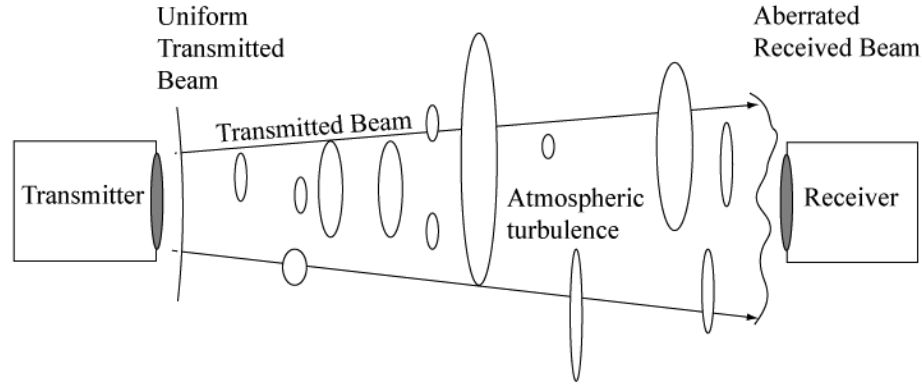


Illustration 1.6: FSO beam propagation through atmospheric turbulence

There are several approaches to mitigating atmospheric scintillation. The most common, aperture averaging, averages out the scintillation by receiving a spatially large portion of the beam [64]. Spatial diversity is employed both in the MRR array design and in the interrogator design. The MRR array elements are separated so as to reduce scintillation [65]. It has been shown in several references that scintillation can be mitigated by averaging its effect over a large receiver aperture [64][66][67]. Large transmit and receive apertures (8 inch) were designed into the the interrogator terminal to reduce scintillation [68].

The most sophisticated scintillation mitigation technology is adaptive optics. Adaptive optics use phase correcting optics to mitigate the phase effects of the atmosphere [69][70]. Adaptive optics are complicated and expensive to implement. Further, adaptive optics typically can only offer marginal link performance improvement [71]. Some researchers have proposed novel scintillation reduction schemes based on reducing the spatial coherence with a multi-mode fiber transmitter [57]. Further, the use of EDFA pre-amplifiers used in saturation has been proposed to limit the scintillation signal variations [72].

1.7 Dissertation Overview

The goal of this dissertation was to complete the longest MRR FSO link ever achieved with a data rate greater than 1 Mbps. To achieve this link the author designed a high performance interrogator terminal. The specifications for this terminal were defined by the author through a detailed link budget analysis. The requirements for the interrogator terminal derived from the link budget were highly stringent. The very small divergence and very high transmit power requirements necessitated the highest level of FSO terminal design. To achieve these stringent specifications the author designed and built a highly precise optical system for beam projection and collection. In addition to advanced optical design, the interrogator terminal required a sophisticated pointing and tracking system. This system was designed and implemented entirely by the author. This design included the design and fabrication of a highly sensitive quadcell detector circuit. Also required was the design and implementation of a sophisticated digital tone tracking fast steering mirror controller. In addition to specifying, designing, and fabricating the interrogator terminal, the author was also responsible for the field installation and successful operation of the 16 km link.

Although the author's contribution was great, the MRR FSO link could not have been completed with the support of the Naval Research Laboratory. The NRL FSO team which provided the MRR array and the communications electronics. In addition, Rita Mahon and Mike Ferraro provided link deployment support during link testing. The support of the NRL is greatly appreciated.

Chapter 2 Link description

The 16 km free-space optical retro-reflector link was deployed by the author at the U.S. Naval Research Laboratory's Chesapeake Bay Deployment (CBD) laser test range [73][74]. This laser link test range consists of two sites in Maryland, one at Chesapeake Beach, and the other on Tilghman Island. Tilghman Island has a direct line of sight with Chesapeake Beach 16 km across the Chesapeake Bay. The beam path was almost entirely over water at a height of about 100 feet. The link is illustrated on the map of Maryland in Figure 2.1.

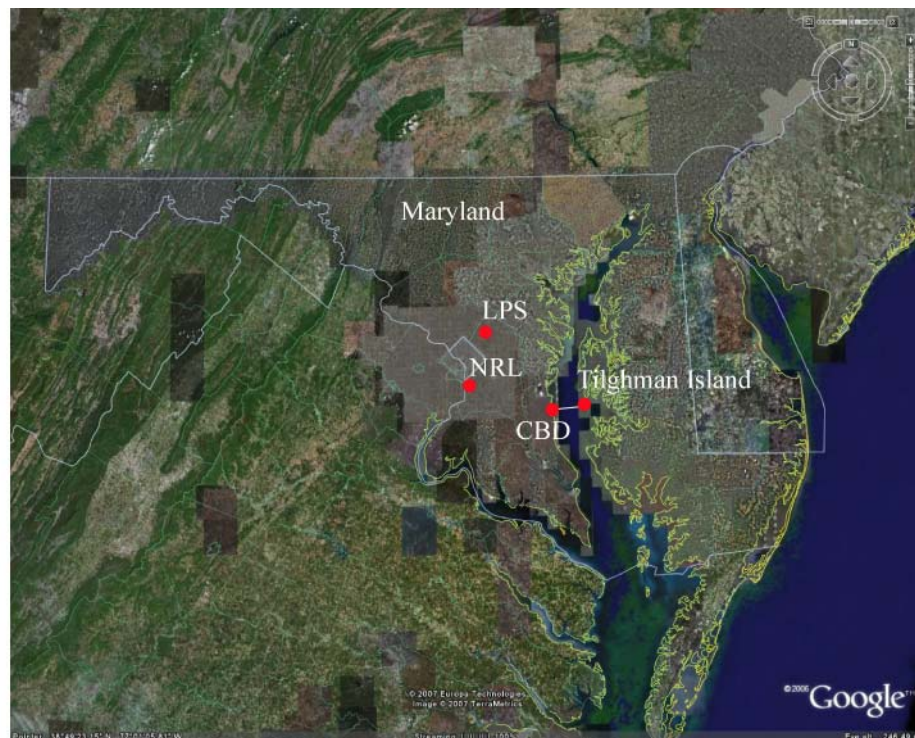


Figure 2.1: Free-space optical link installation map

The link testing was performed from September 6th 2006 until November 27th 2006. The link was available for testing for 12 days during this period. This was due primarily to link range scheduling and weather. The link was deployed on September 6th. On September 8th link acquisition was completed. An alignment problem in the receiver optics resulted in initially low received optical power for the link. The alignment was corrected during four days of the following two weeks. On September 20th, the communications link passed data for the first time. There were 11 subsequent (non-consecutive) days of link testing. This link testing included: scintillation measurements, data throughput measurements, and pointing and tracking measurements.

2.1 Link parameters

The modulated retro-reflector array was set-up in a room on a radar tower on Tilghman Island. The room is approximately 10 meters off the ground. The MRR array was approximately 15 meters above the water level. Initially, the array was located behind a window. Link measurements indicated that this window was causing 3 dB of link loss. Subsequently, the link was operated with the window open for the remainder of the testing to avoid this 3 dB loss. The link is depicted in Illustration 2.1.

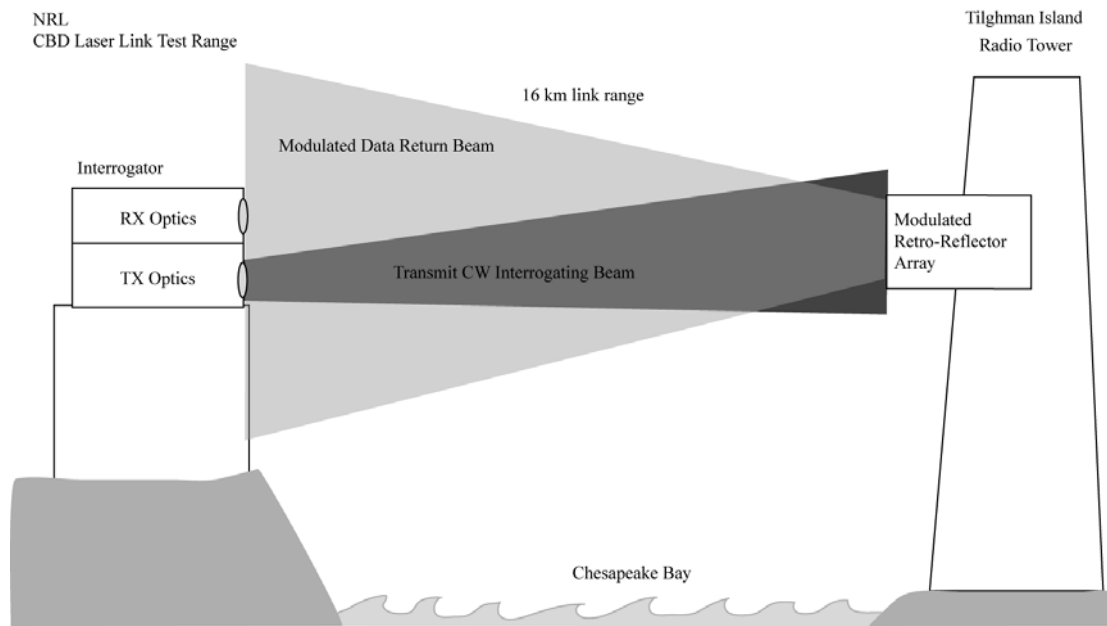


Illustration 2.1: Modulated retro-reflector FSO link scenario diagram

The interrogator terminal was setup inside a building at the Chesapeake Bay Deployment facility. The interrogator was set on an optical table next to an open window facing Tilghman Island. The interrogator was approximately 2 meters above the ground. The ground level was approximately 30 meters above the water level at the CBD side of the link. The majority of the link was approximately 20 meters above the Chesapeake Bay. Pictured in Figure 2.2 is the interrogator system pointed out the window of the CBD facility.



Figure 2.2: Interrogator terminal pointed across the Chesapeake Bay towards Tilghman Island

2.2 Link budget

An FSO link cannot be successful without a balanced link budget. The link budget is a tabulation of the optical power losses in the link. The link budget is bounded by the system dynamic range given by the transmitter output power and the receiver sensitivity. After subtracting all the optical losses across the link, any remaining dynamic range is referred to as the link margin. The excess dynamic range that is the link margin allows a link to operate under adverse conditions such as fog, rain, vibration, and atmospheric turbulence.

The first loss term in the link budget was the loss associated with the optics in the transmitter. The reflection and absorption losses of all the optical elements in the

transmitter were lumped into a single transmitter (TX) optics loss term. A similar accounting of optical losses was comprised for the receiver (RX). Table 2.1 lists the optical losses of the interrogator terminal transmitter and receiver optics. This table was compiled from the optics specifications and verified through measurement. The receiver had an additional optical loss due to the coupling of the signal into an optical fiber. The receiver coupling loss was due to imperfect coupling of the received optical power into the 100 μm photoreceiver input optical fiber.

TX Optics	Loss [dB]	RX Optics	Loss [dB]
Fold Mirror	-0.15	Schmidt Corrector	-0.15
Beam Expander	-0.30	Primary Mirror	-0.15
Fold Mirror	-0.15	Secondary Mirror	-0.15
Fast Steering Mirror	-0.15	Collimating Lens	-0.15
Decollimating Lens	-0.15	Fast Steering Mirror	-0.15
Secondary Mirror	-0.15	Beam Splitter	-3.50
Primary Mirror	-0.15	Bandpass Filter	-2.20
Overfill Loss	-3.85	Focusing Lens	-0.15
Schmidt Corrector	-0.15		
TX Total Optics Loss	-5.2	RX Total Optics Loss	-6.6

Table 2.1: Terminal optical loss budgets

There are three loss terms associated with the modulated retro-reflectors. The first is the absorption loss. The second, wavefront loss, is a loss associated with the imperfection of the retro-reflector optics. The third retro-reflector loss, contrast ratio, is the loss due to the 50% modulation depth of the quantum-well modulator.

The RX and TX atmospheric absorption losses are due to scattering and absorption from the gases in the atmosphere. This loss can easily be expressed in a

single loss term in units of dB/km. For the 16 km link budget, a high visibility absorption coefficient of 0.3 dB/km was assumed.[75][1]

The RX and TX range loss terms account for the beam divergence on each end of the link. The TX range loss comes from the overfilling of the projected power onto the retro-reflector apertures by the transmitted beam divergence. The projected power is calculated in equation (2.1) from the overlap of the project beam footprint, $H(x,y)$, and the aperture function of the MRR array, $M(x,y)$. The interrogator projected a circular beam footprint, $H(x,y)$, that was approximately 1 m in diameter onto the MRR array. The interrogator beam footprint was validated experimentally.

$$Projected\ Power = \iint_M M(x, y) H(x, y) dx dy \quad (2.1)$$

The MRR array aperture function was composed of three 16 mm apertures arranged in a triangle with a 30 cm separation. Rather than a single large retro-reflector, an array of retro-reflectors was required because the field of view (FOV) of a MRR is reduced when the aperture size is increased. The MRR FOV is describe in Section 3.1 Due to the aperture size restriction, an array was necessary to achieve a large reflective area.

The RX range loss comes from the return beam, $F(x,y)$, overfilling the receiver aperture, $R(x,y)$. The power collected by the receiver is calculated with equation (2.2) from the overlap integral of $R(x,y)$ and $F(x,y)$. The return beam footprint was approximately 4 m in diameter due to the diffraction from the 16 mm retro-reflector

apertures. The receiver aperture function was an 8 inch telescope circular aperture with a 2.5 inch central obscuration.

$$Collected\ Power = \iint_R R(x, y) F(x, y) dx dy \quad (2.2)$$

In the absence of atmospheric effects, the beam propagation across the link can easily be predicted using Fourier techniques. Diffraction effects are particularly important in the choice of the element spacing in the MRR array. The 30 cm array separation was chosen to mitigate the interference of the three elements on the interrogator receiver collection aperture. The fringe spacing, S , from two MRRs is given in equation (2.3). The element spacing, d , can be chosen to provide two fringes across the receiver aperture. This ensures that the receiver is never solely in a null of the interference pattern. Further increasing the array spacing beyond two fringes will incur increased link loss as the array elements will no longer be positioned near the maximum of the projected beam intensity. The size of the projected interrogator beam footprint is the absolute limit on the array spacing.

$$S = \frac{\lambda}{d} * R \quad (2.3)$$

The exact projected diffraction pattern can be calculated using the Fraunhofer diffraction expression given in equation (2.4).

$$F(x, y) \propto \iint_M M(x, y) \exp(ikx +iky) dx dy \quad (2.4)$$

The Matlab script provided in Appendix A was used to evaluate this transform numerically to yield the projected return from the MRR array. Plotted in Figure 2.3 is the calculated beam intensity pattern projected on the receiver aperture by the MRR array. The central dark region is the secondary mirror obscuration of the Cassagrain receiver telescope. The six dark bands are the interference nulls from the coherent return from the 3 retro-reflectors. The center lobe of the pattern is blocked by the secondary mirror of the Cassagrain receiver collection telescope.

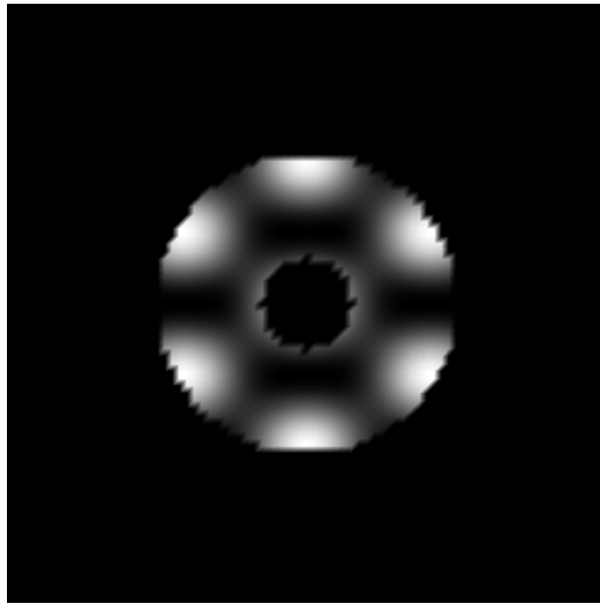


Figure 2.3: Calculated diffracted return beam intensity projected on the receiver aperture

Minor angular vibration of the MRR array will phase shift the elements of the array causing a translation of the projected fringe pattern. This translation will result in a time varying link loss. Plotted in Figure 2.4 is the RX range loss as a function of the phase angle between the elements of the array. The 2π range of phase shift ensures that the loss was calculated over the translation of an entire fringe. As can be

seen in Figure 2.4, the choice of element separation ensured that the vibrational effect of the array on the range loss would be minimal.

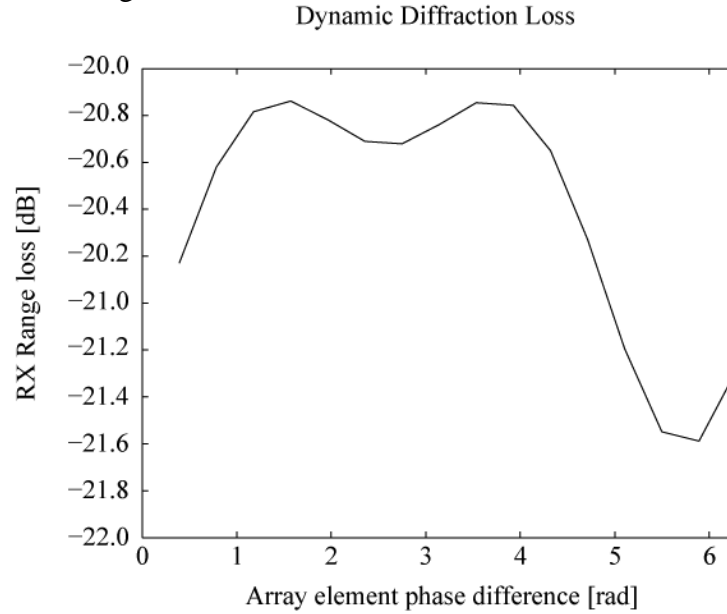


Figure 2.4: Dynamic RX range loss due to array interference

The preceding calculation of link diffraction is mainly important on links with very little atmospheric scintillation. When the atmospheric scintillation is strong, the phase effects of the atmosphere overwhelm the phase effects of the array. Due to the strong scintillation of the 16 km FSO link, the diffraction effects could not be measured from link performance. However, this merely indicates that the spacing was appropriate to mitigate the diffraction. It is better to remove the diffraction problem through proper engineering rather than hoping for favorable atmospheric conditions.

The complete link budget for the 16 km link is listed in Table 2.2. This link budget uses the diffracted beam profiles to determine RX and TX range losses. The RX range loss was averaged over array phase angle. The link budget predicted a link

margin of 12.8 dB. The measured link margin varied between 16 and 7 dB depending on the visibility and atmospheric scintillation. The wide variability in atmospheric absorption (visibility) makes accurate link margin predictions very difficult. A mere 0.75 dB/km change in visibility is all that is required for the link margin to go from 13 dB to 0 dB.

The tracking link budget is also listed in Table 2.2. It is important to tabulate both a communications link budget and a tracking link budget. This is necessary to ensure that the tracking system has enough signal to track effectively even when the signal is below the sensitivity of the communication detector. The tracking system uses a 20 kHz tone to track the received interrogator beam in the presence of solar background light. The transmit power for the tracking channel is reduced by 8.2 dB from the communications channel to account for the 15% modulation depth of the tracking tone. The 20 kHz tone used for the tone tracking system uses only a small modulation to minimize its impact on the communication channel. Tone modulation less than 15% yields a communications channel power penalty that is less than 1 dB. It can be seen in Table 2.3 that the tracking channel has 6.5 dB more link margin than the communication channel.

The sensitivity listed for the tracking system is -63 dBm. This is the signal level at which effective tracking can still be accomplished. The sensitivity of the tracking PLL is even lower at -67 dBm. Therefore, the tracking tone can be detected with significantly less light than required for data reception. This was designed into the system to ensure the tracking would perform even as the communication channel failed. The quadcell sensitivity will be discussed in detail in Chapter 5.

<u>Link Item</u>	<u>Units</u>	<u>Communications Link</u>	<u>Track Link</u>
TX Power	[dBm]	43	34.8
TX Optics Loss	[dB]	-5.2	-5.2
TX Range Loss	[dB]	-34.4	-34.4
TX Atmospheric Absorption	[dB]	-4.8	-4.8
MRR Loss	[dB]	-2.0	-2.0
MRR Wavefront Loss	[dB]	-1.0	-1.0
MRR Contrast Loss	[dB]	-3.0	-1.2
RX Range Loss	[dB]	-20.6	-20.6
RX Atmospheric Absorption	[dB]	-4.8	-4.8
RX Optics Loss	[dB]	-6.6	-6.6
RX Coupling Loss	[dB]	-4.8	0
RX Power	[dB]	-44.2	-43.6
RX Sensitivity	[dBm]	-57	-63
Link Margin	[dB]	12.8	19.4
Actual Margin	[dB]	16 to 7	

Table 2.2: Link budget for the 16 km MRR FSO link

2.3 Link acquisition

Link acquisition can be one of the most challenging aspects of free-space optical links. This is due to the small beam transmitter divergence and small field of view of the receiver. For this reason, secondary large field of view detectors are often integrated into FSO systems. To facilitate the 16 km link acquisition, coarse and fine alignment cameras were integrated into the system. The coarse link alignment was accomplished with a wide field of view (FOV) camera. The transmitted beam was co-aligned to the camera crosshairs in the lab. This enabled the transmitter to be properly pointed at the MRR array by lining up the crosshairs on the opposite end of the link. There is a large lamp on the Tilghman Island tower close to the target

modulated retro-reflector array. This lamp was imaged on the alignment camera and facilitated the pointing of the transmitted laser to the modulated retro-reflector array. The lamp light can be seen in Figure 2.5 as a bright smear just to the left of the center of the crosshairs.

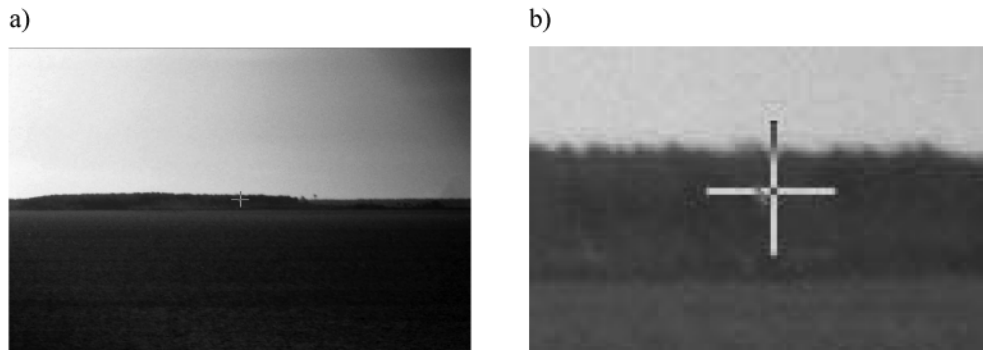


Figure 2.5: Rough alignment camera images
a) Entire camera view, b) Zoomed image of crosshairs

Once the transmitter was aligned, the tracking DSP phase-locked loop acquired the 20 kHz tracking tone. This lock was the first indicator that light was successfully being sent across the link. Pictured in Figure 2.6 is the image of the PLL lock indicator LED on the interrogator. This image was taken on a foggy day and the tracking tone was still detected. Comparing Figures 2.2 and 2.6 demonstrates the diversity of visibility that may occur on the link.

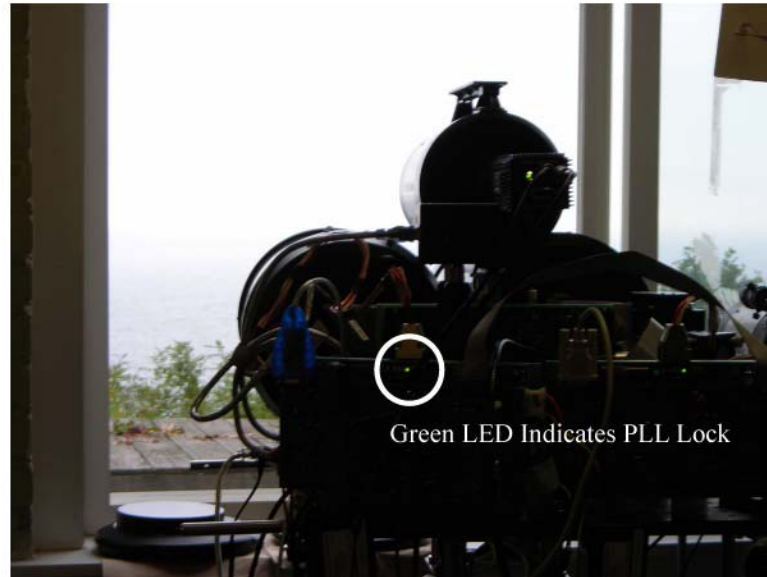


Figure 2.6: Green LED indicates the tracking tone is detected through the fog

The final link acquisition tool was the narrow field of view IR camera. This camera was a Sensors Unlimited IR CCD. This camera was used to image the return from the retro-reflector array. In addition to the MRR array, there were two passive retro-reflector targets on the Tilghman Island tower. These passive retro-reflectors were a three inch corner cube and an array of 25 two inch corner cubes. The retro-reflector targets were all spaced such that the interrogator transmitter would not be able to illuminate more than one at a time. Pictured in Figure 2.7 are the images of the returns from the three retro-reflector targets imaged by the IR camera.

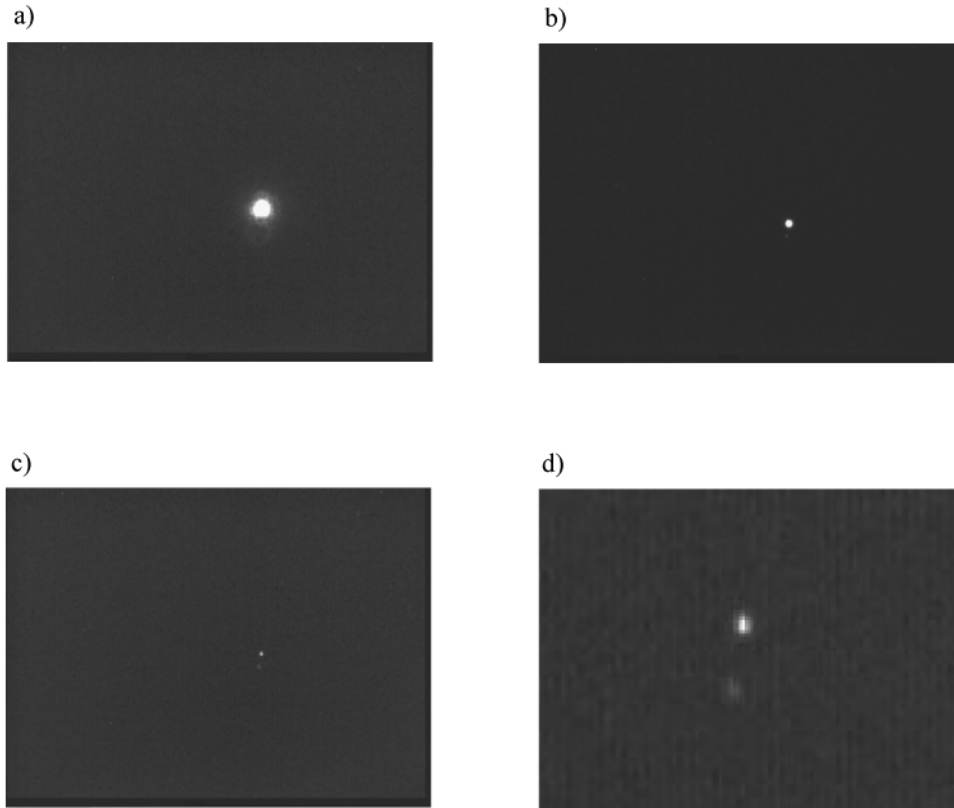


Figure 2.7: IR camera images of retro-reflector target returns
a) 25-array of 2 inch corner cubes, b) 3 inch corner cube, c) MRR array, d) MRR array (zoomed)

2.4 Eye-safety

The interrogator terminal was designed to be eye safe. The two eye-safety standards used in determining the eye-safety of the link were the ANSI Z136.1 and the IEC 60825.1 laser safety standards. The emitted irradiance of the interrogator terminal was 21 mW/cm^2 . This emitted irradiance was less than the IEC 60825 Class 1M maximum permissible exposure (MPE) and less than the ANSI Z136.1 Class 1 unaided viewing MPE limit.[11] Based on these limits the interrogator beam was

safe for viewing to the naked eye. However, the emitted irradiance exceeded the ANSI Z136.1 Class 1 aided viewing MPE limit. Aided viewing is the use of binoculars or other optics to concentrate the emitted irradiance. The IEC Class 1M classification acknowledges the potential for unsafe aided viewing of the laser beam. However, Class 1M provides a classification that is less restrictive than the ANSI Class 3b. Class 1M is specifically intended for the installation of systems for which aided viewing is unlikely but not prohibited. The IEC Class 1M classification has become the standard used for most commercial FSO terminals.[75] Listed in Table 2.3 are the MPE limits from the ANSI Z136.1 and the IEC 60825.1 standards for both aided and unaided viewing of the laser beam.

Standard	Class	Unaided Viewing MPE [mW/cm²]	Aided Viewing MPE [mW/cm²]
ANSI Z136.1	Class 1	100	2
ANSI Z136.1	Class 3b	5197	104
IEC 60825	Class 1	26	2
IEC 60825	Class 1M	104	104
Interrogator Irradiance		21	

Table 2.3: Laser eye-safety MPE for the IEC 60825.1 and the ANSI136.1 laser safety standards

The IEC Class 1M eye safety classification is considered eye-safe under all reasonably foreseeable conditions. This is not as benign as the IEC Class 1 eye-safe classification which is considered safe under all usage conditions. This being the case, certain laser safety control measures were put in place to further reduce the chances of unforeseeable usage conditions that might cause an unsafe situation with the Class 1M emission from the interrogator.

Since there was the potential for unsafe aided viewing of the laser, it was necessary to define a Nominal Hazard Zone (NHZ). The NHZ is the region of space in which aided viewing of the laser would be unsafe. Since the transmitter is diverging, the optical irradiance decreases as the beam spreads out across the link. At a certain range, the optical irradiance drops below the ANSI Z136.1 Class 1 eye-safety limit. The region surrounding the beam up to this range is the Nominal Hazard Zone (NHZ). The NHZ is a rectangular box extending 2000 m out from the CBD facility, 30 m above the water and no more than 5 meters on a side surrounding the beam. Although the NHZ extends a reasonable distance over the bay, the size of the NHZ is very small and located high above the water level. Outside the NRH the optical irradiance is within the ANSI Z136.1 Class 1 limit.

To minimize the risk of exposure in the NHZ, the laser was never operated unattended. Additionally, the portion of the NHZ that was over land at CBD was roped off and marked with appropriate warning signs. The added safety measures ensured that no-one could enter the NHZ unnoticed. If ever anyone did enter the NHZ, the laser could be disabled by the operator. These safety measures are not strictly required by the IEC standard for Class 1M laser systems. However, these measures are recommended by both the IEC and the ANSI standards for outdoor laser use.

Chapter 3 Modulated retro-reflector array

The modulated retro-reflector array used in the 16 km FSO link was developed by researchers at the Naval Research Lab under the direction of William Rabinovich. The retro-reflector array system consists of three main components. The three main components are the modulated retro-reflectors (MRR), the data compressor, and the data source. The data compressor encodes data for the MRR from either a camcorder or a laptop computer. The modulated retro-reflectors are refractive cat's-eye retro-reflectors. The retro-reflector array consists of three modulated retro-reflectors, each with an aperture diameter of 16 mm. These retro-reflectors were mounted in a triangular configuration with a separation of 30 cm. Pictured in Figure 3.1a is a photograph of the front of the MRR array. In this photograph, the three MRR apertures mounted in a triangle can be seen. Pictured in Figure 3.1b is the backside of the MRR array. The three round MRR drivers and the data compressor (center) can be seen in this backside view.

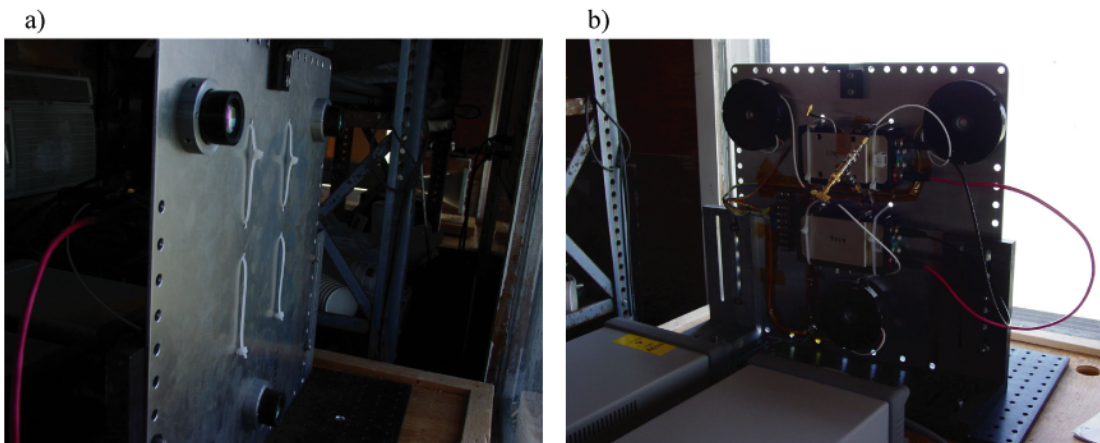


Figure 3.1: Modulated retro-reflector array installed on Tilghman Island
a) Frontside, b) Backside

3.1 Cat's-eye modulated retro-reflector

The cat's-eye retro-reflector consisted of a 16 mm diameter lens with a mirror in the focal plane covered by a quantum-well modulator. The cat's-eye retro-reflector is depicted in Illustration 3.1. The incident beam refracts through the collection lens. The light focuses onto a spherical mirror in the focal plane and reflects back out of the collection lens. The beam reflected back out of the collection lens has a departure angle equal to the angle of arrival of the incoming beam. In this way, the device is a retro-reflector. The data is modulated onto the incident light by the quantum-well modulator.

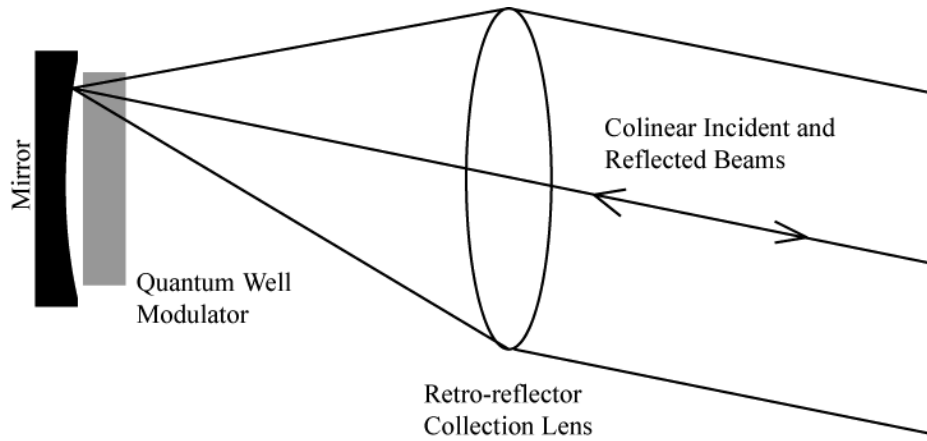


Illustration 3.1. Cat's-eye modulated retro-reflector

A quantum-well modulator was placed over the mirror to imprint the data modulation on the incident CW interrogator beam. The modulation drive current through the modulator shifts the absorption peak modulating the beam. The

modulator is driven with a simple MOSFET current driver. The size of the modulator defines the field of view (FOV) of the retro-reflector by equation (3.1). The edge length of the modulator is denoted as l . The focal length of the collection lens is F .

$$FOV = \frac{l}{F} \quad (3.1)$$

The size of the modulator also determines the data rate. A larger modulator provides a larger field of view but at the cost of modulation speed. So the MRR design has an intrinsic trade-off between the data rate and the field of view. Further, the aperture size is also restricted by the FOV since the F-number of the collection optic must be fixed at $f/2$ to minimize wavefront loss. The MRR array had a 20 degree field of view and a bit rate of 2 Mbps.

3.2 Communication system

The modulated retro-reflector array communication system is depicted in Illustration 3.2 by the system block diagram of the MRR array. The main components are the data compressor, the data sources, the modulator driver, the modulators, and a photodetector. The outgoing data was read into the data compressor, which compressed the video and encoded the data. The data was Manchester encoded at a rate of 2 Mbps. The encoded data was sent to the modulator driver. The modulator driver provided the current drive for the modulators. The modulators imprinted the CW interrogation beam with the data. The retro-reflected interrogation beam carried the data back to the interrogator. The photodetector on the MRR array enabled data

from the interrogator to be received by the MRR communication system. The received signal was feed into the data compressor unit for decompression. The bidirectional link enabled a half-duplex 2 Mbps Ethernet link between the two ends of the FSO link. The data stream was bridged to the laptop by the data compressor via a full-duplex 100 Mbps connection.

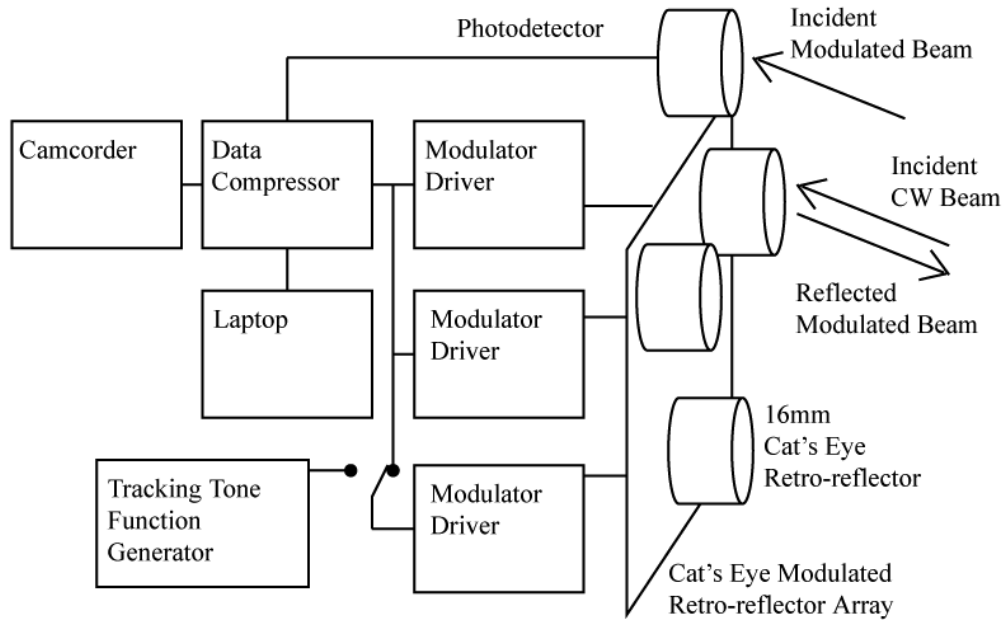


Illustration 3.2. Modulated retro-reflector array block diagram

The modulator drivers could be disconnected from the data compressor and instead connected to a function generator. This interchange could be done to facilitate the use of one or more of the MRRs for generating the tracking tone. The default configuration intended to use one MRR for generating the tone and two for modulating the data. It was found experimentally that the 20 kHz square wave generated by the digital modulator driver for the tracking tone disrupted the

communications channel in the PINFET receiver. For this reason, the tracking tone was modulated onto the interrogation beam by the interrogator for the majority of the link testing. This allowed all three modulators to be used for data modulation. This approach allows the potential for false acquisitions of glint reflections of the interrogation beam. No false acquisitions were observed during the operation of the link with a locally (interrogator side) generated tracking tone.

Chapter 4 Interrogator system description

The interrogator terminal was developed by the author at the Laboratory for the Physical Sciences. The interrogator terminal was a bi-static optical system with active pointing and tracking enabled by two fast steering mirrors. The interrogator is pictured in Figure 4.1 on an optical table at the CBD link installation. The interrogator outputs an 8 inch CW beam with 6 W of power at a wavelength of 1550 nm. This output beam was designed to be Class 1M eye safe. The interrogator receiver had an 8 inch aperture. The interrogator was equipped with two alignment cameras to aide link acquisition.

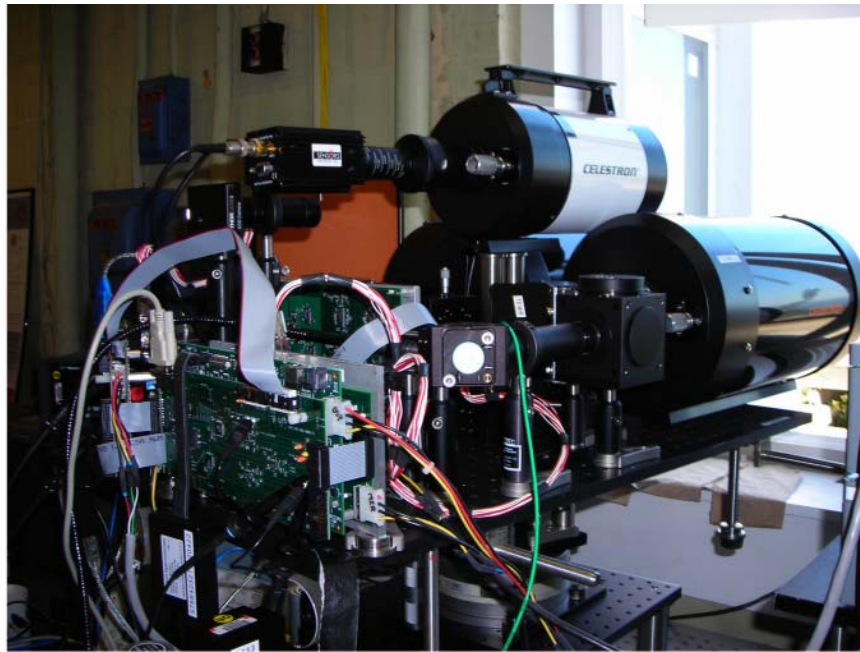


Figure 4.1: Interrogator terminal installed at Chesapeake Bay Deployment laser link test range

The interrogator system block diagram is shown in Illustration 4.1. The interrogator consisted of the transmitter optical train, the receiver optical train, the alignment cameras, the pointing and tracking system, and the communications system. The transmitter optical train was responsible for projecting the interrogation beam down range to the MRR array. The receiver optical train was responsible for collecting the return from the MRR array. The alignment cameras were equipped to aid initial link alignment. The pointing and tracking system maintained link alignment through dynamic link disturbances. The communications system detected and decoded the data from the return signal.

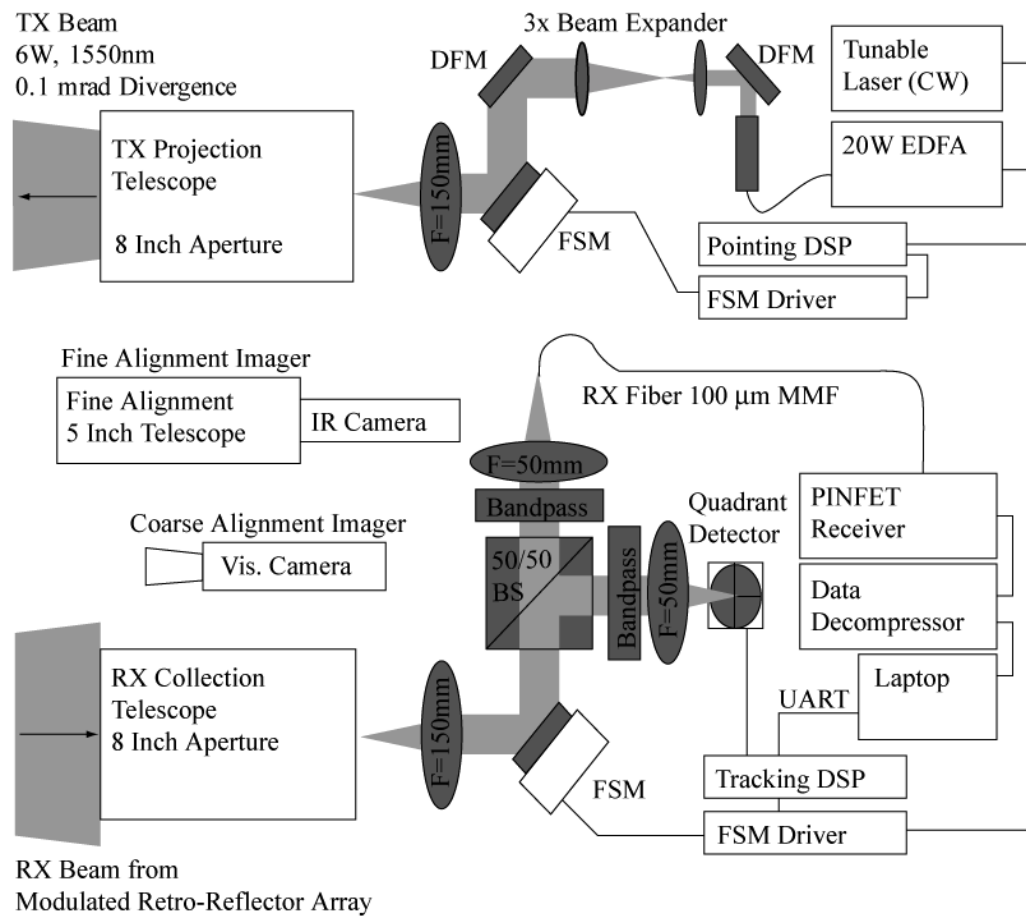


Illustration 4.1: Interrogator system diagram

4.1 Transmitter optical train

The transmitter consisted of a Photonetics tunable laser driving a 20 Watt IPG Photonics EDFA. The output of the EDFA had a hermetically sealed collimating lens that output a 5mm beam. The output of the EDFA reflected off a fold mirror used for alignment. The transmitter beam then was passed through a 3x beam expander and reflected off a second alignment mirror. Then, the transmitted beam reflected off the pointing fast steering mirror used to control the pointing of the outgoing beam. The beam was expanded to the final output beam diameter by the combination of the decollimating lens and the 8 inch projection telescope. The telescope had an adjustable primary-secondary separation that sets the focus of the telescope. The telescope focus was used to set the beam divergence of the outgoing beam to 100 μ rad.

4.2 Receiver optical train

The receiver optical train began with an 8 inch telescope serving as the collection aperture. The received light was collimated by the collimating lens. The light then reflected off the tracking fast steering mirror. The tracking fast steering mirror was employed to keep the received light focused on the photoreceiver optical fiber. The light reflected off the fast steering mirror was split into two equal beams by a 50/50 beam splitter. Both beams pass through 30 nm wide optical bandpass filters to remove any out-of-band background light. One beam was focused onto the quadrant detector to provide the tracking error signal. The other beam was focused on the photoreceiver fiber.

4.2.1 Solar background

The optical bandpass filter was chosen to reduce the solar background, while still providing enough optical passband to pass the received signal.[76] The transmitted laser was a tunable laser in the C band centered at 1550 nm. Wavelength tuning was required to accommodate the temperature dependence of the modulating retro-reflectors. The absorption peak of the modulator shifts with temperature. The interrogator beam must be tunable to the wavelength that maximizes the contrast ratio of the modulator. The modulator had a nominal operating wavelength of 1550 nm. The temperature dependence of the modulator may shift the operating wavelength by 10 nm. Commercial bandpass filters are available in 10 nm and 30 nm passbands. Due to the temperature variation of the operating wavelength, a 30 nm bandpass filter was chosen for the receiver optical bandpass.

A radiometric calculation was done to determine if a 30 nm filter provided sufficient reduction in solar background. The solar background on the receiver is given by equation (4.1). I is the solar irradiance at 1550 nm. F is the detector field of view. L is the albedo (diffuse reflectivity) of the downrange scene as seen by the detector. R is the link range. D is the receiver aperture diameter. The RX optics loss is η . The filter bandwidth is BW .

$$P_B = I \cdot L \cdot \frac{\pi}{2} \cdot \left(\frac{F}{2}\right)^2 \cdot \left(\frac{D}{2}\right)^2 \cdot \eta \cdot BW \quad (4.1)$$

Applying equation (4.1) with the interrogator system parameters and assuming an albedo of 0.2 and a solar irradiance of $0.25 \text{ Wm}^{-2}\text{nm}^{-1}$, the solar background on the quadcell should be approximately 20 nW (-47 dBm). This is sufficiently low for no degradation in the tracking sensitivity.[77][78] The effect of background light on the quadcell will be shown in detail in Section 4.5.

The narrow FOV of the communication detector makes the background light insignificant to the communication detector sensitivity. The background light on the communications detector should be below 100 fW (-70 dBm). This is significantly below the sensitivity of the detector (-57 dBm) and even further below the expected return from the MRR array (-44 dBm).

4.2.2 Acquisition cameras

The interrogator was equipped with two acquisition cameras to aid in the initial alignment of the optical link. These two cameras consisted of a wide field of view (FOV) visible camera and a narrow FOV IR camera. The visible camera was capable of imaging the opposite end of the link. The narrow field of view IR camera enabled the light returned from the retro-reflecting array to be imaged. The wide FOV camera was used to get the link roughly aligned. The narrow field of view camera was then used to finely tune the alignment of the link.

The wide FOV visible camera was a Thorlabs DC310C Firewire camera. The imaging lens used with this camera was a 1 inch, 100 mm focal length, achromatic lens. This camera had a field of view of 3 degrees (53 mrad) and a resolution of approximately 75 μrad . The Thorlabs' *Thorsight* camera software provided crosshairs

that were aligned to the interrogator transmitted beam. These crosshairs could then be used for initial link pointing.

The original interrogator design employed a visible narrow FOV alignment camera instead of the IR camera. The alignment of this camera was disturbed during transport to the CBD link deployment. Fortunately, the resolution of the wide FOV camera was sufficient to complete the initial alignment of the link without the use of the narrow field of view camera. Once the link was aligned, the visible narrow FOV camera was replaced with a narrow FOV IR camera to image the return from the retro-reflector array. The image of the IR return enabled definitive identification of the various retro-reflecting targets on the Tilghman Island tower. The narrow field of view IR camera was a Sensors Unlimited SU320-1.7RT camera. This camera was placed in the image plane of a 5 inch Cassagrain telescope. This camera had a 3 mrad FOV and a resolution limited by the telescope of 35 μ rad.

4.3 Pointing and tracking system

Pointing and tracking for the interrogator terminal was achieved through two fast steering mirrors and a quadcell detector. The quadcell detector was used to detect the angle of arrival error of the return light. This detection was enhanced by the addition of a 20 kHz tracking tone on the interrogator beam to differentiate the return from background light. The tracking error signal was processed with a controller implemented in a C6416 DSP to control the tracking fast steering mirror. The pointing fast steering mirror was controlled based on feedback from position sensors internal to the FSM as well as feed-forward data from the tracking FSM mirror

position. The feed-forward of the tracking mirror position enabled the terminal to point the transmitted beam as well as track the received return beam. The pointing and tracking system will be discussed in detail in Chapters 5 and 6.

4.4 Communication system

The received optical signal returned from the MRR array was coupled into a 100 μm optical fiber. The 100 μm optical fiber guided the return from the MRR array to a photoreceiver. The photoreceiver circuit was developed by NRL and used an PINFET photodetector manufactured by Laser Diode Incorporated. The output of the photoreceiver was input to a data decompression circuit. The data was sent to a laptop computer via an Ethernet connection. The data is stored and presented on a laptop computer.

The communication system also supported bidirectional half-duplex data transfers. For bidirectional data transfers, outgoing data was modulated onto the interrogating beam. The downlink data (data going to the MRR) was received at the MRR array by an optional photodetector. The received downlink signal was conveyed to a laptop computer. The half-duplex link enabled an Ethernet link between both ends of the link. File transfers were then possible across this Ethernet link. When atmospheric fading was high, packet retransmission was employed to ensure complete file transfer.

4.5 Bi-static versus mono-static optical design

One of the pivotal design choices for the interrogator was between a mono-static optical system and a bi-static optical system. A mono-static system has a more simple control system at the expense of a more complicated optical system. In addition, the mono-static system has the advantage that the transmitted beam traverses the same atmospheric path as the received beam. The bi-static system has a simpler optical design, but the pointing and tracking system is twice as complicated.

Initially, a mono-static design was chosen for the interrogator. This design employed polarization to separate the transmitted beam from the received beam. The mono-static beam combination optics are depicted in Illustration 4.2. In this design the transmitted beam had a horizontal polarization achieved with a Glan-Thompson polarizer. A $\frac{1}{4}$ -wave plate was to be used to convert the horizontal polarization to right-handed circular polarization for projection to the MRR array. After reflection from the retro-reflector, the right-handed transmitted beam would become a left-handed return beam. The $\frac{1}{4}$ -wave plate converts the left-handed circular polarized return to vertical polarization. A polarization selective beamsplitter was used to separate the transmitted and received beams. Polarizers were used to increase the isolation between the transmit and received beams beyond the 1:1000 achievable with the beam-splitter alone.

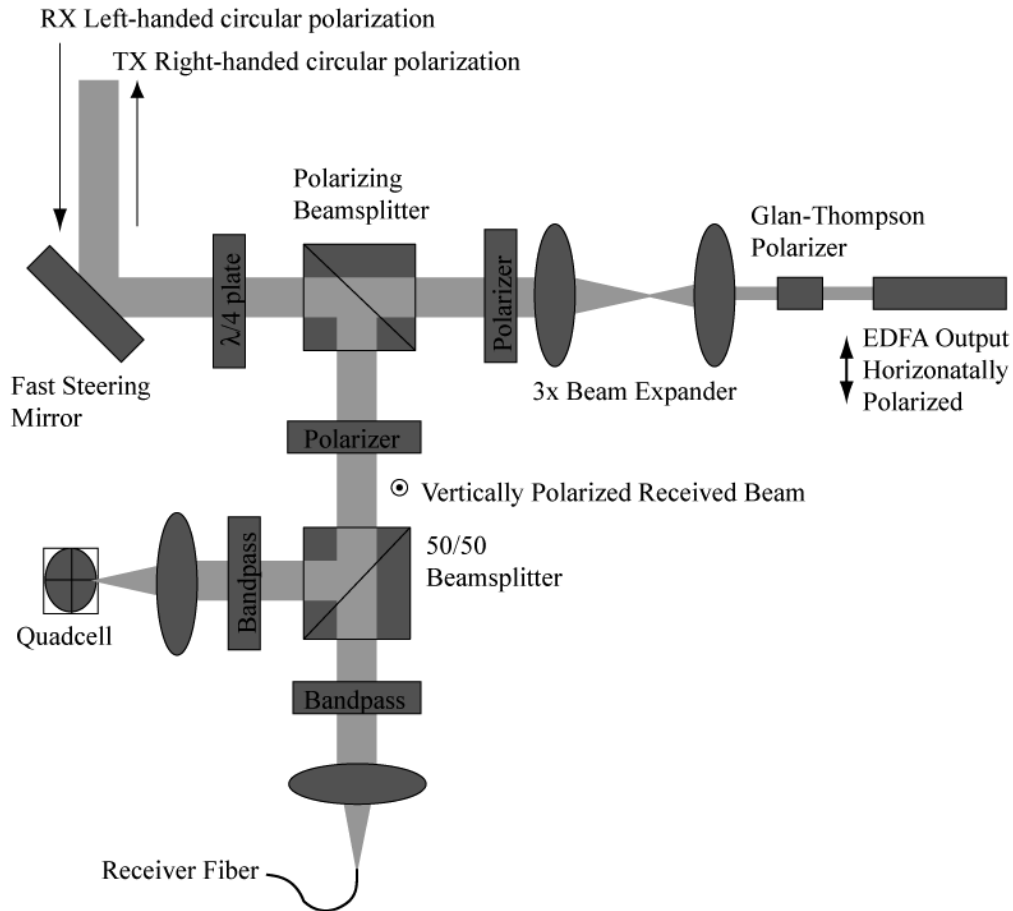


Illustration 4.2: Mono-static interrogator back-end optical system

The combination optics for the mono-static design was implemented in the lab and a stray light test was performed. The goal of this test was to determine how much light from the transmitter would reach the receiver. For the purposes of this test, the detector that was used was configured to simulate the field of view of the quadcell. Since the quadcell was more sensitive and had a larger field of view than the communications detector, the quadcell was more sensitive to stray light. The stray light was measured with and without the $\frac{1}{4}$ -wave plate. It was proposed that the $\frac{1}{4}$ -

wave plate would contribute the majority of the stray light. The measured stray light is presented in Table 4.1.

Stray light configuration	Measured stray light
With $\frac{1}{4}$ -wave plate	-9.2 dBm
Without $\frac{1}{4}$ -wave plate	-12.2 dBm

Table 4.1: Mono-static design stray light measurements

A separate test was done on the quadcell to determine the power penalty to the sensitivity incurred from excess stray light. Listed in Table 4.2 is the quadcell sensitivity in the presence of increasingly high levels of background DC light. The reduction in sensitivity in Table 4.2 was validated as excess shot noise with the quadcell circuit model presented in Section 5.2.

DC Background [dBm]	Quadcell Sensitivity [dBm]
-60	-67
-50	-67
-40	-67
-30	-63
-20	-55
-10	-45

Table 4.2: Quadcell sensitivity versus background illumination

From Tables 4.1 and 4.2, it can be seen that the excess stray light of -10 dBm would cause a dramatic reduction (>20 dB) in quadcell sensitivity. The stray light could be mitigated by a dramatic reduction in quadcell field of view. However, this

was an undesirable system trade-off as it would make link acquisition more difficult and adversely limit the range of the tracking sensor.

Even the most minute scattering reflection will couple an unacceptable amount of light back into the receiver. This was particularly evident in the beam dump employed in the stray light test. A beam dump was used to eliminate the transmit beam once it left the combination optics. The stray light test was intended to determine only the effects of stray reflections inherent in the combination optics. Any back reflections from the transmitter beam once it exited the combination optics was to be avoided by the use of the beam dump. Commercial beam-dumps reflected too much light back towards the combination optics to get a good isolation baseline measurement. These commercial beam dumps included the Thorlabs Model 500 “Blackhole” and the Thorlabs LB1 razor blade stack beam block. A custom beam dump comprising 6 ND filters (ND values of 3, 3, 2, 2, 1, and 0.5) tilted off-axis was used to absorb and reflect off-axis the transmitted beam as much as possible. The beam dump enabled a stray light measurement for the combination optics alone. The stray light measurement provided a best case operating scenario since the front-end beam expansion optics would surely add additional stray light to what was measured in the combination optics alone. A failure of the combination optics was a definite indicator that the completed system would have unacceptable stray light performance.

Due to the excessive stray light in the mono-static design, the optical design was changed to a bi-static design. The spatial separation of the transmitted and received beams ensured the isolation of the two beam paths. This benefit came at the cost of doubling the complexity of the pointing and tracking system. Although the

mono-static design failed, the benefits of a mono-static design make it a desirable goal. If sufficient optical isolation could be achieved, a mono-static solution would be preferable. However, a polarization based mono-static optical system will be extremely difficult to design if it is even at all possible.

Chapter 5 Tracking system design

The pointing and tracking system consisted of two coupled control loops. One control loop controlled the pointing fast steering mirror to properly point the transmitted beam. A second control loop controlled the tracking fast steering mirror to track the received beam. The tracking control loop used the received light focused onto the quadrant detector to detect changes in the beam angle of arrival. The tracking control loop compensated the angle of arrival error with the fast steering mirror. The position of the tracking fast steering mirror was fed forward to the pointing control loop. The pointing control loop commanded the pointing fast steering mirror to move in synchronization with the tracking fast steering mirror. This enabled the pointing and tracking mirrors to act in unison to correct vibration and common-mode atmospheric tip-tilt error.

The block diagram for the pointing and tracking system is depicted in Illustration 5.1. Shown in this diagram are the two fast steering mirror control loops and the connection between them. Described in the remainder of this chapter is the hardware design of the pointing and tracking system. The main components of the pointing and tracking system are the quadcell, the data-converters (ADC and DAC), the DSP, the fast steering mirror, and the fast steering mirror driver.

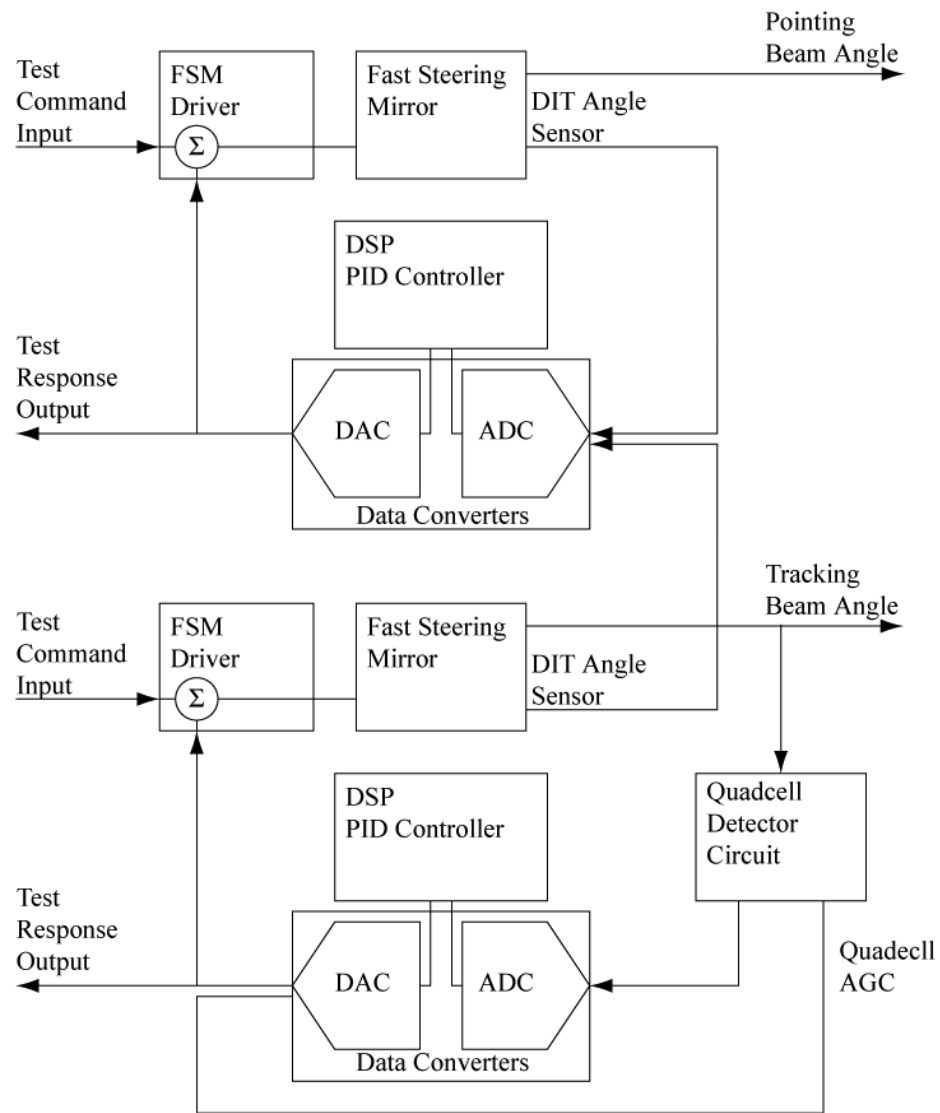


Illustration 5.1: Pointing and tracking control system block diagram

5.1 Tone tracking

The optical link was differentiated from solar background by a small 20 kHz amplitude modulation of the beam.[7][12] This enabled a significant improvement in quadcell sensitivity over direct (DC level) detection. Using tone tracking, the sensitivity of the quadcell was 10 dB better than the sensitivity of the communications detector. This enabled the interrogator to maintain link alignment even when the optical return was below the sensitivity of the communications detector.

The tracking tone can be generated in one of three ways. First, the tone can be placed onto the interrogator outgoing beam (local generation). Second, the tone can be generated by a subset of the modulated retro-reflectors in the retro-reflector array. Third, the tone can be generated by adding a small ripple modulation to the data modulation on all the modulated retro-reflectors in the array.

Modulating the outgoing interrogator beam is the simplest tone implementation. The modulation depth of the tone is kept below 15% to minimize its effect on the communications channel. This approach has the advantage of a simplified modulated retro-reflector design. Another advantage is that the interrogator can increase the modulation depth of the tone during acquisition, then reduce the modulation depth once communications begin. The major disadvantage of this approach is that glint reflections from objects which are not the MRR may cause false acquisitions. The extreme length of the 16 km link makes it very unlikely that any unwanted reflections would return to the interrogator with sufficient energy to trigger a false acquisition.

For the 16 km FSO link the tone was generated in two ways. First, the tone was generated locally by the interrogator. Second, the tone was generated by the MRR array. When the tone was generated by the MRR array, it was done with the MRR digital driver. This produced a 20 kHz square wave modulation. This square wave modulation interfered with the reception of the communications channel. For this reason, local tone generation was employed for the majority of the link testing. No false acquisitions were observed despite the increased vulnerability to this failure mode.

5.2 Quadrant detector

The angle of arrival sensor for the tracking system was a tone tracking quadrant detector. The block diagram for the quadcell amplifier chain is provided in Illustration 5.2. This amplifier chain was replicated for each of the four quadrant signals. The quadcell circuit was fabricated on a 6 layer PCB shown in Figure 5.1. The quadrant detector was a 3mm InGaAs quadrant detector. The InGaAs detector provided greater sensitivity over a Germanium quadrant detector used earlier in the development of the quadrant detector circuit. The quadcell was operated in photovoltaic mode to minimize dark current noise and to provide a consistent transfer function.[79]

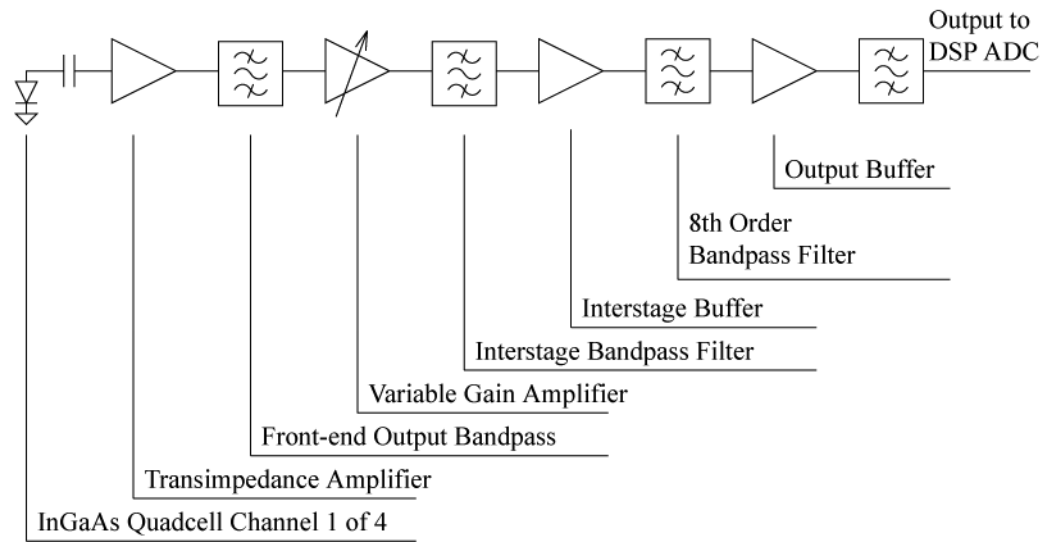
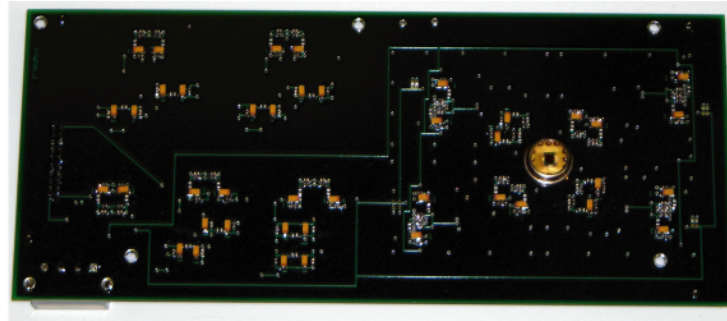


Illustration 5.2: Quadcell amplifier chain block diagram

a) Quadcell board frontside



b) Quadcell board backside

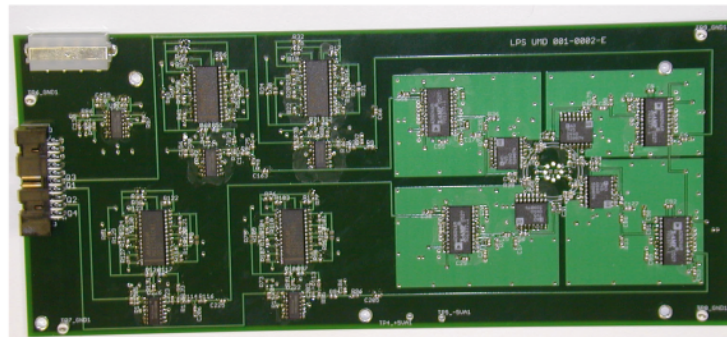


Figure 5.1: Quadcell board

a) Frontside with quadcell, b) Backside with amplifier chain

The quadcell was AC coupled to the transimpedance amplifier to pass the 20 kHz tracking tone while rejecting the DC background. This AC coupling increased the dynamic range of the front-end amplifier. The transimpedance amplifier provides the first stage of signal amplification and filtering. The second stage amplifier was a variable gain amplifier (VGA) used to provide automatic gain control (AGC) for the quadcell circuit. The control voltage for the VGA was provided by the DSP and determined from the strength of the 20 kHz tone. The final stage of the quadcell circuit was an 8th order active bandpass filter. This bandpass filter provided the majority of the signal filtering by limiting the quadcell signal to a band between 15 kHz and 25 kHz. The input and output of this filter were buffered with inverting op-amp stages to provide the necessary level shifting and to add additional filtering.

A quadcell detector noise analysis was completed to determine a circuit design that would provide the phase-locked loop the required 0.5 SNR for locking onto the tracking tone at an input optical power of -67 dBm.[80] The transimpedance amplifier circuit design was critical to the sensitivity of the quadcell. The maximization of the sensitivity was accomplished using the circuit model given in Figure 5.2. There were four main noise sources considered in this model. The quadcell noise sources were shot noise, thermal noise, voltage noise, and current noise. The detector dark current was included in the shot noise current term for the purposes of this model. The voltage and current noise sources were due to the input voltage noise and the input current noise of the AD745 operational amplifier used for the transimpedance amplifier. Flicker noise, or 1/f noise, was neglected in this model as the 20 kHz center frequency was well above any significant 1/f noise contribution.

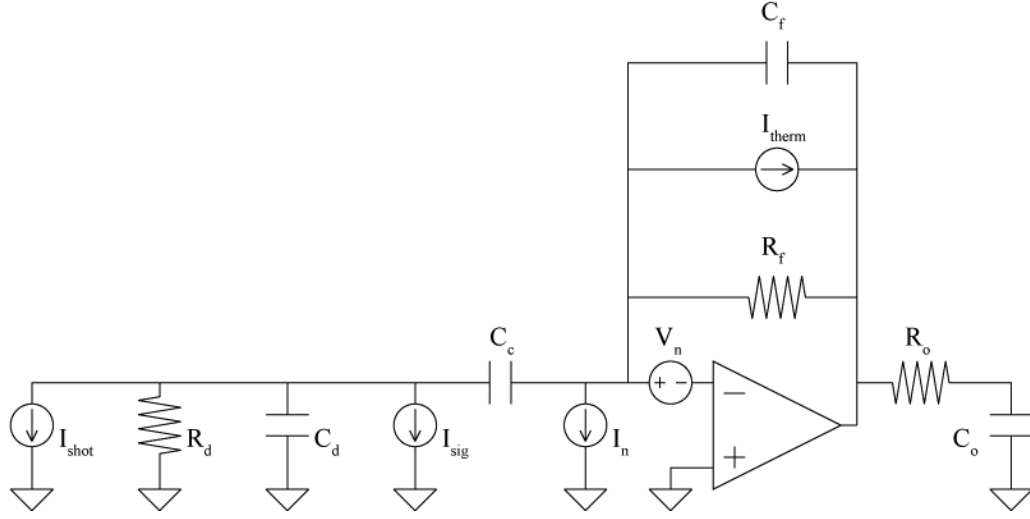


Figure 5.2: Quadcell transimpedance amplifier noise model

The ultimate metric of the quadcell noise performance was the SNR ratio presented to the phase-locked loop. The SNR for the tracking signal is given in equation (5.1). The signal power, P_{Sig} , is the power of the tracking tone. The noise contributions are the shot noise, σ_s^2 , the thermal noise, σ_T^2 , the voltage noise, σ_V^2 , and the current noise, σ_C^2 .

$$SNR = \frac{P_{Sig}}{\sigma_s^2 + \sigma_T^2 + \sigma_V^2 + \sigma_C^2} \quad (5.1)$$

To properly evaluate the SNR it was necessary to determine how the signal and noise sources are filtered by the quadcell circuit. Circuit analysis was performed to determine the transfer functions between the sources and the input to the phase-locked loop. The first step in determining the overall transfer functions was to first determine the transfer functions through the transimpedance amplifier stage shown in

Figure 5.2. The transfer functions for the shot noise, $H_s(s)$, the thermal noise, $H_T(s)$, the voltage noise, $H_v(s)$, and the current noise, $H_c(s)$, are given in equations (5.2) through (5.5). The transfer coefficient of the tracking tone, H_{Sig} , is provided in equation (5.6).

$$H_s(s) = \frac{R_f}{(1 + s C_f R_f)} \frac{s C_c R_d}{(1 + s R_d (C_c + C_d))} \frac{s R_o C_o}{(1 + s R_o C_o)} \quad (5.2)$$

$$H_T(s) = \frac{R_f}{(1 + s C_f R_f)} \frac{s R_o C_o}{(1 + s R_o C_o)} \quad (5.3)$$

$$H_v(s) = 1 + \frac{R_f}{(1 + s C_f R_f)} \frac{1}{\frac{R_d}{1 + s C_d R_d} + \frac{1}{s C_c}} \frac{s R_o C_o}{(1 + s R_o C_o)} \quad (5.4)$$

$$H_c(s) = \frac{R_f}{(1 + s C_f R_f)} \frac{s R_o C_o}{(1 + s R_o C_o)} \quad (5.5)$$

$$H_{Sig} = \frac{R_f}{(1 + \omega_o C_f R_f)} \frac{\omega_o C_c R_d}{(1 + \omega_o R_d (C_c + C_d))} \frac{\omega_o R_o C_o}{(1 + \omega_o R_o C_o)} \quad (5.6)$$

The magnitude of the noise factors input to the PLL can be found by multiplying the transimpedance transfer functions by remaining circuit transfer functions common to all signals. The remaining circuit transfer functions are the gain of the VGA, $G_{VGA} = 10000$, the transfer function of the 8th order bandpass filter, $H_A(s)$,

and the transfer function of the phase-locked loop, $H_{PLL}(s)$. The transfer function of the 8th order bandpass filter, $H_A(s)$, is given in equation (5.7). The transfer function of the PLL is given by equation (5.8). The 8th order bandpass filter passband was between, $F_L = 15$ kHz and $F_H = 25$ kHz. The passband of the PLL was between $F_l = 19990$ Hz and $F_h = 20010$ Hz. The final noise contributions were evaluated by integrating the noise source power spectral densities over the filtering functions of the entire quadcell circuit. The noise filtering is expressed in equations (5.9) through (5.12). The strength of the tracking tone signal is simply expressed in equation (5.13) as the 20 kHz was centered in the passband of most of the filtering. Here the incident optical power is P_{opt} . R is the detector responsivity.

$$H_A(s) = \frac{2\pi F_L s}{(s + 2\pi F_L)(s + 2\pi F_H)} \quad (5.7)$$

$$H_{PLL}(s) = \frac{2\pi F_l s}{(s + 2\pi F_l)(s + 2\pi F_h)} \quad (5.8)$$

$$\sigma_s^2 = \int_{-\infty}^{\infty} I_{Shot} H_s^2(s) H_A^2(s) H_{PLL}^2(s) G_{VGA}^2 ds \quad (5.9)$$

$$\sigma_T^2 = \int_{-\infty}^{\infty} I_{Therm} H_T^2(s) H_A^2(s) H_{PLL}^2(s) G_{VGA}^2 ds \quad (5.10)$$

$$\sigma_V^2 = \int_{-\infty}^{\infty} V_n H_V^2(s) H_A^2(s) H_{PLL}^2(s) G_{VGA}^2 ds \quad (5.11)$$

$$\sigma_C^2 = \int_{-\infty}^{\infty} I_n H_C^2(s) H_A^2(s) H_{PLL}^2(s) G_{VGA}^2 ds \quad (5.12)$$

$$P_{Sig} = (P_{Opt} R H_{Sig})^2 \quad (5.13)$$

The Matlab script in Appendix B was written to use the previous analysis to calculate the SNR of the quadcell as a function of the parameters of the transimpedance amplifier circuit. The Matlab script was used to vary the transimpedance parameters to maximize the quadcell sensitivity. The results of the SNR calculation are presented in Table 5.1. The AD745 was used for the transimpedance amplifier for its unique combination of low voltage and low current noise. Op-amps like the OPA847 can provide lower voltage noise but the accompanied increase in current noise cancels any benefit of the reduced voltage noise. The AD745 provided the best minimization of all noise sources in the amplifier. It can also be seen that the quadcell circuit design approaches the ultimate goal in detector design of balancing the various noise contributions.

Shot Noise [V]	0.049
Thermal Noise [V]	0.058
Current Noise [V]	0.003
Voltage Noise [V]	0.075
Signal Level [V]	0.064

Table 5.1: Quadcell noise contributions and expected signal level for comparison

Finally, it should be noted that the design of a high sensitivity, low frequency detector is much different than the design of high speed detectors. High speed detectors are dominated by thermal noise and as such the sensitivity scales with bandwidth. This is not the case for lower frequencies where shot noise from background light and electronic noise can dominate.

5.3 Data converter subsystem

The data converter subsystem consisted of the analog-to-digital converter (ADC) and the digital-to-analog converter (DAC) used for interfacing the DSP to the tracking system signals. The data converter board was designed to be a daughter card to the C6414 DSP evaluation board from Spectrum Digital. The block diagram for the data converter system is given in Illustration 5.3.

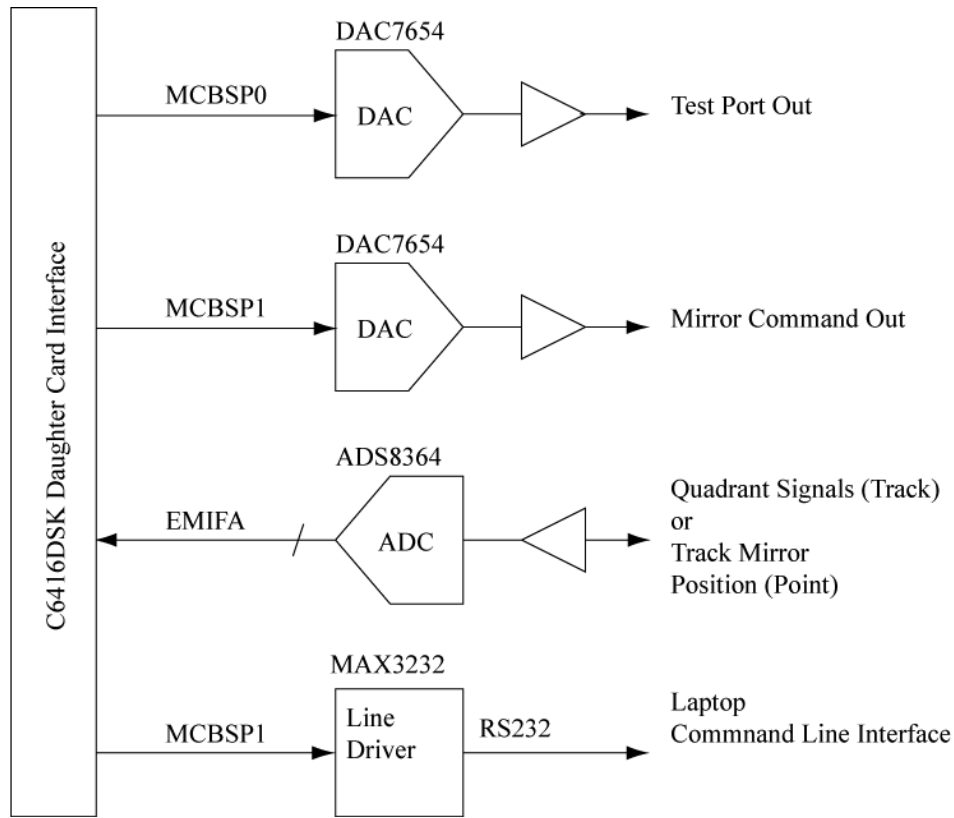


Illustration 5.3: Data converter block diagram

The ADC was connected to the DSP through a 16 bit external memory interface (EMIF). An op-amp pair was used to perform level shifting prior to the ADC input. The ADC converter sampled the quadcell signals at 200 kHz. This was the sampling frequency of the tracking tone phase-locked loop.

There were two DAC units on the data converter. One DAC was used to control the quadcell AGC and the fast steering mirror. The second DAC was used to provide diagnostic signals. The DACs had output inverting amplifiers to buffer the DAC outputs and to provide 1st order filtering of the quantization noise. The DAC was interfaced to the DSP through a multi-channel bidirectional serial port (McBSP).

The DACs were output at 10 kHz. This 10 kHz sampling rate was the sampling rate for the tracking loop as well as the quadcell AGC loop.

A cross connect port was included on the data converter to allow the passing of the tracking fast steering mirror angle signals from the tracking system to the pointing system. The cross connect signals were configured through solder jumpers to enable the same data converter board to be used for the pointing controller as well as the tracking controller. The data-converter board is shown in Figure 5.3.

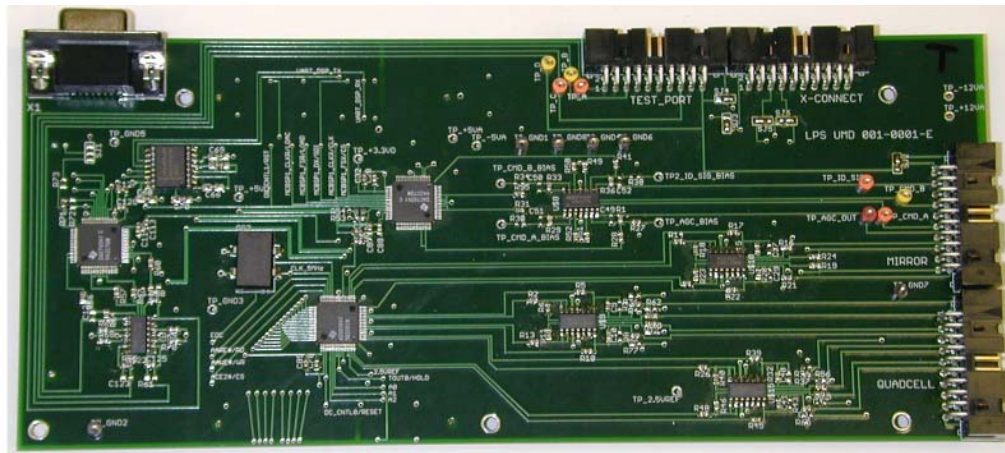


Figure 5.3: Data converter board

5.4 Digital signal processor

The digital signal processor (DSP) used for the tracking controller was the C6416 fixed point DSP from Texas Instruments. The DSP hardware used in the tracking system was the C6416 DSK development board from Spectrum Digital. The C6416 DSK provided a simple daughter card interface to the DSP peripherals. These peripherals were used to interface the data converters implemented on the data

converter board. The embedded software was developed in C using Texas Instruments' Code Composer Studio development environment. This provided a chip support C library for register configuration as well as a JTAG based debug interface for loading code and controlling program execution on the C6416. The DSP runs at a 1 Ghz clock rate.

5.5 Fast steering mirror

The fast steering mirror used in the pointing and tracking systems was the Newport FSM-320. The fast steering mirror is a voice coil driven, flexure mounted, two inch mirror. The range of this mirror is three degrees. The fast steering mirror driver provided by Newport was not used for controlling the FSM. A custom mirror driver was designed to provide greater flexibility in the tracking system design. This enabled improved control of the fast steering mirror as well as a significant reduction in the size of the FSM driver.

The fast steering mirror driver consisted of a simple transconductance op-amp circuit. The block diagram for the mirror driver circuit is shown in Illustration 5.4. This circuit was implemented on a 5 layer PCB shown in Figure 5.4. A high current op-amp from APEX (PA10) was used to drive the voice coils in the fast steering mirror. A small current sense resistor was used to measure the coil current. The coil current signal was fed back through a loop filter with gain to the summing input of the power amplifier. The gain of the feedback was used to set the transconductance of the driver. The transconductance of the driver was set to provide a 10 μ rad static mirror deflection for a single command DAC step. The loop filter was used to limit

the bandwidth of the driver to 10 kHz. The loop filter was employed to reduce any noise from frequencies out of the range of signals produced by the DSP mirror controller.

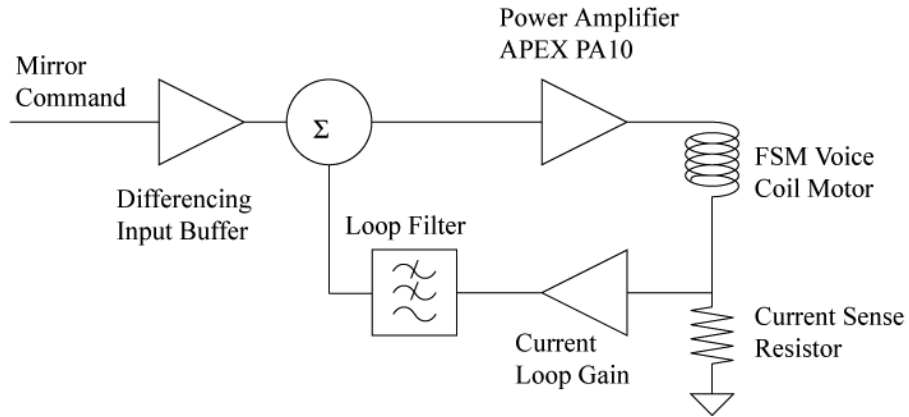


Illustration 5.4: Fast steering mirror driver block diagram

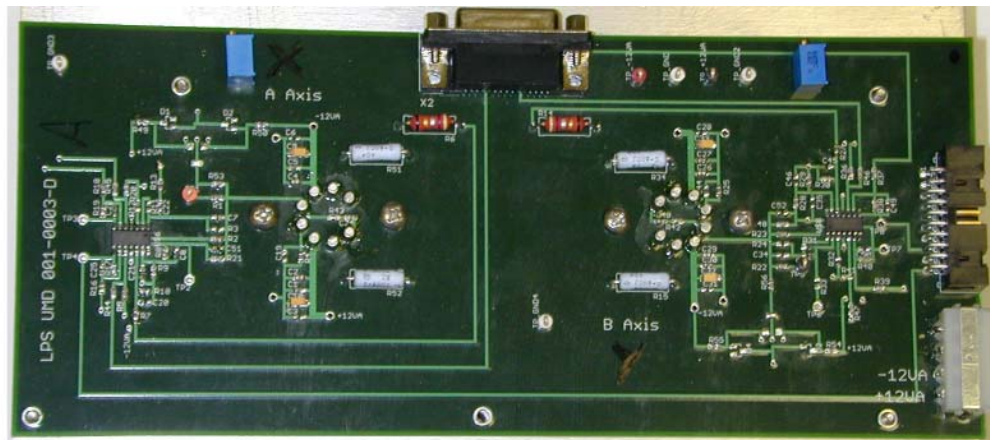


Figure 5.4: Fast steering mirror driver board

Chapter 6 Tracking system software design

The embedded controller software consisted of three main algorithms. The first was the tone tracking phase-locked loop (PLL). The second was the quadcell AGC. The third was the controller for the pointing and tracking fast steering mirrors. In addition to these three main algorithms, the embedded software included a serial port command line interface and outputs to LED status indicators.

6.1 Tone tracking phase locked loop

The phase-locked loop was used for detecting the 20 kHz tracking tone. The local oscillator output of the PLL was used to demodulate the tracking tone signal from the 4 quadrant channels.[81] The demodulated quadrant signals were then be used to determine the angle of arrival error signal via the quadcell math equations given in equations (1.2) and (1.3). The mean value of the PLL phase error was used to determine when the PLL had locked onto the tracking tone. When PLL was locked, a green LED was illuminated. The green LED indicator was the first proof of a completed 16 km MRR link.

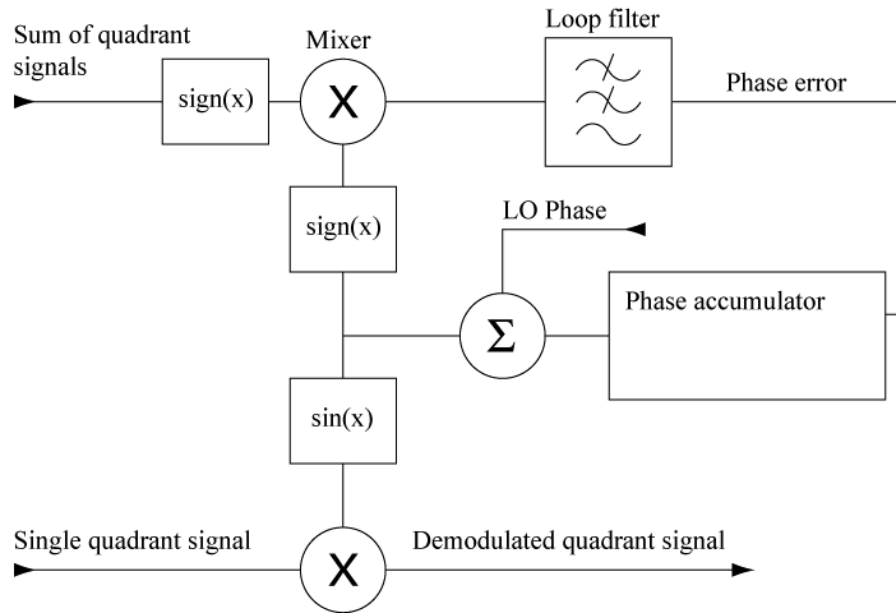


Figure 6.1: Phase locked loop block diagram

The block diagram for the phase-locked loop is depicted in Illustration 6.1. The phase-locked loop implementation was a first order digital phase-locked loop.[80] By using a digital phase-locked loop, only the zero crossings of the quadcell signal contribute to the phase error. This approach prevented any noise due to signal fading from coupling into the phase error.

The input quadrant detector signals were summed and then sign limited. The sign of the input quadcell signal was multiplied by the sign of the phase estimate. The resulting signal was low-pass filtered to eliminate the high frequency products and to isolate the first order product that is proportional to the phase error. The phase error was integrated by an accumulator and summed with the phase of the free-running local oscillator. The result was the phase estimate for the next loop iteration. Once the loop locks onto the input frequency, the phase estimate was used as the argument of sine function look-up table. This sine function was mixed with the four

individual quadrant signals to demodulate the 20 kHz tone. The resulting demodulated quadrant signals were low-pass filtered to remove higher order products. The first order product was proportional to the incident optical power and was used in the quadcell error signal calculation.

The phase locked-loop was implemented in fixed point math for optimized execution speed on the fixed point C6416 DSP. This implementation consisted of factoring floating point filter coefficients into a base two exponent and an integer mantissa. Multiplication is implemented by a right shift of the base two exponent followed by an integer multiplication of the mantissa. The phase-locked loop execution occurred on a timer interrupt at a 200 kHz sampling rate.

The performance of the fixed point math PLL was modeled in a Matlab script listed in Appendix C. This model was used to determine the lock-in time and noise performance of the PLL for various bandwidth settings. The PLL model was executed for 4 PLL bandwidths; 5 Hz, 16 Hz, 48 Hz, and 243 Hz. Plotted in Figure 6.2 is the frequency error of the PLL versus time as the loop locks onto the 20 kHz input tone. The 20 kHz input tone is -50 Hz from the PLL free-running local oscillator frequency of 20050 Hz. When the frequency error settles to -50 Hz, the PLL has locked onto the 20 kHz input tone. It can be seen in Figure 6.2 that an increase in the PLL bandwidth decreases the lock-in time of the PLL.

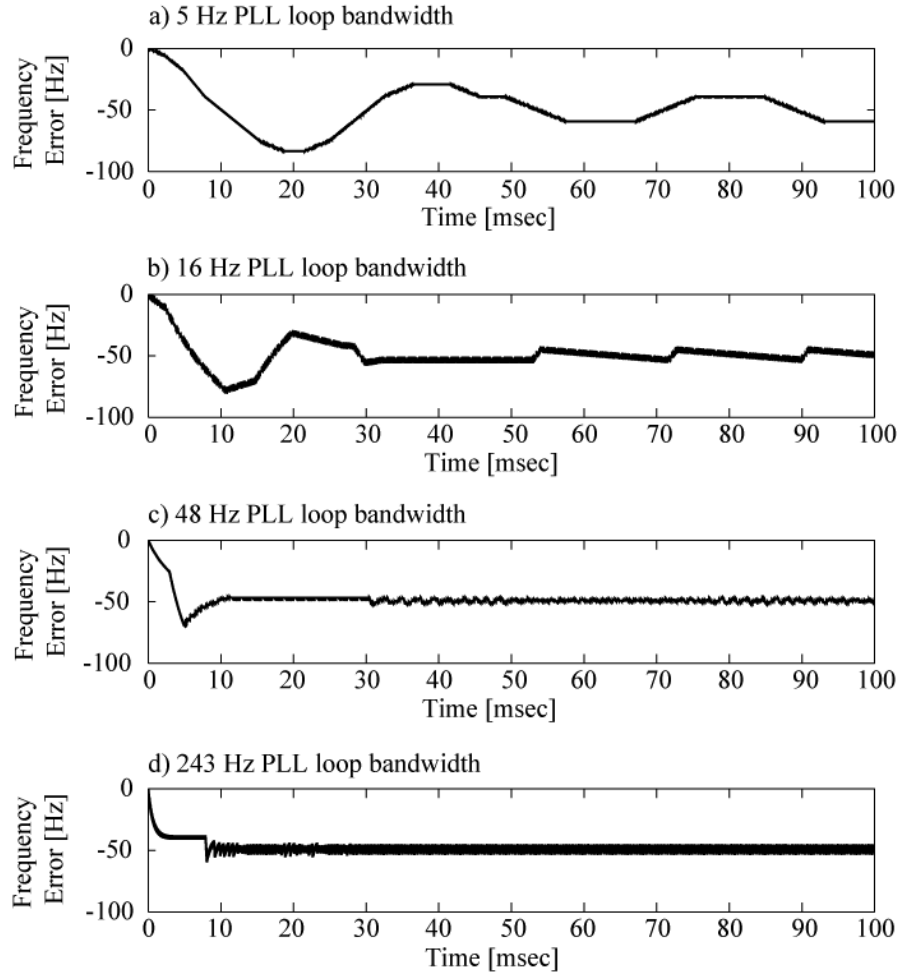


Figure 6.2: PLL lock-in performance for various PLL loop bandwidths
a) 5 Hz bandwidth, b) 16 Hz bandwidth, c) 48 Hz bandwidth, and d) 243 Hz bandwidth

Plotted in Figure 6.3 is the frequency error of the PLL as it locks onto the 20 kHz input in the presence of an additive Gaussian white noise (AGWN) source. The amplitude of the noise was chosen to give the minimum SNR (0.5) required for the PLL to lock. It can be seen from these plots that the smaller PLL bandwidths have a greater tolerance for noise. The smaller PLL bandwidths allows the PLL to ride out high frequency variations in the input signal. Higher bandwidth PLLs track the noise rather than holding the desired center frequency. The chosen PLL bandwidth for the

tone tracking system was 16 Hz. This PLL bandwidth allowed a relatively quick lock-in time of a few milliseconds while providing sufficient noise suppression.

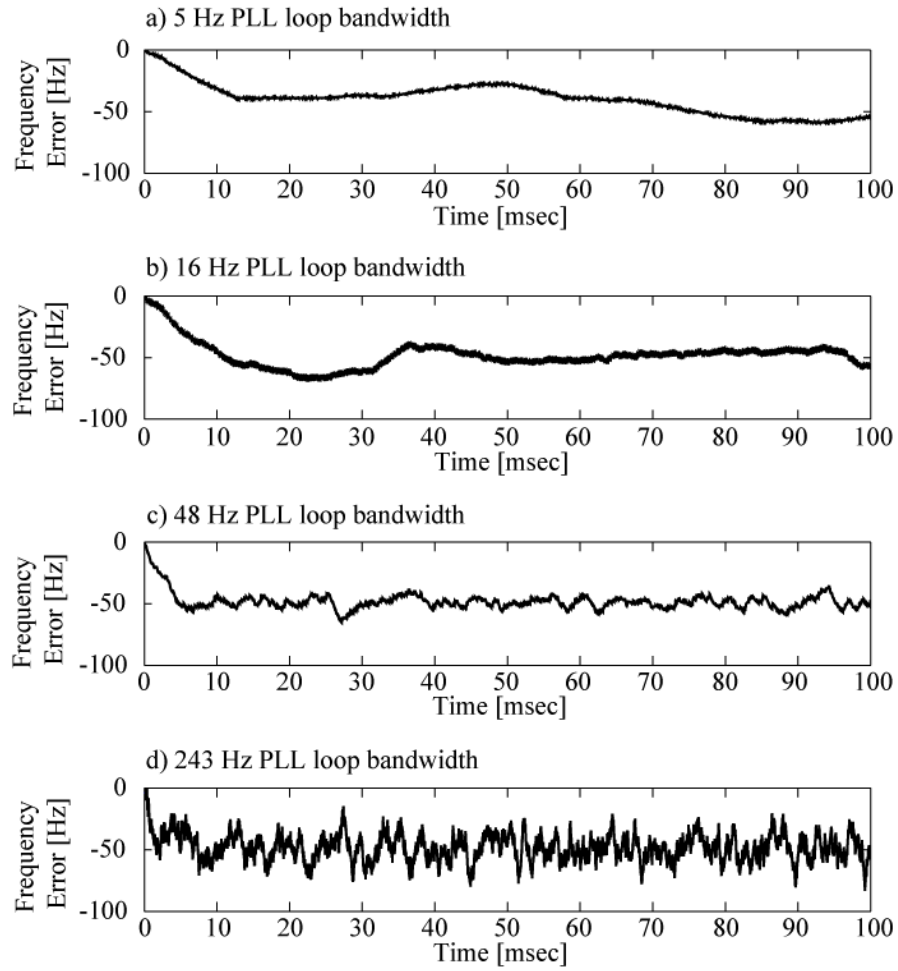


Figure 6.3: PLL lock-in performance in the presence of noise (SNR = 0.5)
a) 5 Hz bandwidth, b) 16 Hz bandwidth, c) 48 Hz bandwidth, and d) 243 Hz bandwidth

6.2 Quadcell automatic gain control

The quadcell automatic gain control adjusts the variable gain amplifier (VGA) in response to the magnitude of the sum of the demodulated quadrant detector signals. The goal of the AGC algorithm is to maintain the quadcell signal level at a moderate level within the dynamic range of the DSP analog-to-digital converter (ADC). When the quadcell signal is too low or too high there is no linear error signal for the AGC algorithm. For this reason, the algorithm incrementally adjusts the gains until the quadcell signal returns to the dynamic range of the DSP. Hysteresis in the algorithm provides a band of quadcell values for which the AGC will remain static. When the quadcell signal is within a subset of the dynamic range of the ADC the AGC is static. The hysteresis band was employed to minimize any effect the changing AGC might have on the tracking error signal.

The quadcell AGC was implemented with the same 10 kHz timer interrupt that was used for the tracking control loop. The quadcell slew rate was determined by the choice of step size. The AGC slew rate was set to 3000 dB/second. At this rate the AGC can sweep the full 82 dB of gain in 30 msec. A detailed discussion of the AGC slew rate is provided in Section 7.2.

6.3 Fast steering mirror controller

The fast steering mirror controller stabilized the fast steering mirror and allowed high frequency response to quadcell error signals. In the case of the pointing control loop, the controller stabilized the pointing mirror and allowed high frequency response to pointing commands fed-forward from the tracking system. The fast

steering mirror controller was a Proportional-Integral-Derivative (PID) controller. A PID controller derives the mirror command from the angle error signal (proportional gain), the integral of the error signal (integral gain), and the derivative of the error signal (derivative gain). A PID controller was chosen since it is a second order controller and well suited for compensating a second order mechanical system such as the fast steering mirror. This relationship will be demonstrated in detail in the following analysis.

The basic tracking loop was composed of a fast steering mirror with feed-back through a PID controller. The tracking control loop diagram is depicted in Illustration 6.1. The fast steering mirror angle was added optically to the angle of arrival error and detected by the quadcell. The four signals from the quadcell were demodulated from the 20 kHz tracking tone via the phase-locked loop then low pass filtered. The resulting 4 signals were used to calculate the angle error signals via the quadcell math. The angle error signal is input to the PID controller to calculate the mirror command signal. The PID controller is implemented for both the Azimuth and Elevation angular error although only one channel is depicted in Illustration 6.1 for simplicity. The mirror command is converted to a voice coil drive current by the FSM driver transconductance amplifier. Test points have been built into the controller circuit shown in Illustration 6.1 for swept-sine network analysis present in Chapter 7. The quadcell math equations are presented again for reference in equations (6.1) and (6.2).

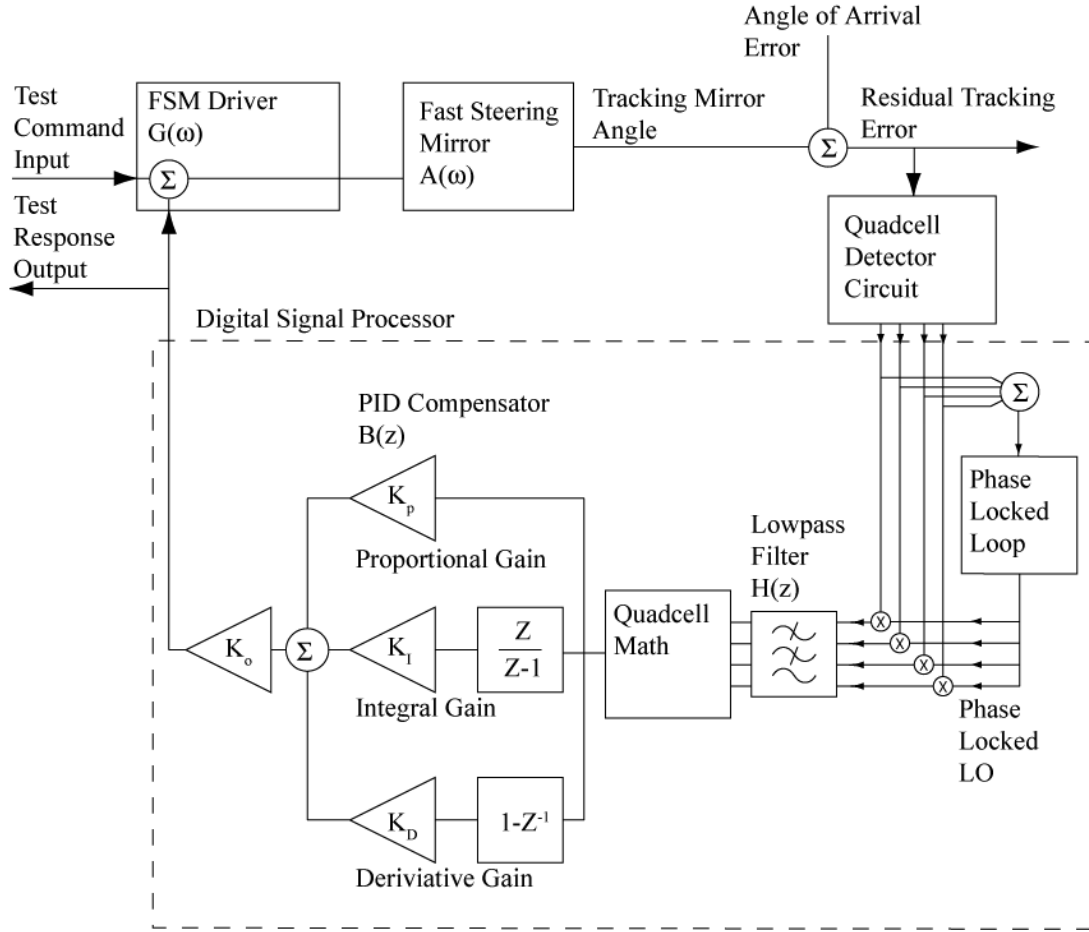


Illustration 6.1: Tracking control loop diagram

$$E_{Az} = \frac{(P_1 + P_4) - (P_2 + P_3)}{(P_1 + P_2 + P_3 + P_4)} \quad (6.1)$$

$$E_{El} = \frac{(P_1 + P_2) - (P_3 + P_4)}{(P_1 + P_2 + P_3 + P_4)} \quad (6.2)$$

The controller gain coefficients were determined using a Matlab control system model. The control loop model Matlab code is listed in Appendix D. The construction of this model began with the continuous time model for the fast steering mirror given by equation (6.3). The fast steering mirror can be parameterized by three factors. The mirror parameters are the resonant frequency, ω_o , the damping coefficient, δ , and the DC gain, k_m . This continuous time model can be converted to a discrete time model by the zero-order sample-and-hold method given by the transform in equation (6.4). The discrete time fast steering mirror model then has the form given in equation (6.5). This discrete time model was used to design the discrete time PID controller.

$$A(s) = \frac{k_m \omega_o^2}{s^2 + 2\delta \omega_o s + \omega_o^2} \quad (6.3)$$

$$A(z) = (1 - z^{-1}) L \left\{ \frac{A(s)}{s} \right\} \quad (6.4)$$

$$A(z) = \frac{A_o z + B_o}{z^2 - 2C_o z + D_o} \quad (6.5)$$

Plotted in Figure 6.4 is the measured transfer function of the Newport fast steering mirrors used in the interrogator terminal. These mirror have a resonant frequency of 10 Hz and a damping coefficient of 0.05. Also plotted in Figure 6.4 is the FSM model transfer function based on the measured FSM parameters.

Comparison of these two plots shows that the second order mirror model is an accurate representation of the FSM dynamics.

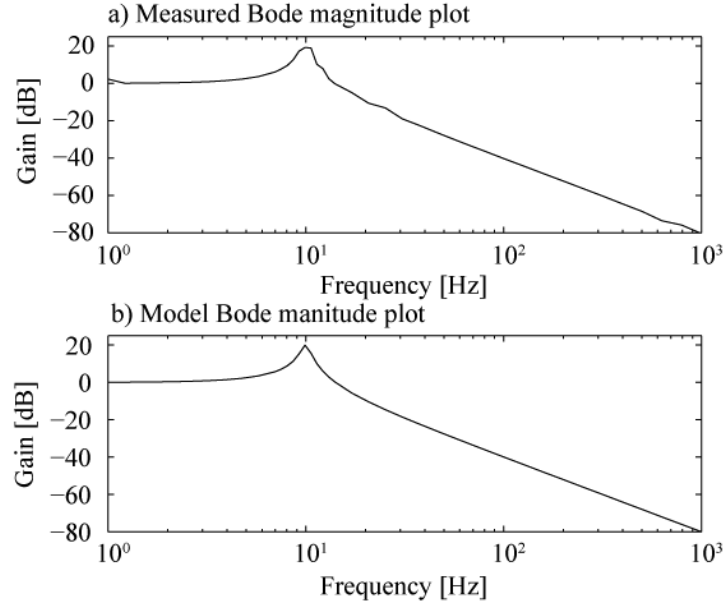


Figure 6.4: Fast steering mirror transfer function Bode magnitude plot
a) Measured, b) Modeled

The PID controller can be designed with zeros that compensate the poles in the fast steering mirror transfer function thereby eliminating the effect of the flexure resonance. For this reason, the PID controller may also be called a compensator. The analysis to calculate the appropriate PID gain coefficients begins with the difference equation for the PID mirror controller command used in the DSP. The PID difference equation is given in equation (6.6). equation (6.7) provides the expression for the error integrator, $I[n]$, used in equation (6.6). The controller gains are denoted by K_p , K_i , K_d , and K_o . These gains are the proportional, integral, derivative, and loop gain respectively.

$$CMD[n]=K_o(K_pE[n]+K_I I[n]+K_D(E[n]-E[n-1])) \quad (6.6)$$

$$I[n]=I[n-1]+E[n] \quad (6.7)$$

Using the Z transform, the controller difference equations can be rewritten as the discrete time transfer function given in Equation (6.8). The closed loop transfer function, $Q(z)$, can be found using the classic feedback Equation (6.9). Here the low pass filter, H , and the mirror driver, G , have been omitted for simplicity. The PID gains can be chosen such that the zeros of the controller transfer function, $B(z)$, cancel the poles of the fast steering mirror transfer function, $A(z)$. Making the appropriate choice of controller gains, the closed loop transfer function, $Q(z)$, can be expressed with equation (6.10).

$$B(z)=\frac{K_o((K_p+K_I+K_D)z^2-(K_p+2K_D)z+K_D)}{z^2-z} \quad (6.8)$$

$$Q(z)=\frac{A(z)B(z)}{1+A(z)B(z)} \quad (6.9)$$

$$Q(z)=\frac{K_o(A_o z+B_o)}{z^2+(K_o A_o-1)z+K_o B_o} \quad (6.10)$$

The closed loop transfer function in the form of equation (6.10) is a low-pass filter with a bandwidth determined by the loop gain K_o . This ideal form is not typically found in real-world systems due to uncertainty in fast steering mirror

parameters and additional transfer function in the loop. However, this form is convenient for determining a starting point for the loop gains.

The control loop modeling was made complete by adding the transfer functions of the low pass filter, $H(z)$, and the FSM driver transfer function, $G(\omega)$. Including these transfer functions, the complete closed loop transfer function can be expressed as in equation (6.11). In equation (6.11) $G(\omega)$, has been mapped into the discrete time transfer function, $G(z)$, by the transform given in equation (6.4). The mirror driver transfer function, $G(z)$, was modeled as the lowpass filter given in equation (6.12). The error signal lowpass filter transfer function, $H(z)$, is given in equation (6.13).

$$Q(z) = \frac{G(z)A(z)H(z)B(z)}{1 + G(z)A(z)H(z)B(z)} \quad (6.11)$$

$$G(z) = \frac{G_0 z}{z - G_1} \quad (6.12)$$

$$H(z) = \frac{H_0 z}{z - H_1} \quad (6.13)$$

The evaluation of equation (6.11) lacks the simplicity found in the analysis of equation (6.9). Since the simple closed loop expression is lost in this new expression, the controller loop gains had to be adjusted. Rather than a direct derivation from mirror parameters, the controller gains were determined through loop performance

measurements that will be presented in Chapter 7. The closed loop tracking transfer function is plotted in Figure 6.5. The plots in Figure 6.5 include both the controller modeling performance prediction as well as the measured tracking transfer function. It can be seen that there is a high degree of agreement between the modeling results and the implemented control loop performance. The measured results were measured while operating the 16 km FSO link. It can be seen in the Bode plots that the tracking system had a closed loop bandwidth of 125 Hz.

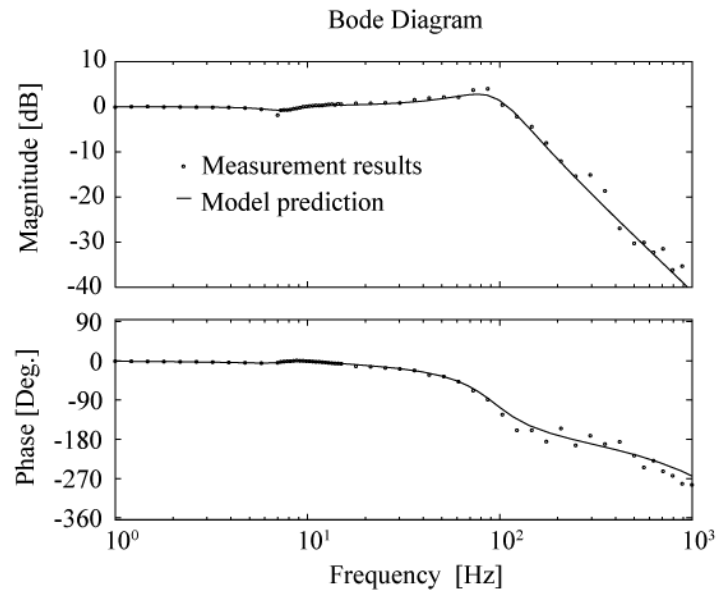


Figure 6.5: Tracking control loop Bode plots from modeling predictions and measured closed loop tracking performance

The tracking bandwidth cannot be increased arbitrarily by increasing the loop gain, K_o . The limit to the tracking bandwidth is determined by the stability of the control loop. Illustrated in Figure 6.6 is the Z-plane root locus for the tracking loop as a function of the loop gain. As the gain is increased, the poles of the tracking loop approach, then exit, the unit circle. When the poles cross the unit circle, the loop

becomes unstable. The loop gain which places the poles on the unit circle is the metastable gain. The metastable gain sets the loop at the point of oscillation. The difference between the operating gain and the metastable gain is the gain margin. The gain margin can be measured from the closed loop Bode plot in Figure 6.5 and has a value of 10 dB. However, the root locus analysis provides the underlying cause of the loop stability.

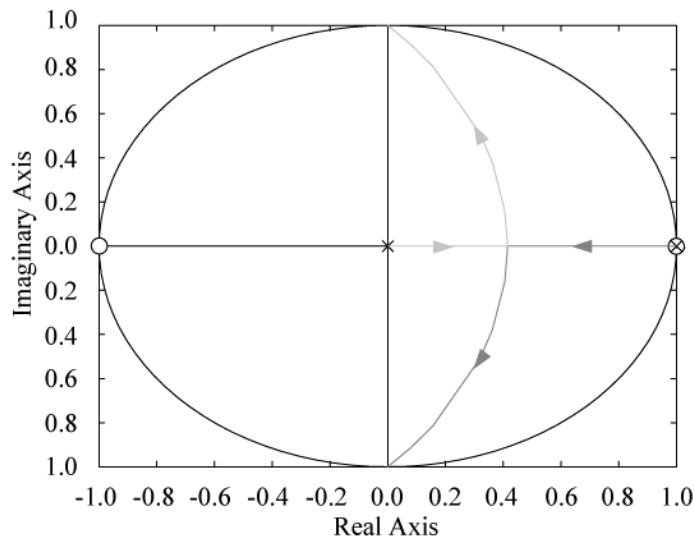


Figure 6.6: Closed loop controller model root locus for loop gain K_o

Based on the previous modeling, a PID controller was implemented using fixed point math for the C6416 fixed point digital signal processor. The sampling rate for the controller was 10 kHz and was derived from an internal timer. Fixed point math was used for the compensator calculations to utilize the high speed operation of the fixed point DSP. The controller gains, derived from the modeling results, were implemented in base-two exponent and mantissa form. The gains were normalized relative to the smallest gain term, the integral gain. This normalization was required

to make all the loop gains integer values. The overall loop gain was restricted to powers of $\frac{1}{2}$ such that the loop gain could be implemented with a simple right shift operation.

The pointing controller was very similar to the tracking controller. The primary difference in the two controllers is that the error signal for the pointing control was derived from internal position sensors in the pointing fast steering mirror. Input from the tracking mirror position sensors were added to the pointing mirror control. This enabled the point-ahead capability of the pointing and tracking. So as the tracking mirror tracked the incoming return beam, the pointing mirror would move in synchronization to keep the transmitter pointed correctly. The tracking mirror position was low-pass filtered to eliminate noise from being fed to the pointing mirror control. The pointing mirror control diagram is given in Illustration 6.2.

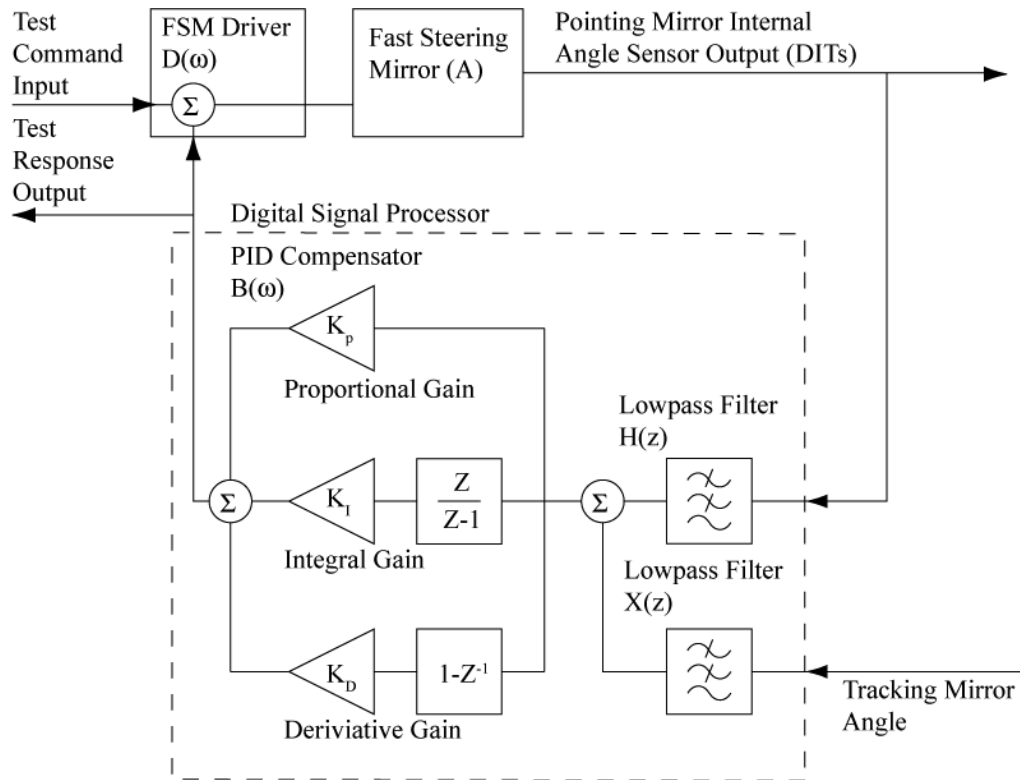


Illustration 6.2: Pointing fast steering mirror control diagram

The same PID controller structure was used for the pointing as was used for tracking. However, the controller gain values have changed due to differences in the sensor response functions and the error signal low pass filters. Plotted in Figure 6.7 are the closed loop Bode plots for the modeled pointing control along with the measured result. The bandwidth of the pointing mirror controller was 175 Hz. The pointing mirror controller was designed with more bandwidth than the tracking controller to ensure the pointing mirror could accurately follow the motion of the tracking mirror.

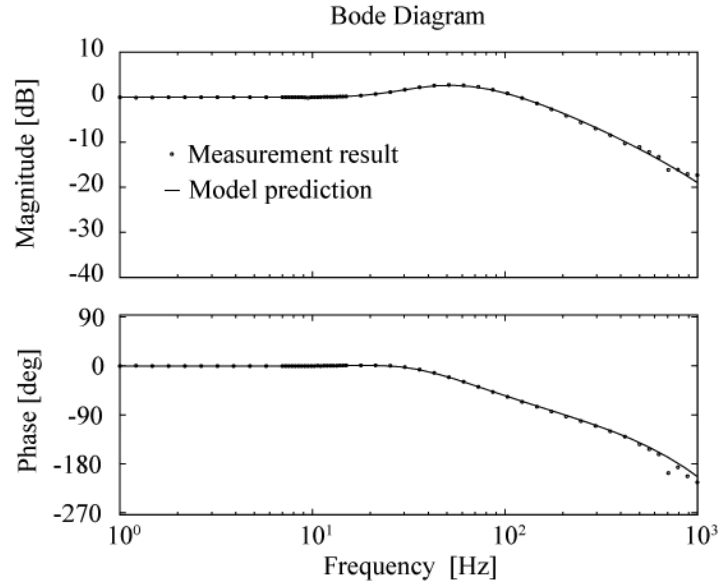


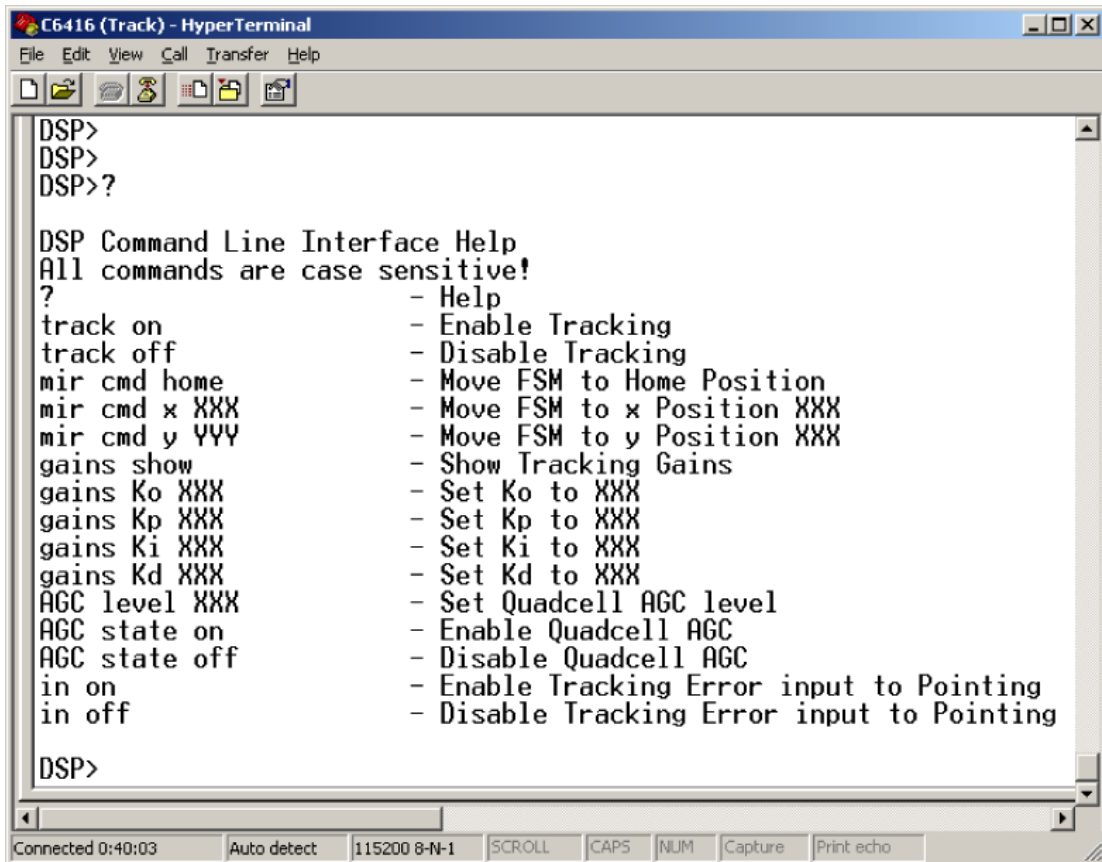
Figure 6.7: Pointing control loop Bode plots from modeling predictions and measured closed loop pointing performance

6.4 User interfaces

The embedded software provided three user interfaces. The main user interface was the serial port command line interface. The embedded software also included LED outputs and DIP switch inputs. The LED outputs were used to indicate PLL lock and mirror out-of-range error. The PLL lock LED indicated the phase lock loop had acquired the tracking tone based on the phase error as will be described in Section 7.1. The mirror out-of-range LED was lit when the FSM was commanded to the limit of its range of motion. This indicator was provided to warn the user if the mirror was being over driven and possibly damaged. A DIP switch was used to configure the software for pointing or tracking mirror control. When the DIP switch was set, the unit would identify itself as a pointing DSP. A pointing DSP takes its compensator inputs from the mirror internal position sensors as opposed to the

quadcell error signal. When identified as a pointing DSP, the point-a-head algorithm became available for activation. By default, the unit identified itself as a tracking DSP and configured itself with the tracking compensator gains and executed the quadcell PLL.

The serial port interface was developed to provide user interaction with the pointing and tracking systems. Using Microsoft's HyperTerminal application, serial commands could be sent to the DSP. The user could enable or disable tracking, quadcell AGC, and the point-ahead feature. In addition, the user could change the various gain settings associated with each of the pointing and tracking algorithms. This feature was employed extensively in the link testing to determine the optimal pointing and tracking gain settings. The command line interface is shown in Figure 6.8. The list of available commands can be seen in Figure 6.8 as well.



```
DSP>
DSP>
DSP>?

DSP Command Line Interface Help
All commands are case sensitive!
?
- Help
track on          - Enable Tracking
track off         - Disable Tracking
mir cmd home      - Move FSM to Home Position
mir cmd x XXX     - Move FSM to x Position XXX
mir cmd y YYY     - Move FSM to y Position XXX
gains show        - Show Tracking Gains
gains Ko XXX      - Set Ko to XXX
gains Kp XXX      - Set Kp to XXX
gains Ki XXX      - Set Ki to XXX
gains Kd XXX      - Set Kd to XXX
AGC level XXX     - Set Quadcell AGC level
AGC state on      - Enable Quadcell AGC
AGC state off     - Disable Quadcell AGC
in on             - Enable Tracking Error input to Pointing
in off            - Disable Tracking Error input to Pointing

DSP>
```

Figure 6.8: Pointing and tracking DSP command line interface

Chapter 7 Tracking performance

The performance of the interrogator pointing and tracking system was tested *in situ* on the 16 km link. The pointing and tracking testing involved testing the five major components of the pointing and tracking systems. These five components are the tone tracking phase-locked loop, the quadcell AGC, the pointing mirror controller, the tracking mirror controller, and the point-ahead control of the pointing mirror.

7.1 Phase-locked loop

The performance of the phase-locked loop was determined by two loop parameters. These parameter were the tracking bandwidth and the lock-in time. The tracking bandwidth of the PLL was 150 Hz. The PLL tracks input frequencies in the range of 19070 Hz to 20120 Hz. This range was intentionally offset from 20000 Hz to allow the detection of a phase-lock by thresholding the phase error. When the loop locks onto the 20 kHz tone the phase error accumulator will have a value of -50 Hz. A threshold of -25 Hz was used to determine that the loop was locked. Illustrated in Figure 7.1 is the measurement of the lock-in time of the PLL. Here the input tracking tone is plotted along with the PLL lock indicator. It can be seen in this plot that after 2.75 msec the PLL achieves lock. This lock-in time is in agreement with the PLL model presented in Chapter 6. The lock-in time is critical to the design of link acquisition algorithms. During acquisition, many links will perform a spiral scan of the transmitter to acquire the link. The spiral scan must not sweep the transmitted beam at a rate faster than the PLL can lock.

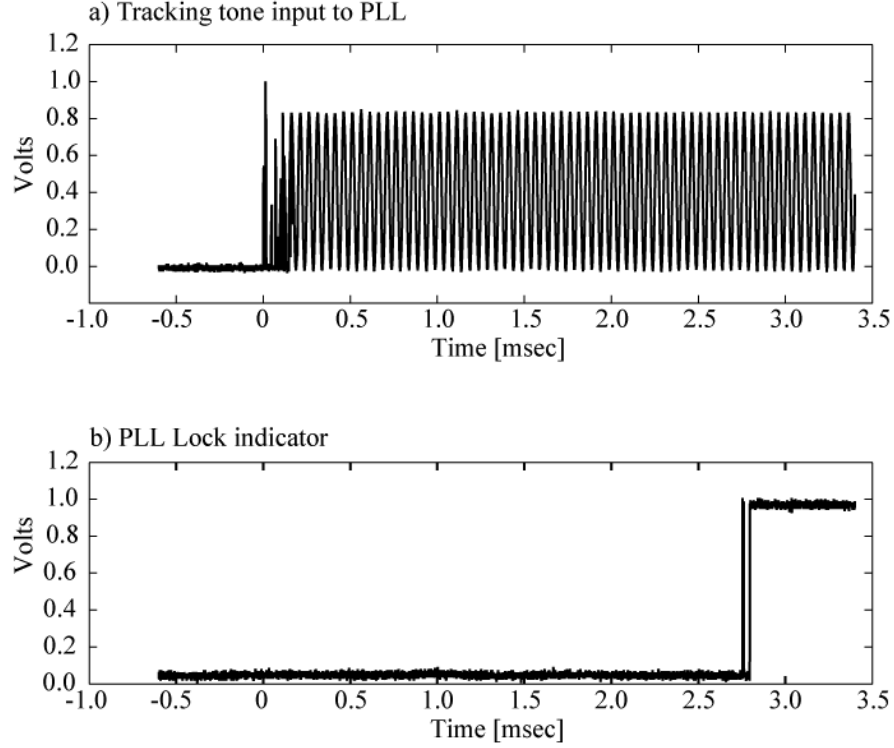


Figure 7.1: Measurement of the phase-locked loop achieving lock
a) Input 20 kHz tone to the PLL, b) PLL lock indicator output

7.2 Quadcell automatic gain control (AGC)

The performance of the automatic gain control was tested *in situ* on the 16 km link in the presence of atmospheric turbulence. The quadcell AGC algorithm was operated with various gain step sizes. The step size corresponds to the slew rate of the VGA gain. AGC using a larger step size is able to respond to changes in the quadcell signal level faster. The step size cannot be made too large or the signal will never fall into the hysteresis band and the AGC will oscillate. Plotted in Figure 7.2 are the quadcell signals and the AGC response for three values of AGC step size. It can be seen that, as the step size is increased, the AGC responds more quickly. AGC resulted in an increased quadcell signal mean value and fewer periods where the

signal fades. The units of the quadcell AGC setting are 16 bit integer counts. The maximum AGC setting value was 65576. These counts can be related to the gain of the VGA by the factor of 0.0015 dB/count. A step size of 20 counts corresponds to a step size of 0.03 dB. Since the AGC loop runs at a sampling rate of 10 kHz, the slew rate for a 20 count AGC step is 300 dB per second. At this slew rate the full 82 dB of gain offered by the AD604 can be swept in 0.3 seconds. The final step size of 200 counts provided a slew rate of 3000 dB/second which could sweep the full gain range in 30 msec.

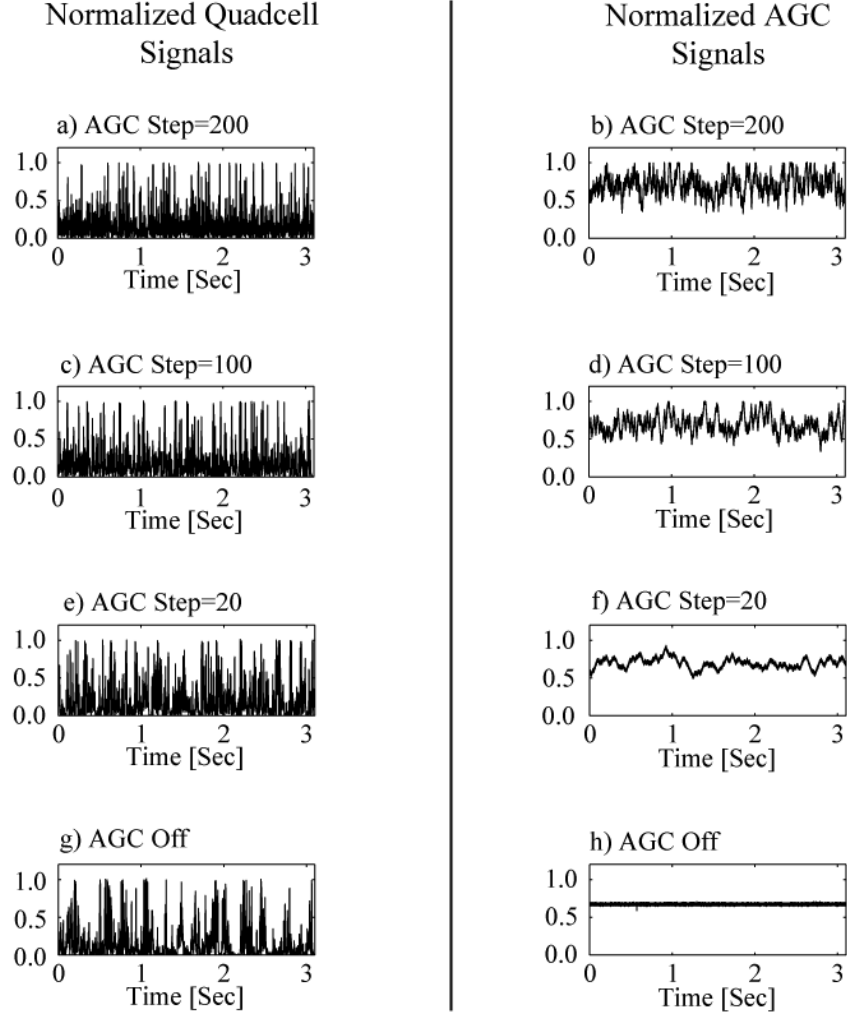


Figure 7.2: Quadcell AGC performance for various step sizes
a-b) Step = 200 counts, c-d) Step = 100 counts, e-f) Step = 20, g-h) No AGC

The effect of the AGC in reducing the quadcell signal variance can also be represented in the frequency domain. Plotted in Figure 7.3 are the power spectral density curves for quadcell signals with various AGC step sizes. It can be seen that, as the step size is increased, the low frequency power fluctuations in the quadcell signal are reduced. In this sense, the step size can be seen as increasing the bandwidth of the AGC.

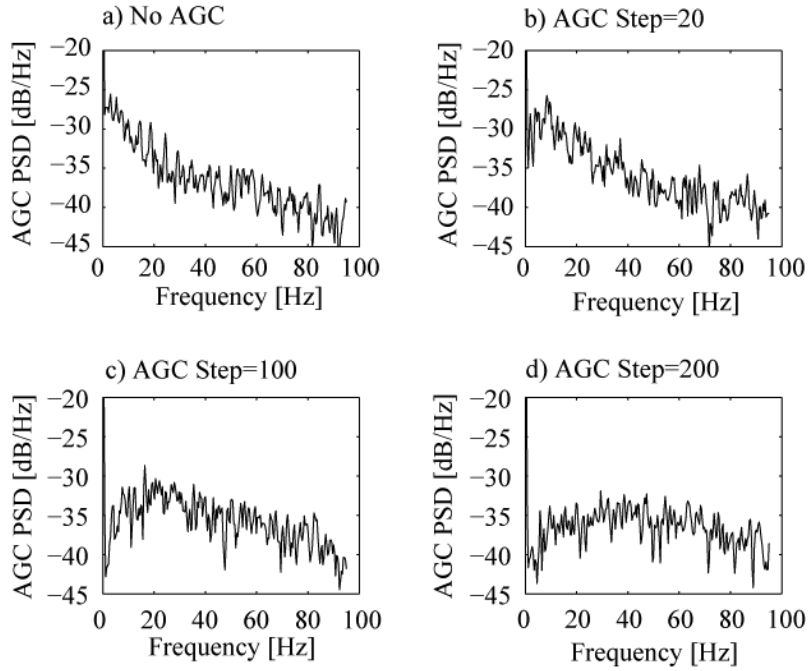


Figure 7.3: Quadcell signal power spectral density plots for various AGC step sizes
a) No AGC, b) Step = 20 counts, c) Step = 100 counts, d) Step = 200 counts

7.3 Pointing mirror control loop

The pointing mirror controller was optimized and characterized *in situ* on the FSO link. The optimizing of the PID controller began with gain values determined from the control model for canceling the fast steering mirror resonance. These gains provided a starting point for optimizing the performance of the pointing controller. The controller gains were optimized empirically to accommodate variability between the the system parameters used in the controller modeling and the actual system parameters. The optimization of the controller employed time domain step response measurements as well as frequency domain transfer function measurements.

7.3.1 Pointing mirror time domain controller optimization

The pointing mirror controller gains were initially optimized by step response measurements. Plotted in Figure 7.4 is the uncompensated mirror response to a step command input. The uncompensated mirror takes 4 seconds to stabilize after the application of the step input. The over shoot is nearly 100% and the resonant frequency is 10Hz.

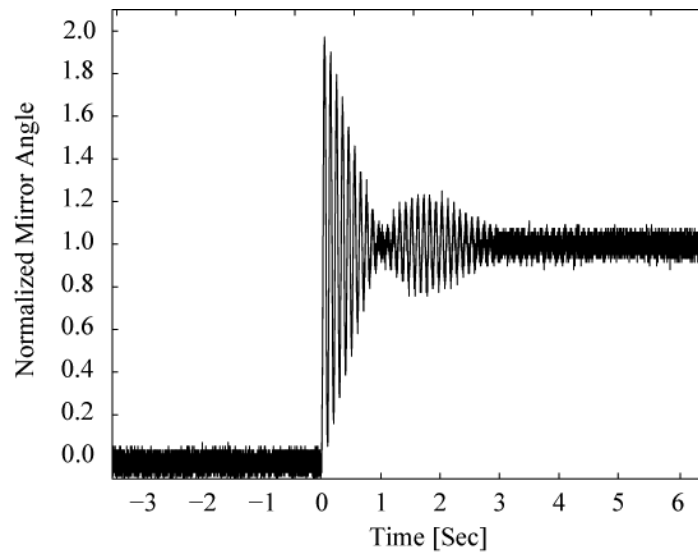


Figure 7.4: Open loop fast steering mirror step response

Plotted in Figure 7.5 are the closed loop mirror step responses for various values of the proportional gain. The proportional gain effects the overshoot as well as the settling of the response. Based on these measurements, the proportional gain was set to 100. This gain setting provided a quick step response with little overshoot. A gain of 200 could also be employed as it also provided a quick response with little overshoot. It will be shown later that a proportional gain of 200 has undesirable

effects in the frequency domain. Based on both time domain and frequency domain measurements the final proportional gain was set to 100.

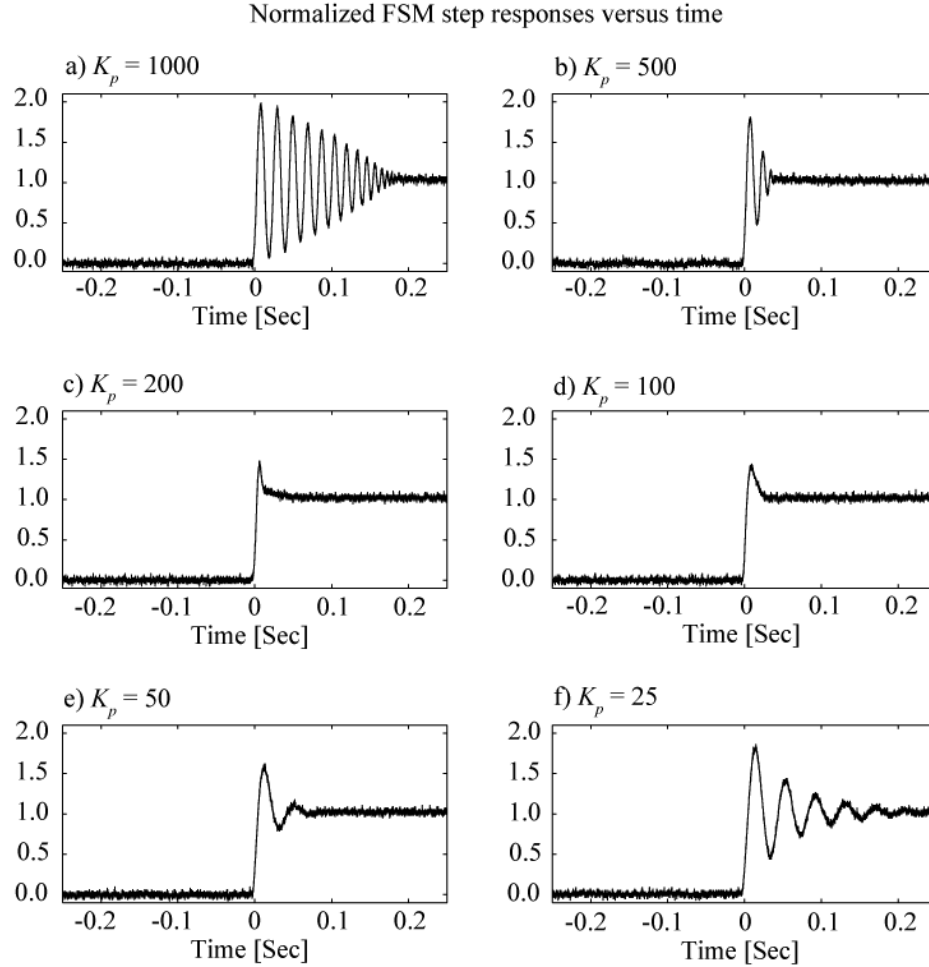


Figure 7.5: Pointing fast steering mirror step responses for various proportional gain values
a) $K_p = 1000$, b) $K_p = 500$, c) $K_p = 200$, d) $K_p = 100$, e) $K_p = 50$, and f) $K_p = 25$

The next gain value to be optimized was the derivative gain. Plotted in Figure 7.6 are the step responses for various derivative gain values. It can be seen from these plots that the derivative gain effects the speed of the mirror response as well as the settling time. Based on these plots a derivative gain of 4000 was chosen for the

controller. This provided a quick response with little overshoot. Plotted in Figure 7.7 is the optimized pointing mirror controller step response.

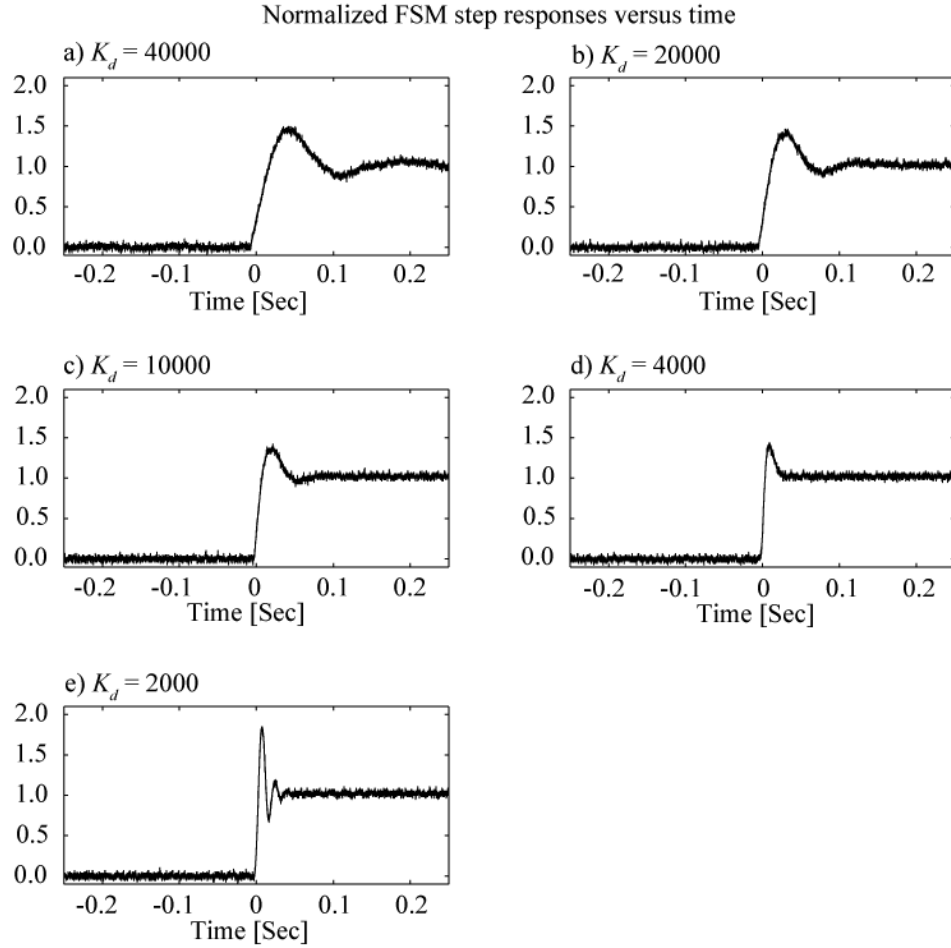


Figure 7.6: Pointing fast steering mirror step response curves for various derivative gain values
a) $K_d = 40000$, b) $K_d = 20000$, c) $K_d = 10000$, d) $K_d = 4000$, and e) $K_d = 2000$

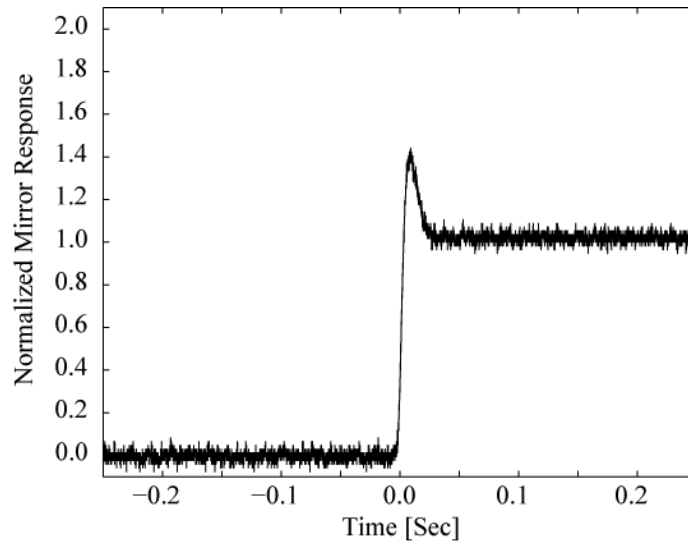


Figure 7.7: Controlled fast steering mirror step response with optimized controller gain settings

The overall compensator loop gain, K_o , was initially determined by starting with a low gain setting and increasing the gain until the loop became unstable. The loop gain was then backed down by a factor of 8 for the step response testing of the previous section. This overall loop gain provided a gain margin of about 8 such that the loop was well within the region of stable operation. This overall gain setting was validated using frequency response techniques in the next section. The overall loop gain determined by both methods was similar.

To facilitate implementation on a fixed point DSP, the loop gains were normalized to the smallest of the gains. This gain was the integral gain which was set to 1 in the fixed point representation. For this reason the integral gain was not varied. However, the response of the controller is dependent on the relative value of the loop gains so there was no loss in generality by making this normalization.

7.3.2 Pointing frequency domain controller optimization

The performance of the pointing mirror compensator was measured in the frequency domain by swept-sine transfer function analysis. The performance metric for these tests was the closed loop transfer function of the pointing mirror controller. The closed loop transfer function was measured for various values of the proportional, derivative, and overall loop gain terms. Again, due to the nature of the fixed point calculations, the integrator gain was fixed to a value of 1. The pointing mirror compensator transfer function was measured using an audio frequency network analyzer, Siglab, manufactured by Spectral Dynamics. The Siglab output was connected to the command summing node of the mirror current driver. The Siglab input was connected to the controller mirror command output. The Siglab test points in the pointing mirror control system are shown in Illustrated in Figure 7.1.

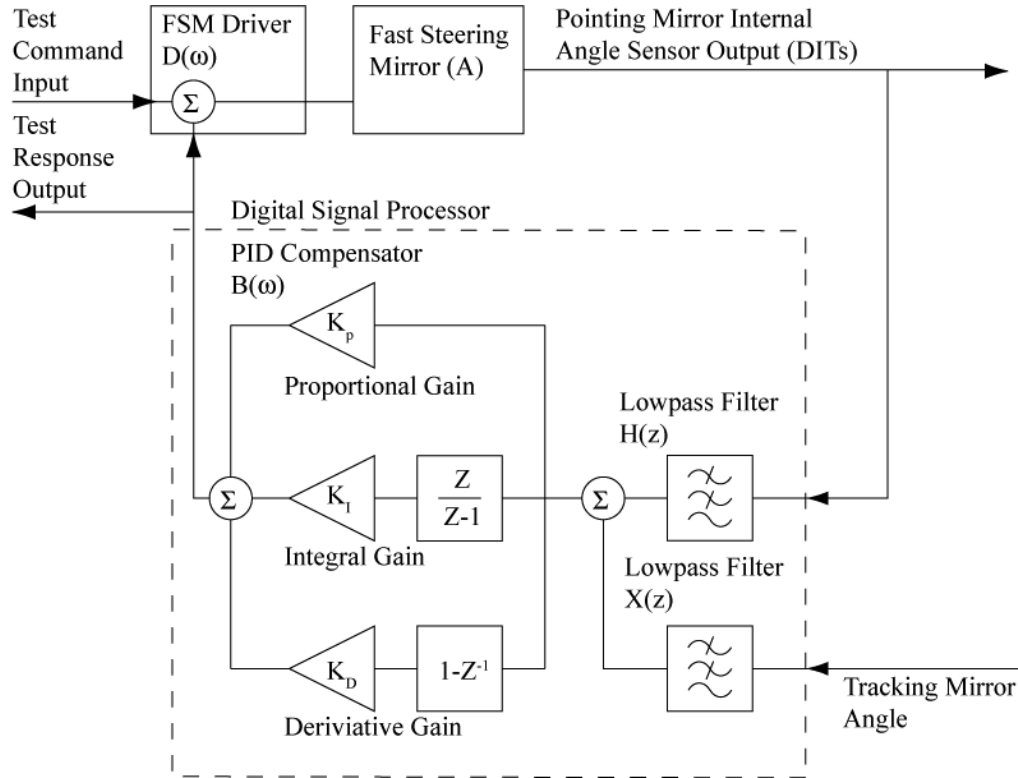


Illustration 7.1: Pointing controller system diagram with measurement test ports

The first compensator gain to be varied was the proportional gain. Plotted in Figure 7.8 are the Bode plots of the closed loop transfer functions of the pointing mirror compensator for various values of the proportional gain. The desired transfer function is a first order low pass filter with sufficient tracking bandwidth (~ 100 Hz). It can be seen in these plots that the proportional gain term effects the deviation of the transfer function from a first order transfer function to a second order transfer function. Gain above 0 dB is undesirable as that indicates that the loop is over-responding at those frequencies. Positive gain up-to 6 dB can be tolerated without significant performance degradation. It can be seen that a proportional gain of 100

provides a minimal amount of positive gain in the closed loop transfer function. This was the final value chosen for the proportional gain.

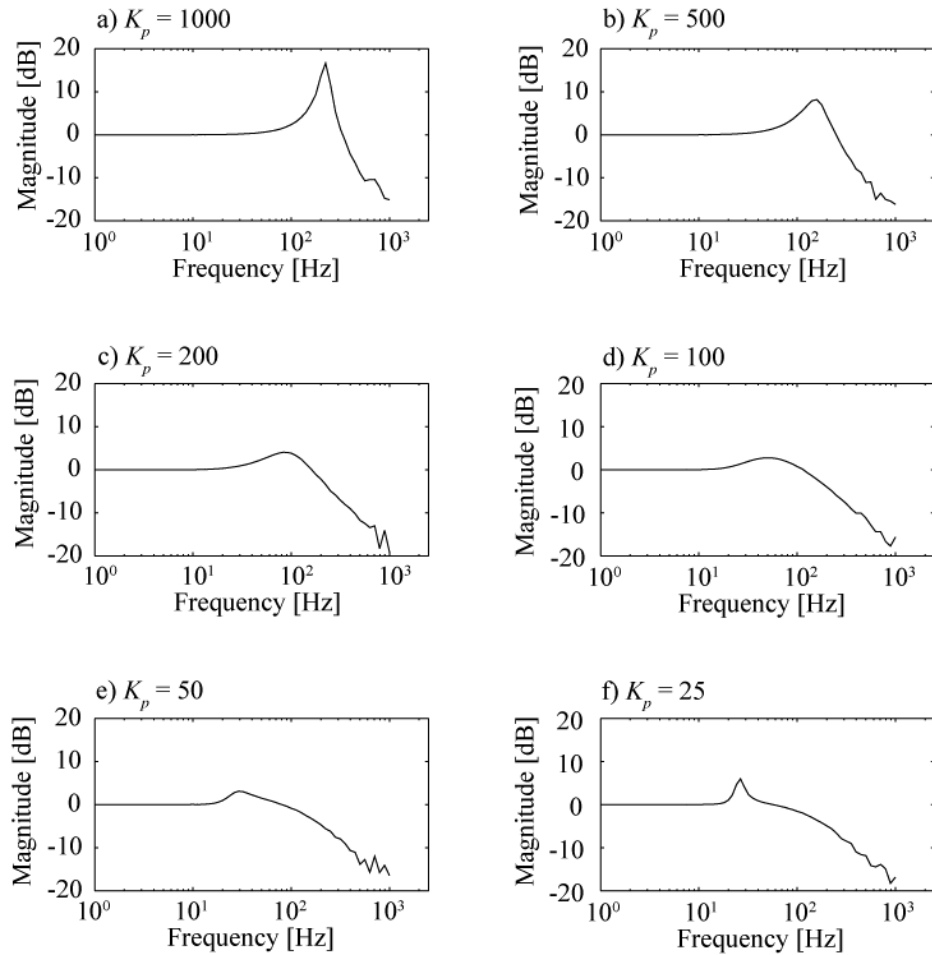


Figure 7.8: Pointing closed loop transfer function for various proportional gain values
a) $K_p = 1000$, b) $K_p = 500$, c) $K_p = 200$, d) $K_p = 100$, e) $K_p = 50$, and f) $K_p = 25$

The closed loop transfer function was measured for various values of the derivative gain. Plotted in Figure 7.9 are the transfer functions for various derivative gains. It can be seen here that the value of 4000 provides little positive gain. Although the plot for a derivative gain of 10000 appears optimal, the step response of

this gain setting was not as good as a setting of 4000. The gain setting of 4000 was chosen for the final derivative gain so as to provide a good step response as well as a good transfer function.

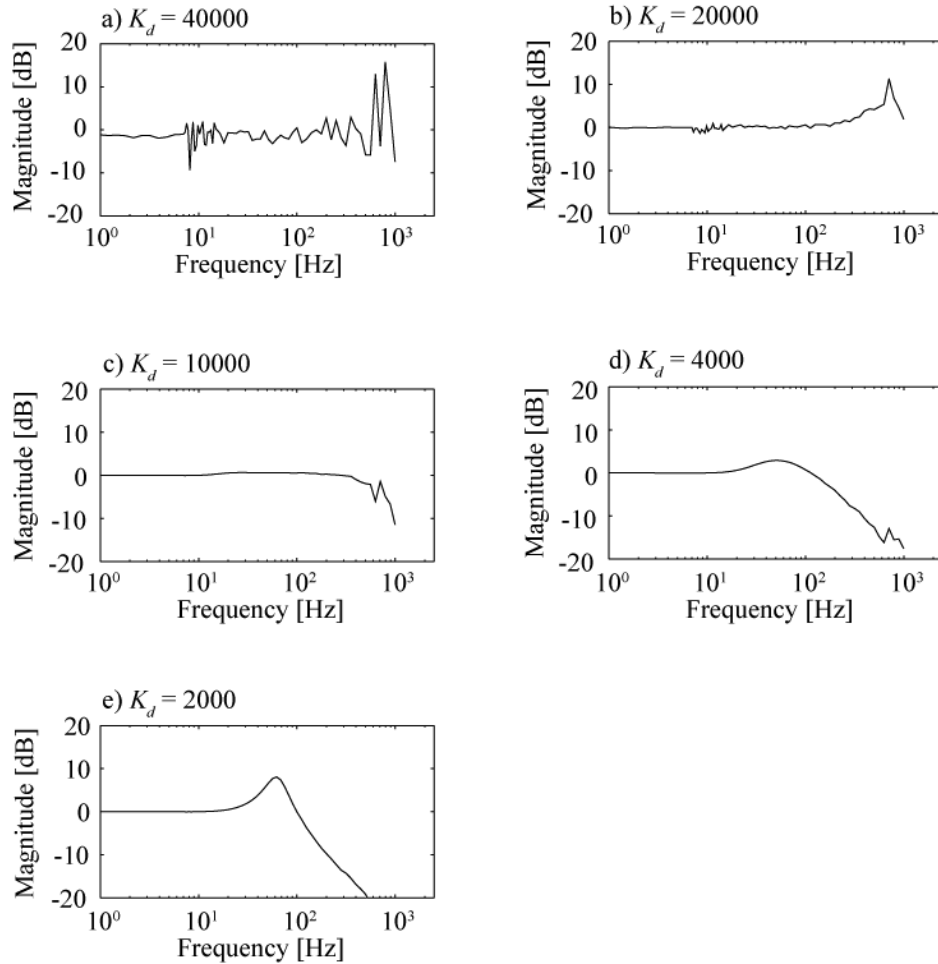


Figure 7.9: Pointing controller transfer functions for various derivative gain values
a) $K_d = 40000$, b) $K_d = 20000$, c) $K_d = 10000$, d) $K_d = 4000$, and e) $K_d = 2000$

The final loop gain value to be evaluated was the overall loop gain, K_o . The overall loop gain is the major determinant of the controller bandwidth but it may also effect the shape of the transfer function. For this reason, a series of transfer function

measurements were taken for various loop gain values. Plotted in Figure 7.10 are the controller transfer functions for various loop gain values. The loop gain was implemented as a shift operation in the DSP so all the loop gain values are powers of $\frac{1}{2}$.

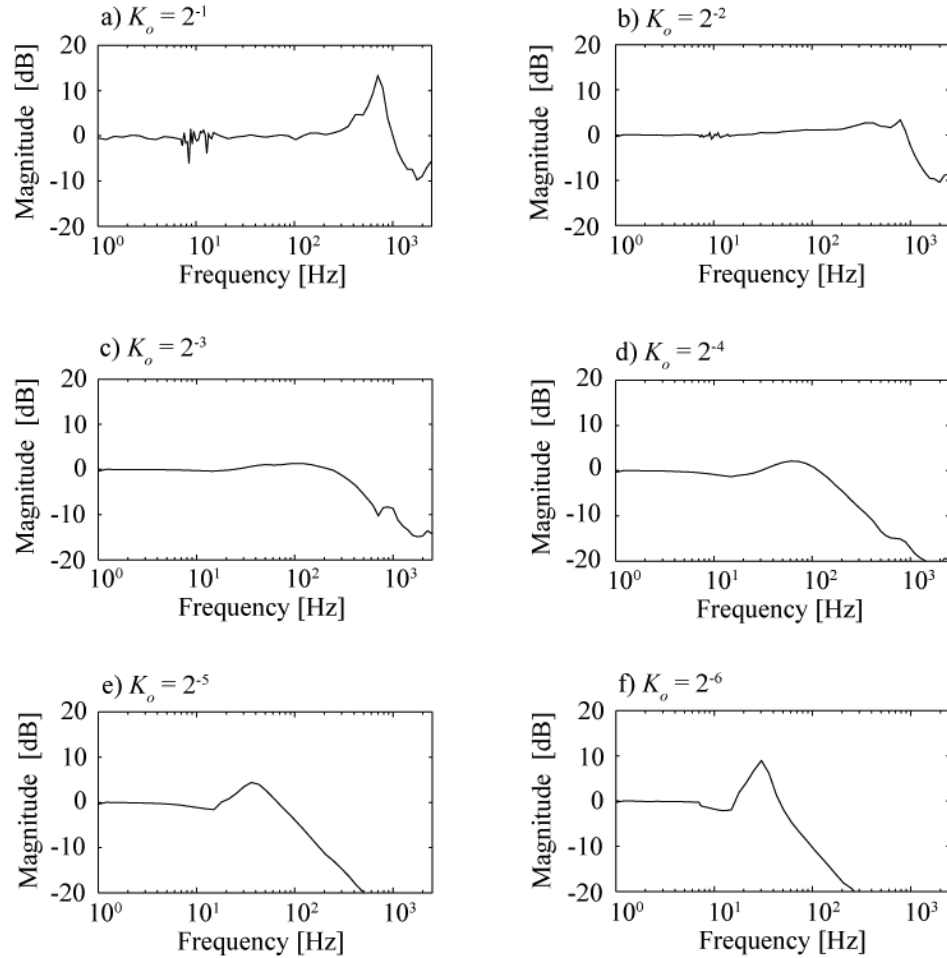


Figure 7.10: Pointing controller transfer functions for various overall loop gains
a) $K_o = 2^{-1}$, b) $K_o = 2^{-2}$, c) $K_o = 2^{-3}$, d) $K_o = 2^{-4}$, e) $K_o = 2^{-5}$, and f) $K_o = 2^{-6}$

The final loop gains for the pointing controller were 100, 1, 4000, and 2^{-4} for the proportional, integral, derivative, and overall loop gains respectively. The bandwidth of the pointing mirror controller was 175 Hz. Plotted in Figure 7.12 is the

closed loop Bode plot for the pointing mirror control along with the modeling results from Section 6.3.

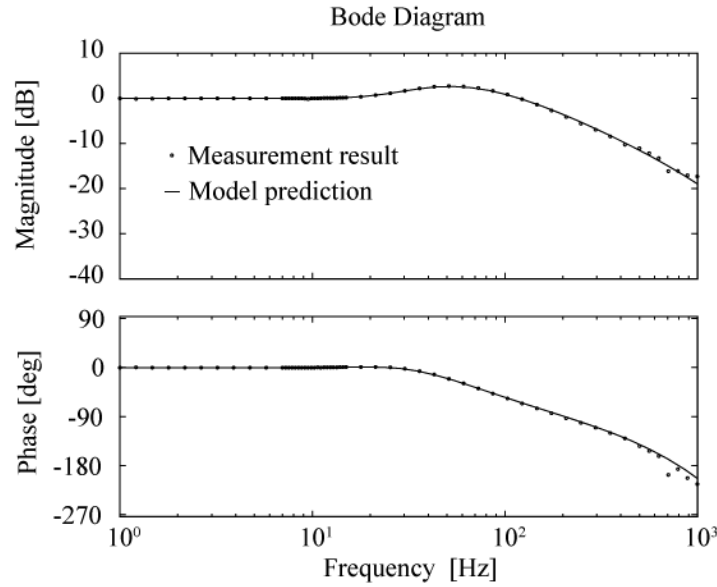


Figure 7.11: Pointing control loop Bode plots from modeling predictions and measured closed loop pointing performance

7.4 Tracking mirror control loop

The tracking mirror compensator was optimized in a fashion similar to the tuning of the pointing mirror compensator. The tracking performance was measured in three ways. First, step response data was taken for various compensator gain values. Second, closed loop transfer functions were measured for various compensator gain values. Finally, the residual error signal was measured while the tracking system corrected disturbances. These disturbances included an injected 5 Hz

disturbance used to simulate vibration. Also, the inherent angle of arrival error disturbance on the FSO link was corrected by the tracking system.

The tracking compensator optimization was performed, *in situ*, during normal operation of the FSO laser link. The tracking loop was operated with signals from light returned from the retro-reflectors. This was necessary since the loop gain of the compensator is dependent on the spot size focused on the quadrant detector. This spot size is determined by the size of the array and the prevailing atmospheric conditions. For this reason, the tracking compensator testing had to be tested on the actual link and could not be simulated in the lab. It is extraordinary that the quadrant detector provided sufficient SNR over a 16 km link to enable accurate measurements of the tracking performance.

7.4.1 Tracking time domain controller optimization

The tracking compensator gains were initially set using values derived from the compensator model in Section 6.3. To optimize the tracking controller gains, step response and transfer function measurements were taken for various values of the proportional, derivative, and overall loop gains. First, the proportional gain was varied. Plotted in Figure 7.12 are the step responses from the tracking loop for various proportional gain values. The gain value chosen for the final setting was 100, although a gain value of 500 had a shorter settling time. It will be shown in the next section that the gain value of 500 had a transfer function with an undesirable amount of positive gain for certain frequencies.

Normalized FSM step response curves

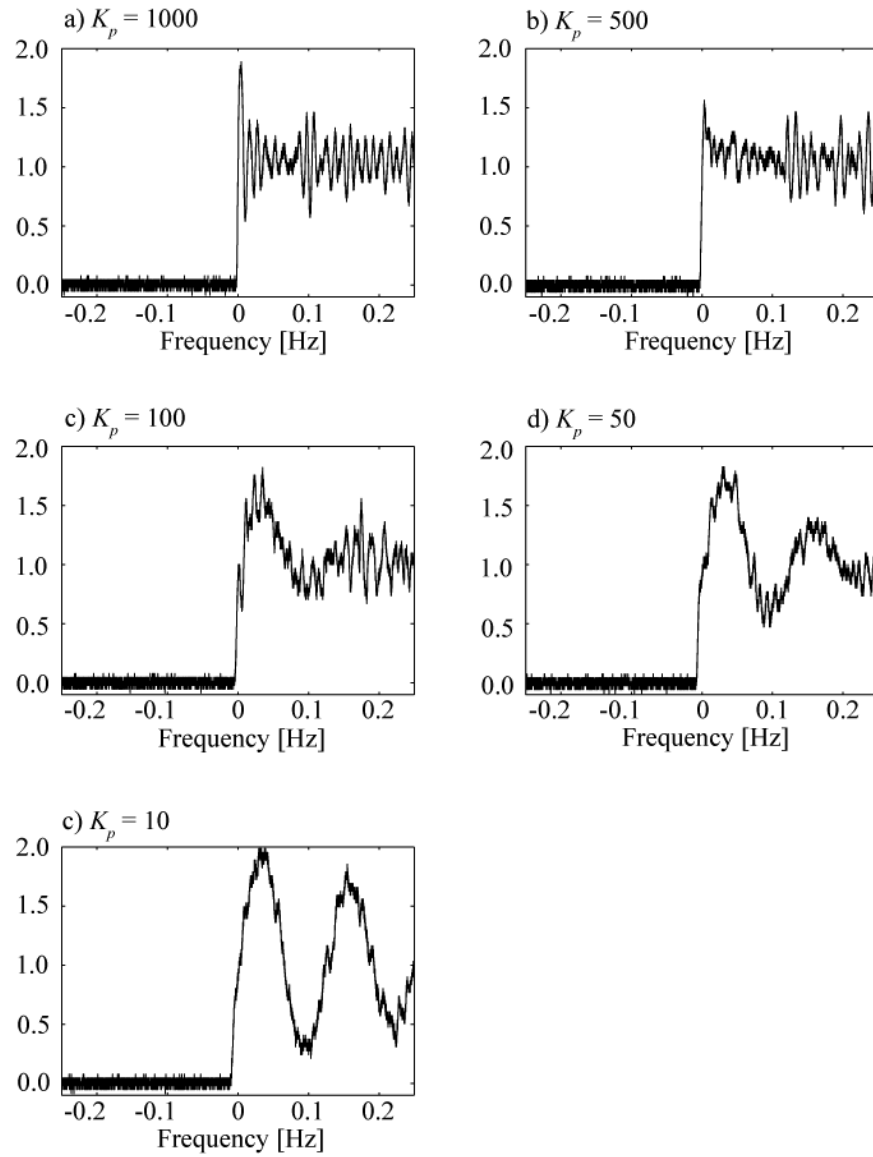


Figure 7.12: Tracking controller step response for various proportional gain values
a) $K_p = 1000$, b) $K_p = 500$, c) $K_p = 100$, d) $K_p = 50$, and e) $K_p = 10$

The step response of the tracking loop was measured for various derivative gain settings. Plotted in Figure 7.13 are the step responses for the various derivative gain settings. A derivative value of 40000 was chosen. This gain setting seemed to provide a quick response with little overshoot.

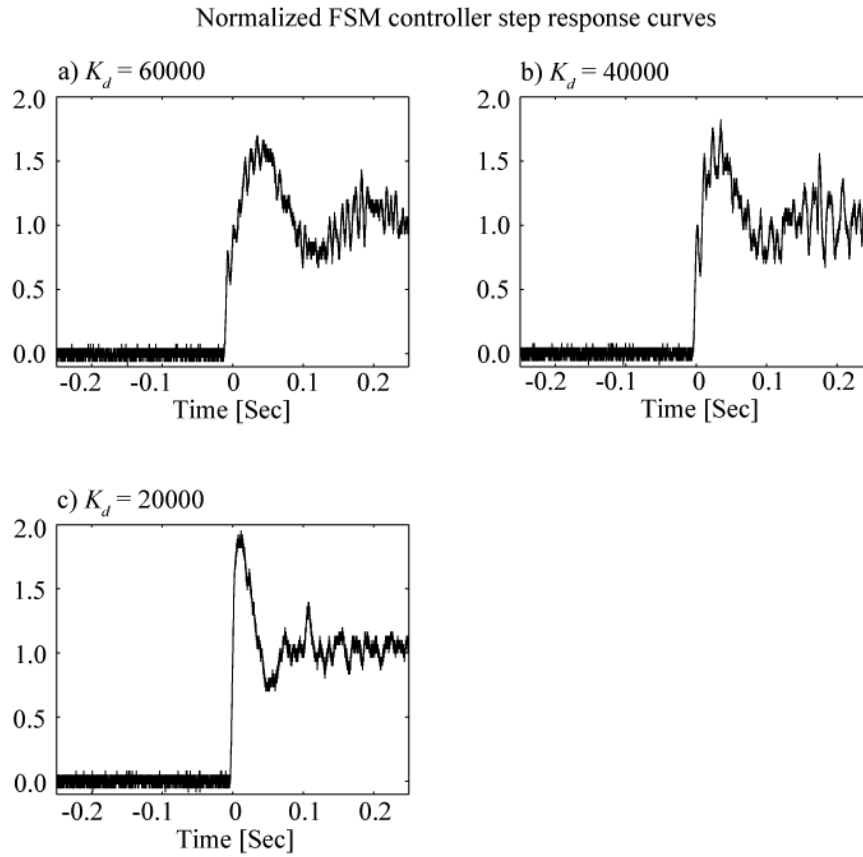


Figure 7.13: Tracking FSM controller step response curves for various derivative gain values
a) $K_d = 60000$, b) $K_d = 40000$, and c) $K_d = 20000$

The performance of the loop was measured in the presence of an injected disturbance to simulate vibration. The disturbance was an additional mirror command signal injected into the loop at a summing node in the FSM driver. This input was also used for the swept-sine transfer function measurements. The additional mirror command signal simulates terminal base motion. A 5 Hz, 200 μ rad disturbance was injected into the tracking loop. Plotted in Figure 7.14a is the quadcell error signal in the presence of the disturbance signal. This is the error signal with tracking off. Plotted in Figure 7.13b-7.13d are the residual error signals with tracking turned on for various overall loop gains. These plots show the residual

disturbance signal after the tracking loop attempted to compensate the disturbance. The three tracking plots demonstrate the reduction in residual disturbance as the loop gain is increased.

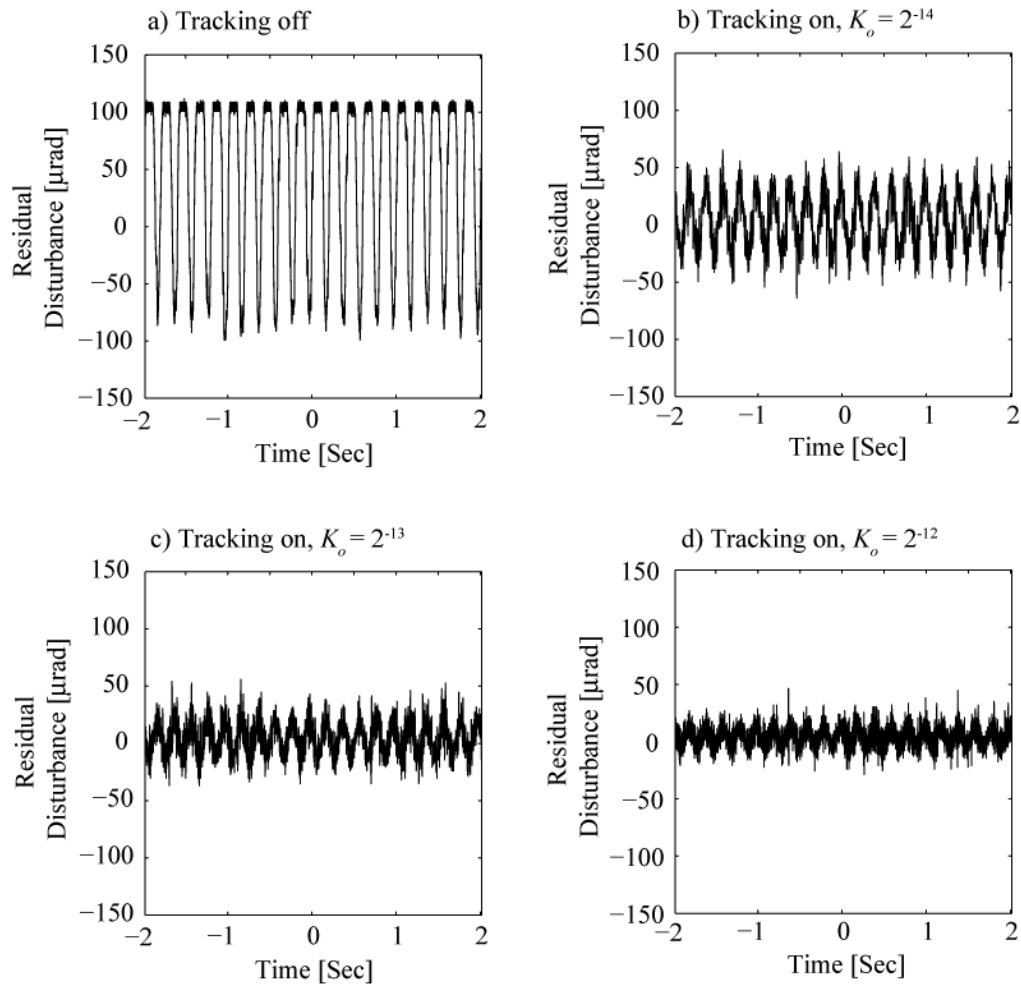


Figure 7.14: Tracking disturbance rejection
a) tracking off, b) $K_o = 2^{-14}$, c) $K_o = 2^{-13}$, d) $K_o = 2^{-12}$

Plotted in Figure 7.15 is the power spectral density (PSD) of the error signal, with and without tracking, for four different values of the overall loop gain. The

higher loop gains reduced the residual disturbance but can increase the noise in higher frequencies. This was due to the positive gain in the closed loop transfer function as the loop gain is increased. The final operating gains for the tracking loop correspond to Figure 7.14c. These gains provided sufficient disturbance rejection without injecting too much high frequency noise. Listed in Table 7.1 are the quadcell error signal variances with and without tracking for the loop gain values in Figure 7.15.

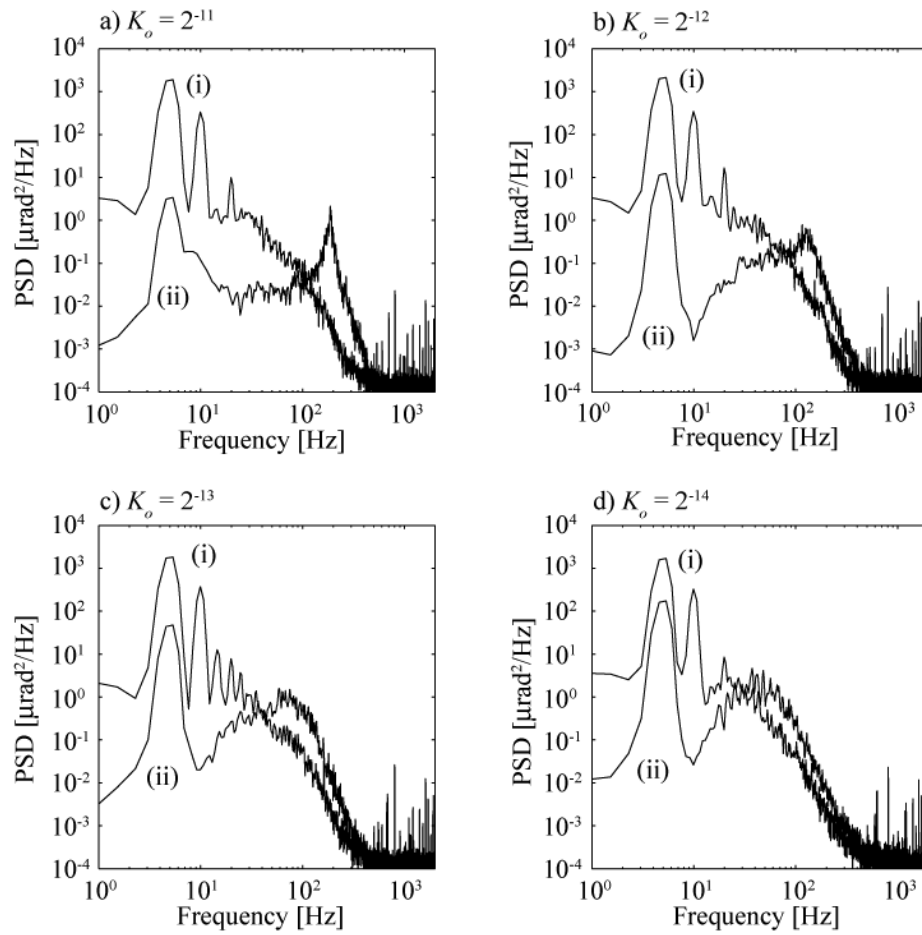


Figure 7.15: Tracking compensation power spectral density plots, with tracking (ii), and without tracking (i) for various values of overall loop gain
a) $K_o = 2^{-11}$, b) $K_o = 2^{-12}$, c) $K_o = 2^{-13}$, and d) $K_o = 2^{-14}$

Loop Gain	2^{-11}	2^{-12}	2^{-13}	2^{-14}
Uncompensated Angle Error [μrad]	72	76	72	69
Residual Angle Error [μrad]	8	9	14	23

Table 7.1: Tracking error comparison in the presence of a 5 Hz disturbance

The overall loop gain for the tracking loop ($K_o = 2^{-13}$) is substantially smaller than the pointing loop ($K_o = 2^{-4}$). This was due to large difference in the DC gain of the respective position sensors. The quadcell is a tremendously sensitive position sensor with a DC gain 45 times larger than the internal position sensor of the FSM.

7.4.2 Tracking frequency domain controller optimization

In addition to step responses, transfer function measurements were also used to optimize the tracking compensator gains. The transfer function measurement was similar to the transfer function measurements taken on the pointing control loop. The test points for the transfer function measurements are shown in Illustration 7.2. The important difference between the two measurements is the position sensor SNR. The pointing compensator gets a error signal from the FSM internal position sensors. The internal position sensors provided a consistent, high SNR, error signal for the pointing compensator. The tracking compensator gets an error signal from the quadcell. Since the quadcell error signal was dependent on the atmospheric link, the SNR was highly dynamic. This creates some defects in the transfer function measurements. Despite this challenge, transfer function measurements were still possible. This was due to the tremendous sensitivity of the quadcell circuit and the high bandwidth of the quadcell AGC. It was quite remarkable to complete a complicated transfer function measurement on an actively tracking free-space laser link.

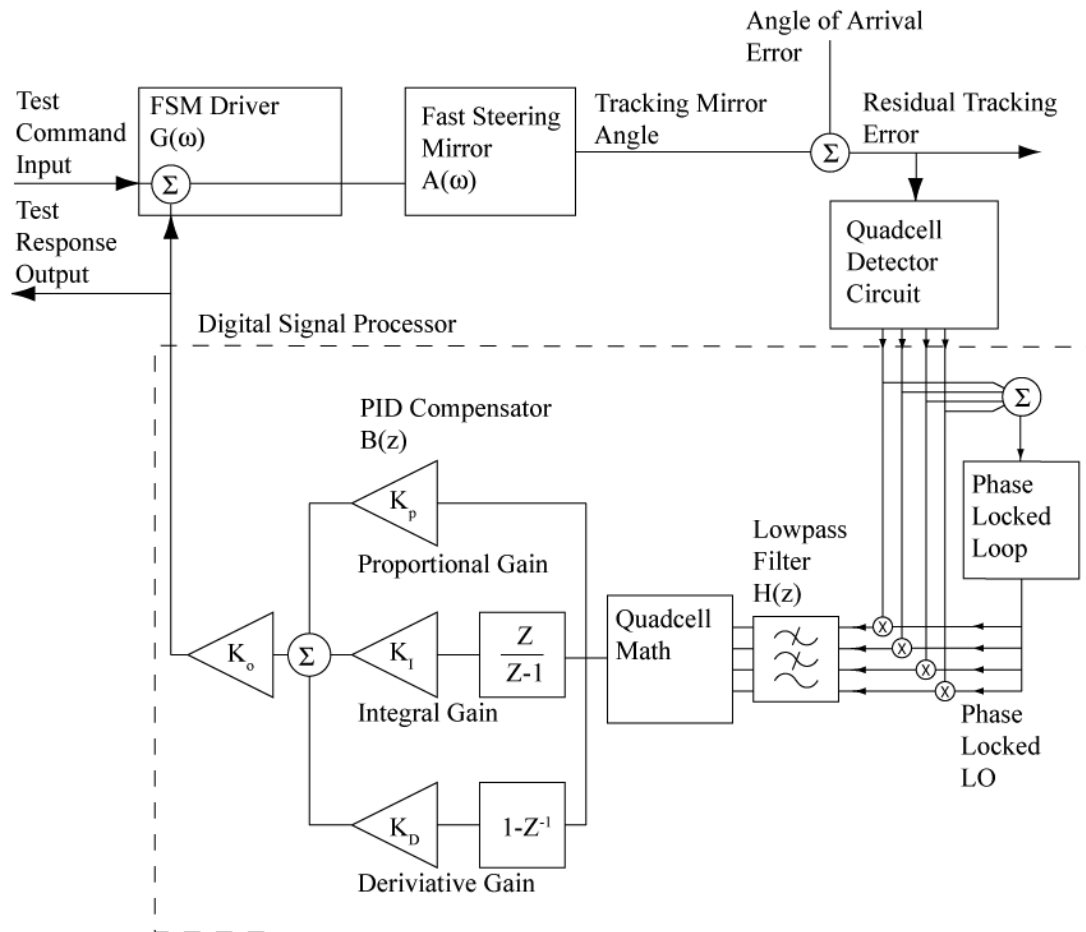


Illustration 7.2: Tracking control loop diagram

The first tracking controller gain to be optimized was the proportional gain. Plotted in Figure 7.16 are the transfer functions of the closed loop tracking system for various proportional gains. The final proportional gain was chosen to be 100. This choice offered a low positive gain region, while maintaining sufficient step response performance.

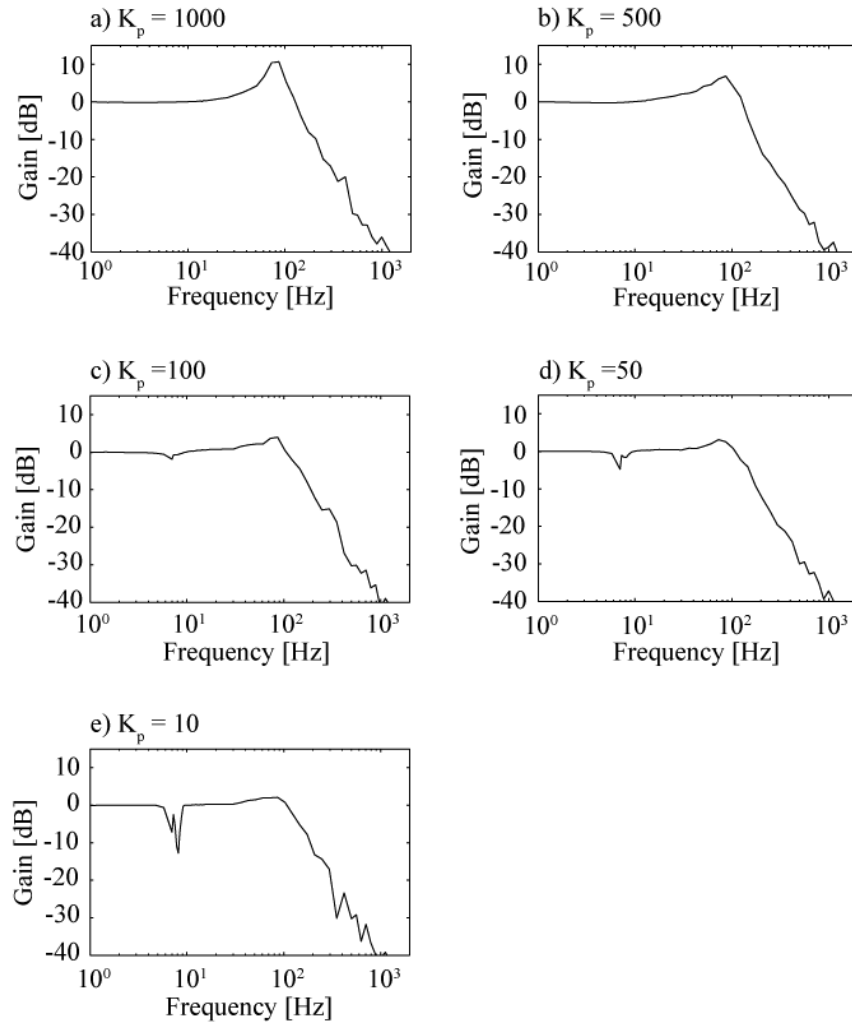


Figure 7.16: Tracking closed loop transfer functions for various proportional gains
a) $K_p = 1000$, b) $K_p = 500$, c) $K_p = 100$, d) $K_p = 50$, and e) $K_p = 10$

The next compensator gain to be optimized was the derivative gain term. Plotted in Figure 7.17 are the transfer functions of the tracking compensator for various derivative gain values. Based on these curves, a derivative gain of 40000 was chosen. This gain provided a quick step response without too much positive gain. The large dip in the transfer function for a derivative gain of 20000 was due to a momentary drop in SNR during the measurement. These kinds of errors were unavoidable when measuring the transfer functions on an active link. It was

remarkable that the majority of the transfer function could be accurately measured with only a few data points being corrupted by signal fading.

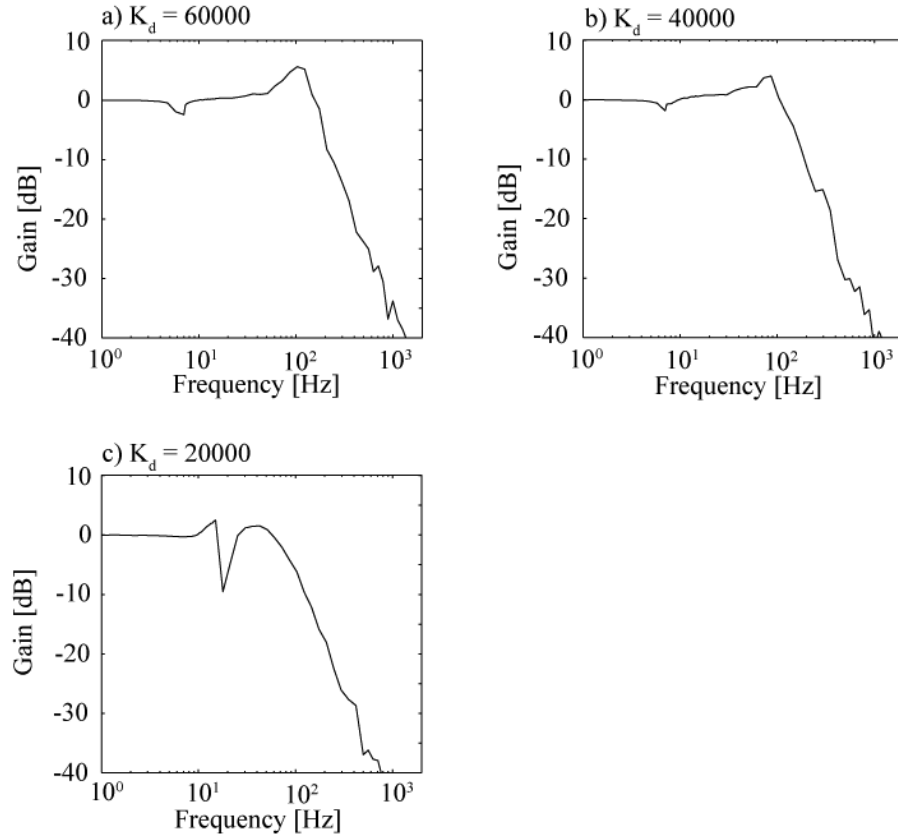


Figure 7.17: Tracking closed loop transfer functions for various derivative gains
a) $K_d = 60000$, b) $K_d = 40000$, and c) $K_d = 2000$

The final gain to be optimized was the overall loop gain. Plotted in Figure 7.18 are the transfer functions of the tracking controller for various loop gains. It can be seen from these plots that the closed loop bandwidth increases with the loop gain. However, the positive gain region increases as the loop gain approaches the limit of loop stability.

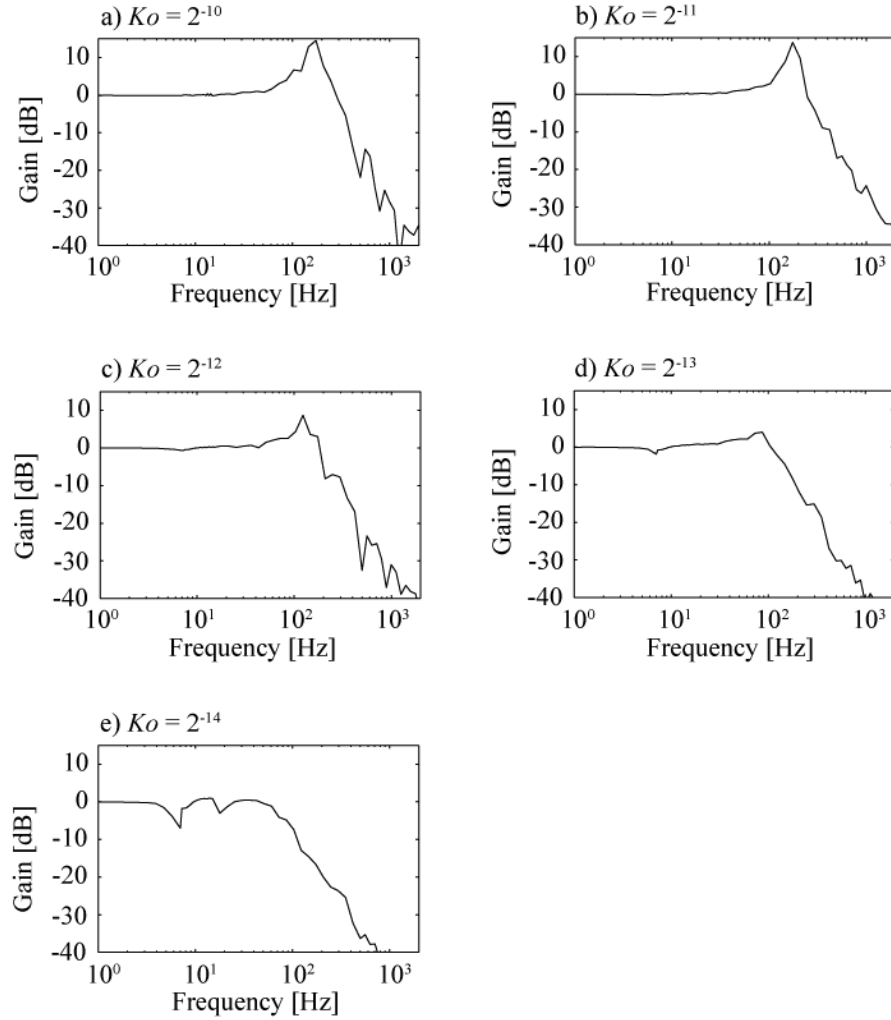


Figure 7.18: Tracking closed loop transfer functions for various overall loop gains
a) $K_o = 2^{-10}$, b) $K_o = 2^{-11}$, c) $K_o = 2^{-12}$, d) $K_o = 2^{-13}$, and e) $K_o = 2^{-14}$

From the closed loop transfer function plots and from loop stability observations a loop gain of 2^{-13} was chosen. Plotted in Figure 7.19 is the measured and modeled closed loop transfer functions (Bode plot) of the tracking controller using the final optimized gains. The closed loop tracking system has a bandwidth of 125 Hz as shown in Figure 7.19. From this Bode plot, the gain and phase margins can be extracted. The gain margin was 8 dB and the phase margin was 80 degrees. These

margins provided a sufficient stability margin to allow the loop to operate in a stable manner in the presence of a dynamic atmosphere [82].

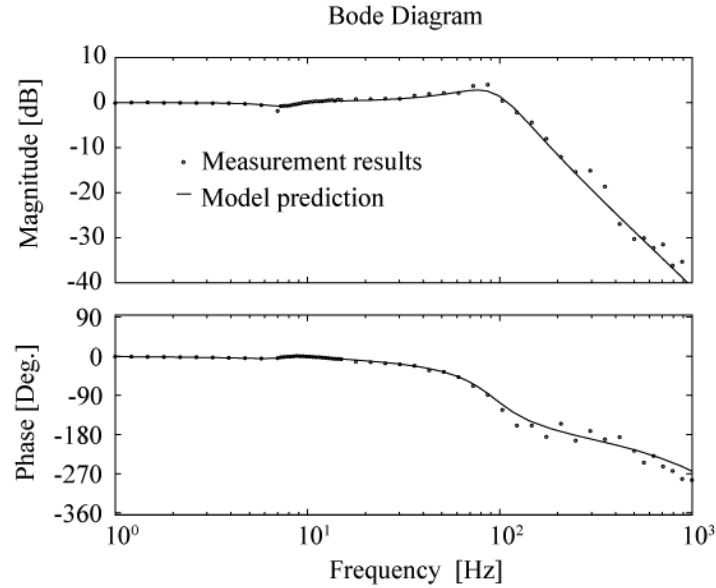


Figure 7.19: Tracking control loop Bode plots from modeling predictions and measured closed loop tracking performance

7.5 Tracking atmospheric turbulence

This section describes the successful operation of the tracking system to correct the atmospheric turbulence induced angle of arrival error. Plotted in Figure 7.20 are the PSD curves for the quadcell error signal with and without tracking. Without tracking, the quadcell error signal is a measurement of the atmospheric angle of arrival error. It is assumed that the vibration environment was negligibly small on the optical table on which the terminal was mounted. The assumption that the angle of arrival error was mainly atmospheric turbulence induced was supported by the broadband nature of the error signal. Vibration error signals are typically narrow

band when generated by typical vibration sources such as fans or other mechanical systems. It can be seen in Figure 7.20 that the tracking system could compensate a large amount of the atmospheric angle of arrival error. This tracking data was taken on 11/27/2006. The scintillation index on the link was on average 1.87 that day. This was a moderately strong scintillation case. Listed in Table 7.2 is the reduction in angle of arrival error provided by 4 different loop gain settings. As the loop gain is increased, the residual angle error was decreased.

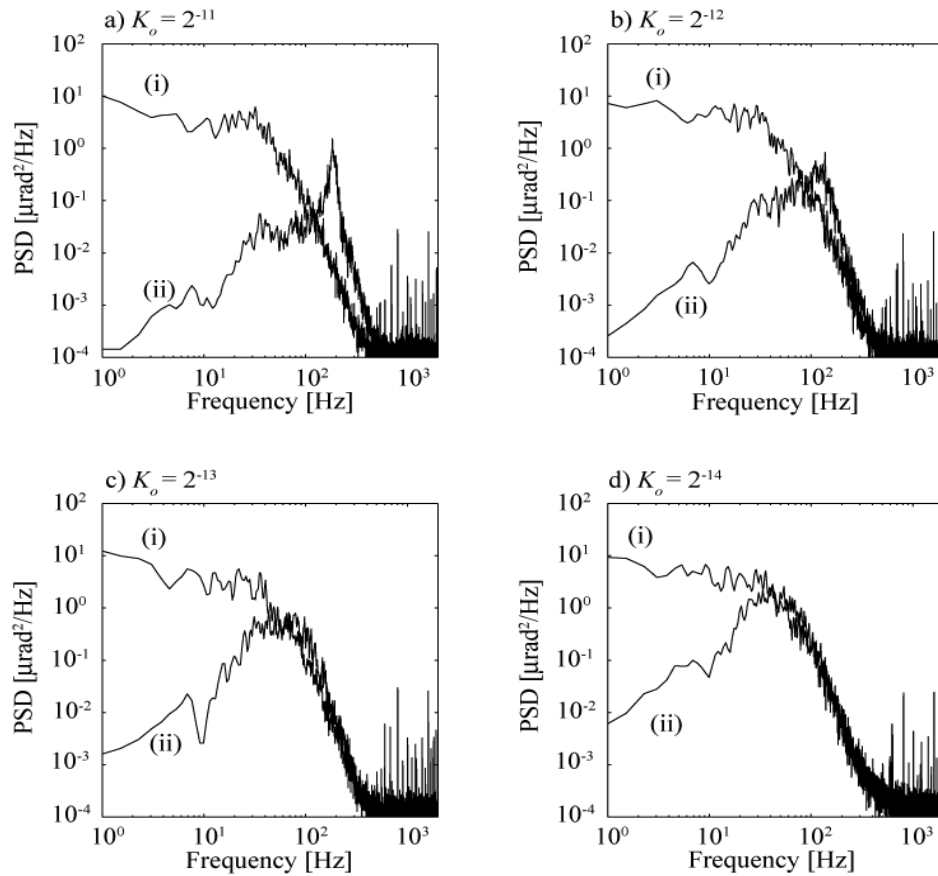


Figure 7.20: Tracking compensation of atmospheric angle of arrival error for various loop gain values a) $K_o = 2^{-11}$, b) $K_o = 2^{-12}$, c) $K_o = 2^{-13}$, and d) $K_o = 2^{-14}$

Loop Gain	2^{-11}	2^{-12}	2^{-13}	2^{-14}
Uncompensated Angle Error [μrad]	16	17	16	17
Residual Angle Error [μrad]	7	7	8	11

Table 7.2: Tracking error comparison in the presence of atmospheric angle of arrival error

7.6 Link point-ahead performance

The performance of the point-ahead interaction between the tracking system and the pointing system was tested *in situ* on the 16 km link. The goal of this test was to demonstrate the pointing mirror controller response to the tracking mirror motion. The pointing mirror response to tracking error maintains the pointing of the link in the presence of common-mode pointing and tracking disturbances. Unfortunately, the point-ahead functionality could only be demonstrated with a static link pointing error. A dynamic test of the point-ahead interaction would require a controlled dynamic disturbance of the entire terminal. Due to the large mass of the terminal, a controlled common mode disturbance was not feasible. The point-ahead performance was therefore only validated by its ability to correct a static pointing error. This test provided data similar to a step response.

For the point-ahead testing, the terminal was pointed out of alignment by a small angle equal to approximately $\frac{1}{2}$ the transmitter divergence. This pointing error placed the terminal pointing at the edge of transmitter divergence. The point-ahead system was then be able to bring the link back to a centered alignment based on the receiver angle of arrival angle. When activated, the tracking system moved the tracking FSM to correct the receiver angle of arrival error. The tracking FSM motion,

reported by the tracking FSM position sensor, was fed forward to the pointing FSM controller system. The pointing FSM controller then brought the angle of departure of the transmitter to equal the angle of arrival of the receiver. Thus, the pointing error of the terminal was corrected.

The point-ahead performance was tested for various interaction filter bandwidths. The interaction filter was a low-pass filter that filters the tracking FSM position signal that was fed into the pointing mirror controller. This filter eliminated high frequency noise that would have been fed to the pointing system and limited any high frequency disturbances. The point-ahead was tested with the loop filter set to 3000 Hz, 300 Hz, and 30 Hz. The point-ahead system was unstable for filter bandwidths above 30 Hz. The instability seemed to be due to a lack of correlation between the angle of arrival error and the angle of departure error due to the differing atmospheric optical path differences [83][84]. The dynamic difference between the angle of arrival and angle of departure errors may be a fundamental limit on the performance of bi-static pointing and tracking optical terminals. Future research will include techniques to extend the high frequency capability of the pointing system. These techniques include accelerometer assisted tracking [85], pointing nutation [86], pointing optimization [87], and disturbance canceling base mounts [42].

The point-ahead system was able to correct the low frequency disturbances including the static point error introduced to test the point-ahead system. The action of the point-ahead system is shown in Figure 7.21. Plotted in Figure 7.21a is the tracking FSM internal position sensor output response at the activation of the pointing and tracking. Plotted in Figure 7.21b is the corresponding pointing FSM internal

position sensor response. The synchronization between the two mirrors can easily be seen. An unfortunate choice of oscilloscope settings resulted in a low quality measurement of the tracking mirror position signal.

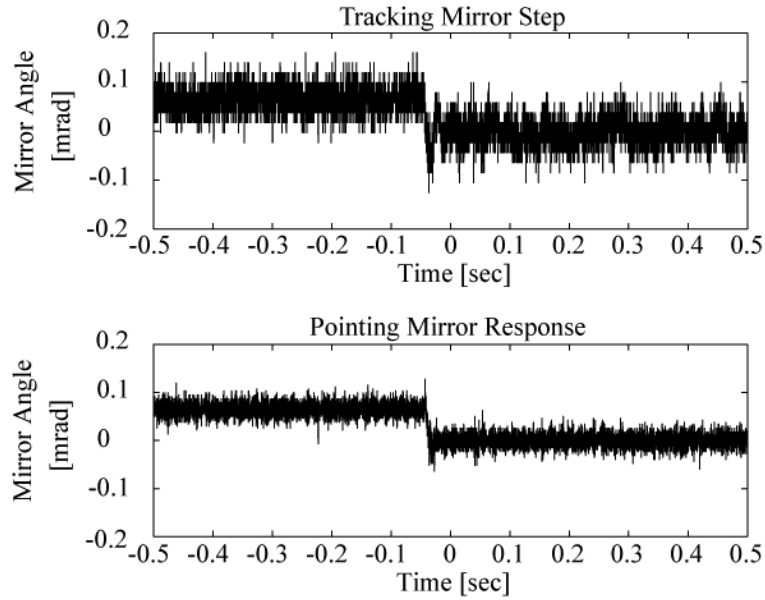


Figure 7.21: Point-ahead system response to a static pointing error

Chapter 8 Atmospheric effects

The performance of the communications channel of the FSO link was dominated by atmospheric effects. The two main atmospheric issues effecting the link were visibility and scintillation. For the communications link to perform well, the visibility had to be high enough that the link margin exceeded the scintillation induced signal fading. The weather conditions required for optimal link performance were good visibility and low scintillation. These days occurred on mild days when the sky was clear and the temperatures of the water and the air were similar.

8.1 Weather

The weather was a critical component for the link performance. Link performance was dominated by the visibility and scintillation conditions of the atmosphere. The weather was monitored during link testing in a number of ways. One main source of weather data was the National Weather Service METAR weather data collection sites. METAR weather stations are typically operated at airports, and take a specific set of hourly weather measurements. These measurements include temperature, humidity, visibility, and precipitation. Data from four METAR weather sites was examined to find weather data representative of the weather conditions on the optical link. The locations of these four METAR sites are illustrated in Figure 8.1.

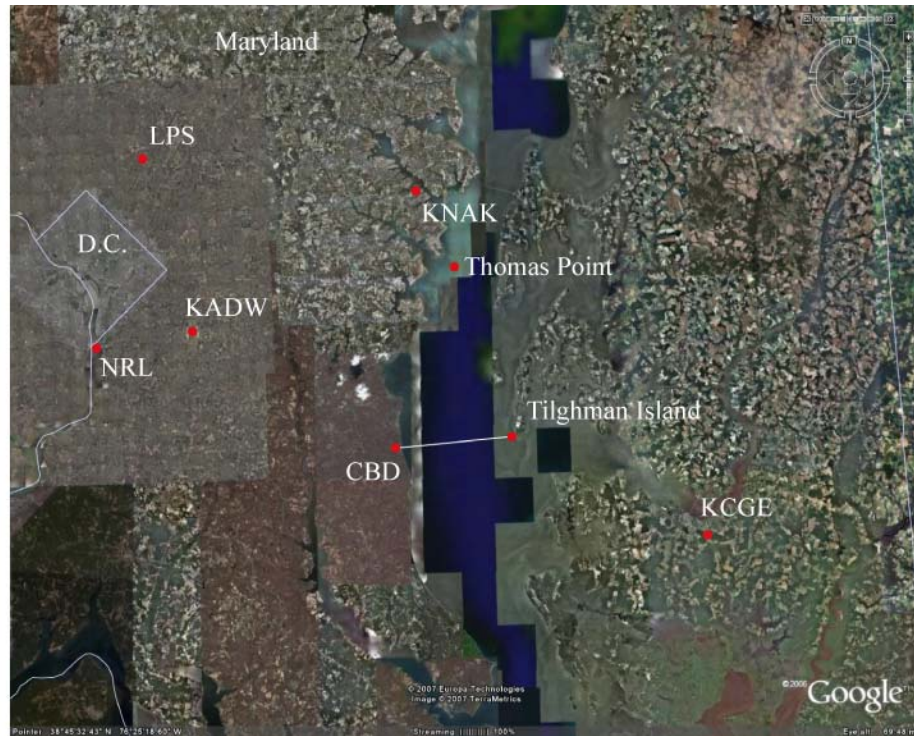


Figure 8.1: METAR weather station locations

The four weather sites were KADW, KCGE, KNAK and the Thomas Point Buoy. The designations KADW, KCGE, and KNAK stand for Andrews Air Force Base, Annapolis Naval Academy, and the Cambridge-Dorchester Airport. The Thomas Point Buoy is a marine weather station that provides weather data to the NWS but does not conform to the METAR data standard. However, Thomas Point does provide data for the water temperature that is not available from the airport data. The water temperature relative to the air temperature is an important factor in atmospheric scintillation. Listed in Table 8.1 is an example METAR weather data set from KNAK on 10/18/2006.

TimeEDT	Temperature [F]	Dew Point [F]	Humidity [%]	Pressure [mm]	Visibility [miles]	Wind Direction	Wind Speed [MPH]	Gust Speed [MPH]	Precipitation [In]	Conditions
12:54 AM	64	62	93	29.84	7	South	5.8	-	N/A	Overcast
1:54 AM	64	62	93	29.82	6	South	3.5	-	N/A	Overcast
2:54 AM	64	62	93	29.82	5	South	4.6	-	N/A	Overcast
3:54 AM	64	62	93	29.81	4	Calm	Calm	-	N/A	Overcast
4:17 AM	64.4	63	94	29.81	4	Calm	Calm	-	N/A	Overcast
4:41 AM	64.4	63	94	29.81	3	Calm	Calm	-	N/A	Overcast
4:54 AM	63	62	97	29.82	4	Calm	Calm	-	N/A	Overcast
5:46 AM	62.6	63	##	29.82	2.5	Calm	Calm	-	N/A	Overcast
5:54 AM	63	62	97	29.83	2.5	Calm	Calm	-	N/A	Overcast
6:08 AM	62.6	63	##	29.82	3	Calm	Calm	-	N/A	Overcast
6:18 AM	62.6	63	##	29.82	2.5	Calm	Calm	-	N/A	Overcast
6:29 AM	64.4	63	94	29.83	3	Calm	Calm	-	N/A	Overcast
6:54 AM	64	62	93	29.84	3	Calm	Calm	-	N/A	Overcast
7:08 AM	62.6	63	##	29.84	2.5	Calm	Calm	-	N/A	Overcast
7:16 AM	64.4	63	94	29.84	4	Calm	Calm	-	N/A	Overcast
7:54 AM	64	62	93	29.86	3	Calm	Calm	-	N/A	Overcast
8:11 AM	64.4	63	94	29.86	4	Calm	Calm	-	N/A	Overcast
8:54 AM	64.9	62	90	29.88	4	Calm	Calm	-	N/A	Overcast
9:21 AM	66.2	61	83	29.88	9	NW	4.6	-	N/A	Mostly Cloudy
9:54 AM	66	61	84	29.89	10	West	4.6	-	N/A	Overcast
10:54 AM	66	61	84	29.89	10	North	4.6	-	N/A	Overcast
11:14 AM	66.2	61	83	29.89	10	NNW	5.8	-	N/A	Scattered Clouds
11:54 AM	68	61	78	29.89	10	NNW	3.5	-	N/A	Partly Cloudy
12:54 PM	69.1	62	78	29.89	9	SE	5.8	-	N/A	Partly Cloudy
1:06 PM	68	63	83	29.87	7	SE	6.9	-	N/A	Mostly Cloudy
1:15 PM	69.8	63	78	29.87	6	SE	8.1	-	N/A	Scattered Clouds
1:54 PM	66.9	62	84	29.87	7	SE	6.9	-	N/A	Mostly Cloudy
2:12 PM	69.8	63	78	29.85	7	SE	5.8	-	N/A	Scattered Clouds
2:54 PM	68	63	84	29.86	7	SE	8.1	-	N/A	Clear
3:54 PM	68	62	81	29.85	8	SE	6.9	-	N/A	Clear
4:54 PM	68	62	81	29.85	8	SE	4.6	-	N/A	Clear
5:54 PM	68	61	78	29.86	8	SSE	5.8	-	N/A	Partly Cloudy
6:54 PM	66	62	87	29.86	7	Calm	Calm	-	N/A	Clear
7:54 PM	64	62	93	29.88	5	Calm	Calm	-	N/A	Mostly Cloudy
8:54 PM	64	62	93	29.88	4	Calm	Calm	-	N/A	Scattered Clouds
9:54 PM	63	62	97	29.88	3	Calm	Calm	-	N/A	Mostly Cloudy
10:54 PM	64.9	62	90	29.9	6	Calm	Calm	-	N/A	Overcast
11:54 PM	63	60	90	29.89	5	Calm	Calm	-	N/A	Scattered Clouds
<!-- 0.236:1 -->										

Table 8.1: Example METAR data from KNAK (Naval Academy) weather station

In addition to the NWS data, weather station data was collected at both ends of the link. This weather station data provided local air temperature and wind speed data for both ends of the optical link. All the sources of weather data were compiled along with the optical link performance statistics.

In order to reduce the quantity of data presented, only the most relevant weather data will be used for comparisons with link performance. For example, the visibility data is only presented for the KNAK observations. This was done because KNAK is the only weather station located near the water. Being near the water, KNAK had similar visibility conditions to the optical link over the water. The NADW visibility was taken 20 miles inland and was not well correlated to the link visibility. Further, many of the weather observations were redundant. There was generally agreement between the air temperature measurements of the CBD weather station, the Tilghman Island weather station, and the Thomas Point weather station. Since the air-water temperature difference seemed to be a factor in the scintillation conditions, only the Thomas Point temperature data are presented.

8.2 Atmospheric effects measurements

The atmospheric effects on the FSO link were measured on 8 days during the link testing. The atmospheric effects were measured by measuring the optical power coupled into the receiver 100 μm core multi-mode optical fiber (MMF). The received optical power was measured using a Thorlabs PDA400 InGaAs photodetector. The received signal from this detector was recorded with a Tektronix TDS5054B Oscilloscope and a NI 6036E DAQ card. The recoded signals were analyzed to

determine the mean receive optical power as well as the received signal variance. The received signal variance was quantified using the scintillation index and the log (base 10) variance. Scintillation index, σ_I^2 , is a standard scintillation metric which is calculated from the received optical power, I , by equation (8.1). The scintillation index is the normalized variance of the received optical power. The standard scintillation index measurements employ point receivers.[24] The results presented here are for an 8 inch receiver with a 150 μ rad field of view. For the remainder of this document any reference to measured scintillation index refers to the normalized variance of the received power through the 8 inch aperture with a 150 μ rad field of view.

$$\sigma_I^2 = \frac{\sigma^2(I)}{\langle I \rangle^2} \quad (8.1)$$

The log variance of received optical power is calculated as the variance of the normalized received optical power as in equation (8.2). The log standard deviation derived from this variance has units of dB. As such, the log standard deviation is a useful link design parameter because it allows quick link margin calculations. When determining the necessary clear air link margin, it is first necessary to specify the allowable scintillation fading rate. The scintillation fading statistics can be assumed to be log normal in distribution. It may then be specified that 3 sigma fading occurrences are tolerable. This would be equivalent to specifying the allowable probability of signal loss due to scintillation to be less than 1%. The required link

margin to achieve this level of performance would be 3 times the log standard deviation of the scintillation on the FSO link.

$$\sigma_{\log(I)}^2 = \text{var}\left(10\log_{10}\left(\frac{I}{\langle I \rangle}\right)\right) \quad (8.2)$$

The measurements of the atmospheric effects on the FSO link are tabulated in Table 8.2. This table includes the data and time of each link measurement. Each measurement has three atmospheric effect values. The reported atmospheric effects were the scintillation index, the log standard deviation, and the mean received optical power. Listed along with these link effects are some relevant weather measurements. These weather measurements include the visibility at KNAK, the wind speed at Thomas Point, as well as the air and water temperature difference at Thomas Point. These weather measurements seemed to be the most correlated to the link measurements of all the weather data collected. The measurements in Table 8.2 are enumerated for referencing in the following sections. Table 8.2 should be referenced whenever dataset numbers are used in subsequent charts.

Data Set Number	Date	Hour	Scintillation Index	Signal Variance [dB]	Signal Mean Value [nW]	TP Air Temperature [Deg.]	TP Water Temperature [Deg.]	TP Windspeed [mph]	Naval Academy Visibility [miles]
1	9/22	9 AM	1.48	3.58	56	64	71	12.7	10
2	9/22	9 AM	1.36	3.48	49	64	71	12.7	10
3	9/22	10 AM	1.15	3.05	33	64	71	12.7	10
4	9/22	10 AM	1.71	2.9	28	64	71	12.7	10
5	9/25	12 PM	0.89	3.66	11	70	71	11.5	10
6	9/25	12 PM	0.95	3.73	11	70	71	11.5	10
7	9/25	3 PM	0.23	3.04	26	72	72	12.7	10
8	9/25	3 PM	0.29	3.14	23	72	72	12.7	10
9	9/25	3 PM	0.32	2.27	24	72	72	12.7	10
10	9/25	3 PM	0.42	3.04	19	72	72	12.7	10
11	9/25	3 PM	0.5	3.14	19	72	72	12.7	10
12	10/4	12 PM	0.73	3.89	31	70	70	8.1	7
13	10/4	12 PM	1.34	5.43	10	70	70	8.1	7
14	10/4	12 PM	1.56	4.51	6	70	70	8.1	7
15	10/4	12 PM	0.63	3.47	30	70	70	8.1	7
16	10/4	12 PM	0.84	3.95	25	70	70	8.1	7
17	10/4	12 PM	1.3	4.41	12	70	70	8.1	7
18	10/4	12 PM	2.01	5.9	15	70	70	8.1	7
19	10/11	12 PM	0.68	4.29	5	66	67	4.6	5
20	10/11	12 PM	0.59	4.81	5	66	67	4.6	5
21	10/11	12 PM	0.51	4.23	7	66	67	4.6	5
22	10/18	12 PM	0.32	2.91	79	66	64	5.8	9
23	10/18	12 PM	0.56	3.87	60	66	64	5.8	9
24	10/18	12 PM	0.55	3.86	46	66	64	5.8	9
25	10/18	2 PM	0.53	3.07	19	66	63	6.9	7
26	10/18	2 PM	0.48	2.87	21	66	63	6.9	7
27	10/18	2 PM	0.62	3.22	14	66	63	6.9	7
28	10/25	3 PM	2.17	6.42	4	53	59	23	10
29	10/25	3 PM	1.67	5.45	7	53	59	23	10
30	10/25	3 PM	1.64	5.49	6	53	59	23	10
31	11/17	1 PM	0.43	2.71	134	58	56	13.8	10
32	11/17	1 PM	0.38	2.57	124	58	56	13.8	10
33	11/17	1 PM	0.37	2.51	143	58	56	13.8	10
34	11/17	1 PM	0.32	5.47	157	58	56	13.8	10
35	11/27	3 PM	1.79	4.9	47	52	54	4.6	10
36	11/27	3 PM	1.98	4.89	52	52	54	4.6	10
37	11/27	3 PM	2.18	4.85	56	52	54	4.6	10
38	11/27	3 PM	1.65	4.7	51	52	54	4.6	10

Table 8.2: FSO link atmospheric effects data summary

8.3 Atmospheric attenuation

The dominant weather factor in link performance is the link attenuation due to reduced visibility. Listed in Table 8.2 are the visibility measurements reported at the KNAK weather station as well as the link throughput. Illustrated in Figure 8.2 is the mean received optical power along with the KNAK visibility measurements for comparison. The sensitivity of the communications detector was 2nW and the link performed well when the average received power was above 40nW.

It can be seen in Figure 8.2 that the received power is lower when the visibility is reduced. On 10/11/2006, there were fog conditions throughout the area that adversely effected the link. The effect of the fog can be seen in the received power and visibility data.

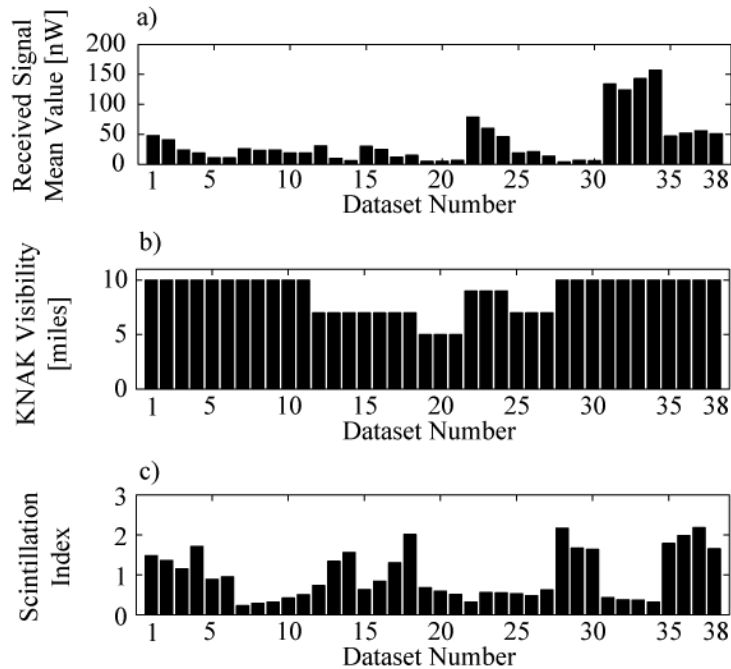


Figure 8.2: FSO link atmospheric measurements
a) Received optical power, b) KNAK visibility, and c) Scintillation Index

It can be seen in Figure 8.2 that the received power can be reduced even when the visibility is high. This is due to two effects. First, visibility measurements are not reported over 10 miles. Any variability in the visibility above 10 miles is lost. The second effect influencing the mean received optical power is the scintillation index. The scintillation index is also plotted in Figure 8.2. A high scintillation index may also contribute to a reduced received optical power. This is due to the limited field of view of the receiver optical fiber. Scintillation can reduce the fiber coupling efficiency and cause beam wander loss. The atmospheric measurements were performed with tracking off so as not to complicate the data interpretation. It should be noted that the maximum received power occurred when visibility was high and the scintillation was low.

8.4 Scintillation statistics

Scintillation is the second major atmospheric factor effecting link performance. Scintillation causes large dynamic signal variations. The FSO link needs a link margin large enough to allow for the scintillation variation while maintaining the FSO link. Plotted in Figure 8.3 are the scintillation index values for the recorded data sets. The data in Figure 8.3 suggests that when the wind speed is high and the air-water temperature difference is high, the scintillation index will be high. Neither the air-water temperature difference or the average wind speed data alone can predict the scintillation conditions.

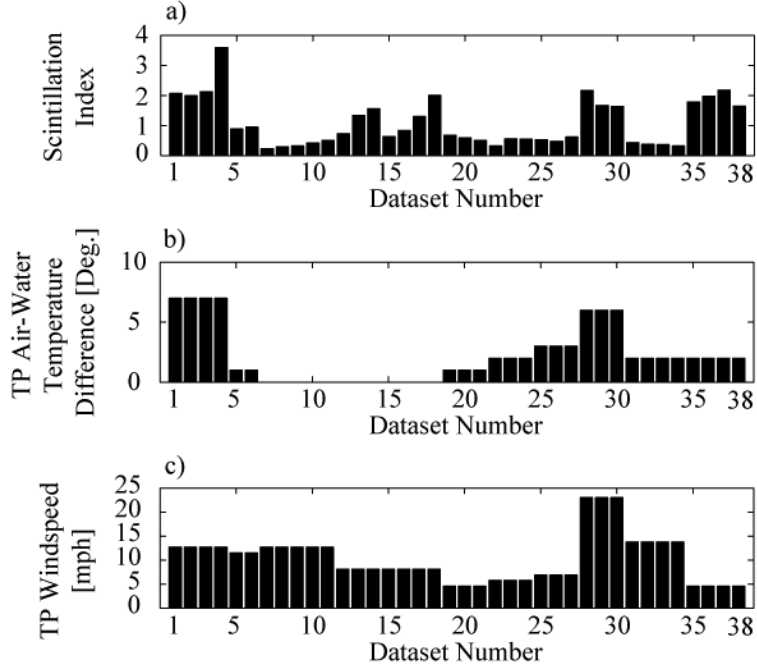


Figure 8.3: Scintillation index and Thomas Point weather buoy data
a) Scintillation index, b) Air-water temperature difference, and c) Wind speed

Data sets 1-4 and 28-30 in Table 8.2 suggest a relationship between scintillation and the Thomas Point weather data. However, data sets 35-39 show a high scintillation index despite low air-water temperature difference and low wind speed. This data demonstrates that scintillation is a random process that depends on a great number of environmental variables. Prediction of scintillation from a few simple metrics is difficult, if not impossible. The intention of this section was to demonstrate that some relation exists between the weather conditions and the scintillation. Indeed this relation exists, but it is sufficiently complicated to make scintillation performance prediction difficult if not impossible.

An important observation from the scintillation data is the magnitude and variability of the scintillation index. The scintillation index is typically between 0.2

and 2.0. The scintillation index can be as high as 3.6. In terms of log variance, the log standard deviation is typically between 2.5 dB and 3.7 dB. The log standard deviation may be as high as 5.5 dB. A rule of thumb for FSO link margin is that a good FSO link margin is 5 times the log standard deviation. Therefore a link with about 15 dB of margin would operate acceptably under these scintillation conditions. This was the case with the 16 km FSO link which had a link margin of 13 dB.

In addition to the magnitude, the speed of the scintillation is also an important factor. The speed of the scintillation impacts receiver AGC specifications and is a typical parameter reported on scintillation statistics. The power spectral density for three representative sets of scintillation data were calculated. These PSDs are presented in Figure 8.4. The three data sets were data sets, 7, 31, and 28. These data sets had scintillation index values of 0.23, 0.43, and 2.17 respectively. These data sets are representative of weak, moderate, and strong atmospheric turbulence. The stronger turbulence has greater high frequency content than weak and mild turbulence. Also plotted, in Figure 8.4, are the respective cumulative PSD plots for the three data sets. The cumulative PSD curves allow the determination of the frequency below which 90% of the power is contained. For the three data sets, 7, 31, and 28, the 90% cumulative power frequencies were 30 Hz, 60 Hz, and 200 Hz, respectively. Weak to moderate turbulence has frequency content below 100 Hz and strong turbulence may have frequency content of a few hundred Hz. It also seems that the relation between scintillation index and the 90% cumulative power frequency is somewhat linear.

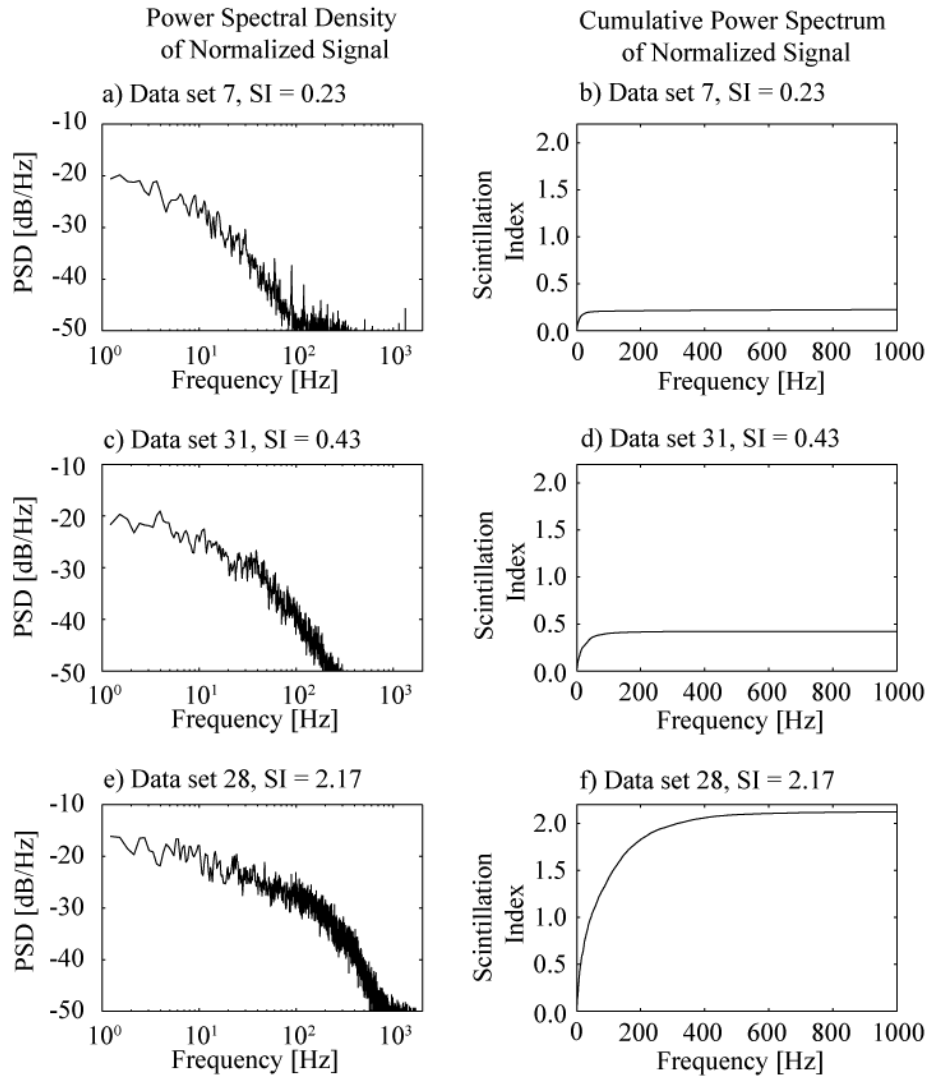


Figure 8.4: Scintillation power spectral density curves for various scintillation index values
a) $\sigma_I^2 = 0.23$, b) $\sigma_I^2 = 0.43$, and c) $\sigma_I^2 = 2.17$

8.5 Spatial diversity

The 3 retro-reflector array provided more than just a three-fold benefit in link power. The three retro-reflector array provided improved atmospheric scintillation performance over a single retro-reflector. The array of retro-reflectors utilized spatial diversity due to the multiple atmospheric paths traversed by the light from the three separate retro-reflectors. The retro-reflectors were arranged in a spacing greater than the expected atmospheric coherence length. The different optical paths should have unrelated turbulence effects. The array performed as an extended coherent source. This offers better scintillation performance over a single coherent point source. The improvement should not be expected to be as great as an array of incoherent sources. However, it still offered some improvement in scintillation index.

The spatial diversity effect of the array on the scintillation index was measured on four days during the link testing. The spatial diversity data is listed in Table 8.2. It can be seen in Table 8.2 that for all 4 days of testing, the scintillation index was reduced by the use of multiple array elements. This reduction appears to be approximately linear. The data taken on 11/27/2006 includes the scintillation index measured using a 3 inch retro-reflector target as opposed to the array of MMRs. This was done to provide a control test for the data. It could be presumed that the reduction in scintillation index was due to the increase in received optical power that comes from adding elements to the array. However, the 3 inch retro-reflector, which returned significantly more optical power than the array, had a scintillation index similar to a single MRR data. This indicates the extended source nature of the array was indeed the cause of the reduction in scintillation index.

Date	Exposed Array Elements	Scintillation Index	Log Received Power Standard Deviation [dB]	Mean Received Power [nW]
10/18	1	1.38	5.2	6
10/18	2	0.78	4.4	7
10/18	3	0.48	3.5	19
10/25	1	5.27	5.2	1
10/25	2	2.96	5.1	3
10/25	3	1.92	5.0	6
11/17	1	1.70	5.6	44
11/17	2	0.88	3.9	85
11/17	3	0.39	2.6	134
11/27	1	5.64	6.7	15
11/27	2	2.74	5.6	35
11/27	3	1.99	4.9	51
11/17	3 inch retro	1.44	5.8	1109

Table 8.3: Scintillation index and received optical power for 1 to 3 array elements measured on 4 separate days

The probability distributions functions (PDFs) for the received optical power measurements taken on 11/17/2006 are plotted in Figure 8.5. These PDFs are the probability distribution functions of the log (base 10) of the normalized received optical power so the units are decibels. The Gaussian distributions in Figure 8.5 are indicative of the underlying log normal received power PDF. In Figure 8.5, the log standard deviation of the signal is reduced as the number of array elements is increased. The time domain data, from which the PDFs in Figure 8.5 were derived, is also plotted in Figure 8.5.

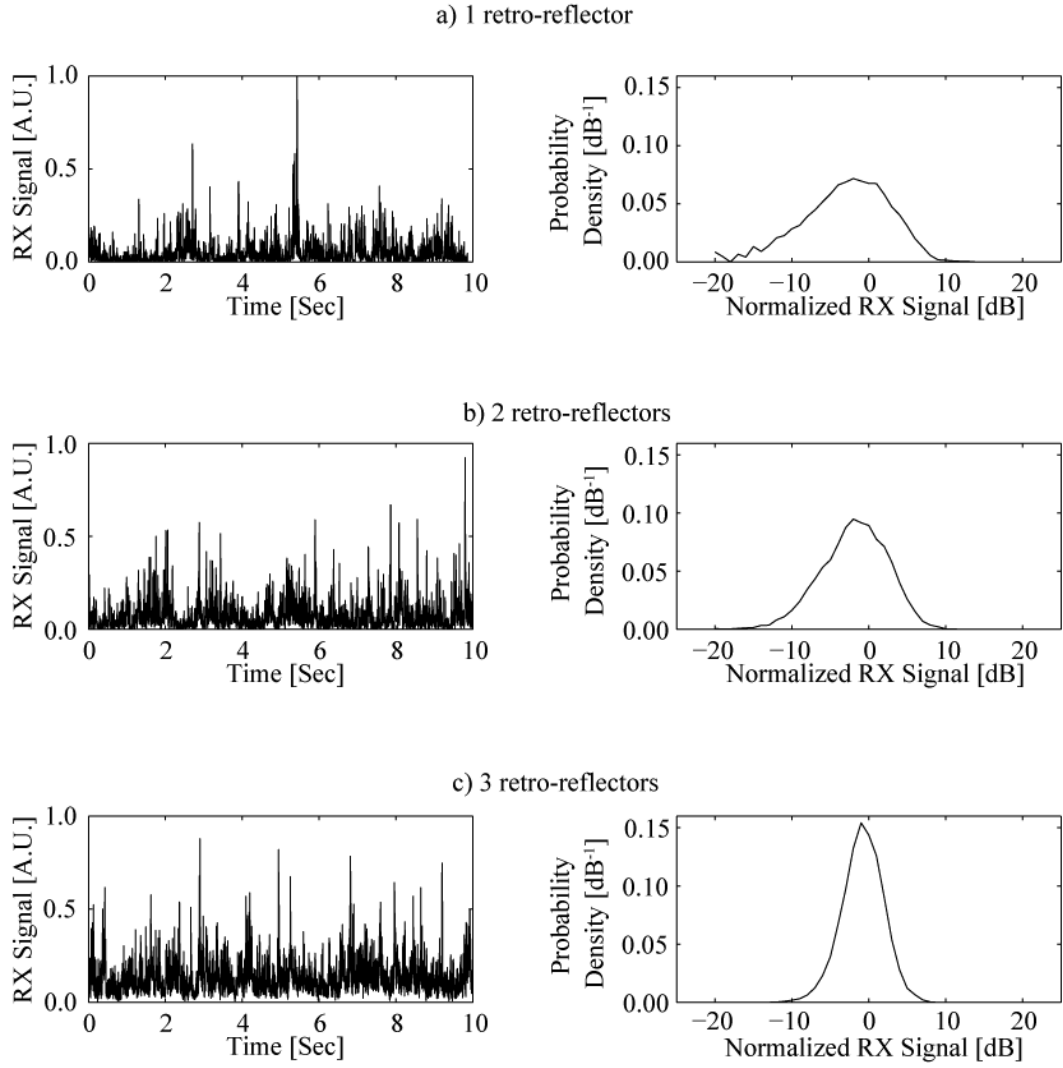


Figure 8.5: Received optical signal for various MRR array element counts
a) 1 retro-reflector, b) 2 retro-reflectors, and c) 3 retro-reflectors

8.6 Angle of arrival variance

Atmospheric turbulence can cause an angle of arrival error to the receiver in addition to total power fluctuations. The angle of arrival error can cause the focused return spot to move off the receiver optical fiber resulting in a loss of signal. This error may cause an additional dynamic loss in the system. The quadrant detector in

the receiver tracking system was used to measure the angle of arrival variance. Listed in Table 8.4 is the angle arrival variance for the five days the angle of arrival was measured. Also listed in Table 8.4 is the scintillation index and weather measurements taken on those days.

Dataset Number	Date	Time	Azimuth Angle of Arrival Standard Deviation [urad]	Elevation Angle of Arrival Standard Deviation [urad]	Radial Angle of Arrival Standard Deviation [urad]	TP Air Temperature [Deg.]	TP Water Temperature [Deg.]	TP Windspeed [mph]	Naval Academy Visibility [miles]
1	9/29	2 PM	25	24	35	57	71	15	10
2	9/29	2 PM	23	22	32	57	71	15	10
3	9/29	2 PM	24	24	34	57	71	15	10
4	9/29	2 PM	27	24	36	57	71	15	10
5	10/4	4 PM	15	14	21	73	71	13	8
6	10/4	4 PM	9	22	24	73	71	13	8
7	10/4	4 PM	7	7	10	73	71	13	8
8	10/4	4 PM	15	12	19	73	71	13	8
9	10/4	4 PM	13	10	16	73	71	13	8
10	10/18	2 PM	23	24	33	66	64	6	7
11	10/18	2 PM	18	18	25	66	64	6	7
12	10/18	2 PM	29	30	42	66	64	6	7
13	10/18	2 PM	17	21	27	66	64	6	7
14	10/18	2 PM	18	18	25	66	64	6	7
15	10/18	2 PM	14	17	22	66	64	6	7
16	10/18	2 PM	19	27	33	66	64	6	7
17	10/18	2 PM	20	20	28	66	64	6	7
18	10/18	2 PM	14	22	26	66	64	6	7
19	11/17	9 AM	11	22	25	52	56	7	10
20	11/27	10 AM	16	27	31	49	50	9	8
21	11/27	11 AM	17	27	32	49	50	9	8
22	11/27	11 AM	16	22	27	49	50	9	8
23	11/27	11 AM	17	22	28	49	50	9	8

Table 8.4: Angle of arrival data statistics

Plotted in Figure 8.6 is the angle of arrival error along side the Thomas Point Buoy air-water temperature difference and wind speed. The relationship between these variables is weaker than the relation seen for the scintillation index. It seems that the angle of arrival error may be increased when the air-water temperature difference and wind speed are high. However, this connection appears only vaguely in the data. The relation between gross weather data and the scintillation index may be stronger because scintillation index is a parameter that is effected by conditions all along the length of the beam propagation.

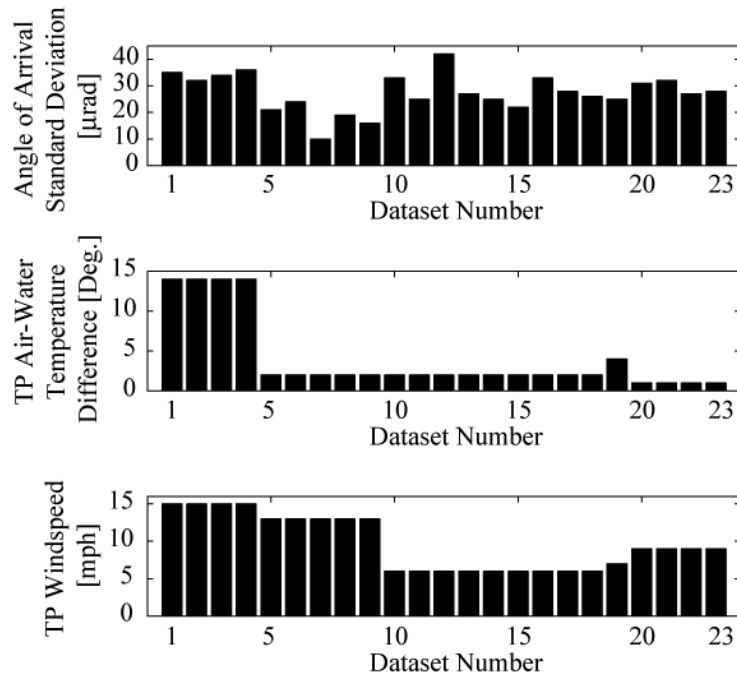


Figure 8.6: Angle of arrival error summary with air-water temperature differential and wind speed as recorded at the Thomas Point weather station

The angle of arrival error may be more strongly effected by localized effects near the receiver aperture. The angle of arrival error is the first order phase error of the received beam. This phase error would have to be generated near to the terminal.

First order phase error generated early in beam propagation would propagate out of the beam prior to reaching the terminal. The localized effects that may influence the angle of arrival may include the air-ground temperature difference at CBD or the wind speed at CBD. Similar to the case for scintillation, there are a large number of variables that may effect the angle of arrival error. Although weather conditions are a poor predictor of angle of arrival error, certain bounds on the angle of arrival error can be determined from the data. The angle of arrival error observed was between 7 μrad and 30 μrad in standard deviation.

The angle of arrival error can be compensated by the tracking system provided the spectral content of the angle of arrival error is below the closed loop tracking bandwidth of the tracking system. Plotted in Figure 8.7 is the PSD of a typical angle of arrival data set taken on 11/17/2006. From the cumulative (integrated) power spectrum we can determine the frequency below which 90% of the power is contained. The 90% cumulative power frequency for the angle of arrival error was typically 50 Hz. The 90% cumulative power frequency could be as high as 150 Hz.

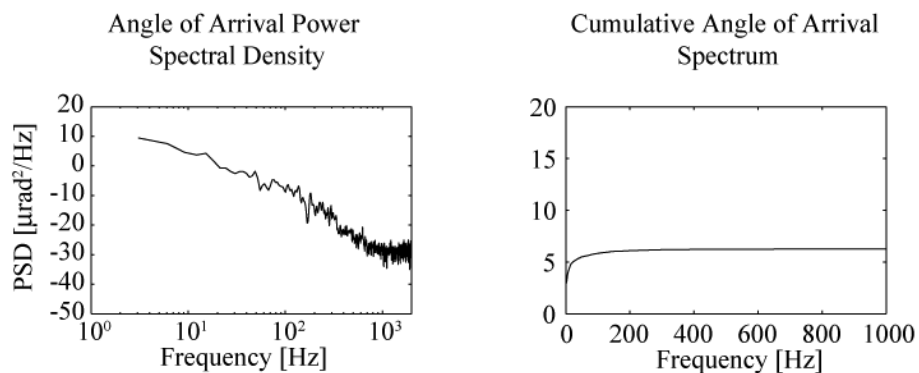


Figure 8.7: Angle of arrival error power spectral density and cumulative power spectral density

Chapter 9 Communications channel performance

Primarily, the data sent across the FSO link was compressed video from a CCD camcorder. The compression hardware enabled three levels of video quality, low, medium, and high. Lower quality video fills the communications channel with relatively smaller data packets. High quality video, however, used a much larger packet size. The low quality video was more tolerant of high scintillation of the data link as shorter packets could get across the link between signal fades. Shown in Figure 9.1 is the AC coupled output of the PINFET photoreceiver during packet transmission. The sharp transitions in the signal are the edges of the data packets. The slow amplitude modulation of the data is the effect of atmospheric scintillation induced fading.

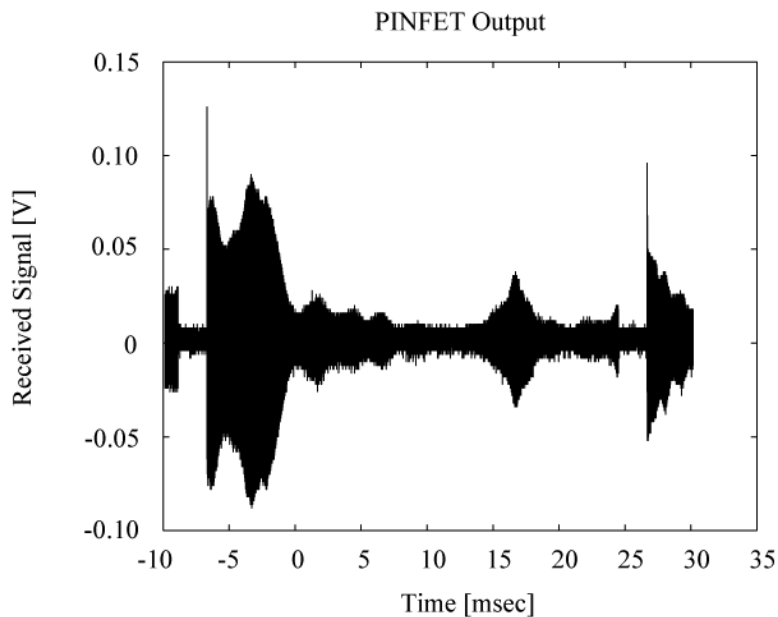
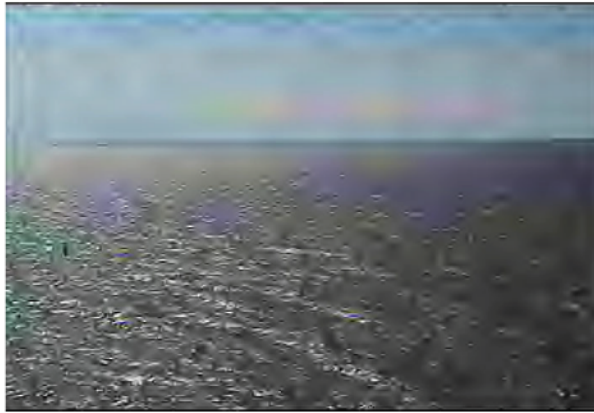


Figure 9.1: PINFET receiver photodiode sample output

Pictured in Figure 9.2a is the first frame sent across the FSO link. This was a low quality video frame. The low quality video could be supported with as little as 10nW of received optical power. However, 10nW provided only 7 dB of link margin. Such little link margin greatly limited the frequency of frames successfully crossing the link. The first video frames came across the link at an intermittent rate. Approximately one frame every few minutes successfully crossed the link. Fortunately, improvements in the optical alignment as well as improved atmospheric conditions on subsequent days lead to several days of testing with uninterrupted frame transfers. Pictured in Figure 9.2b is a frame from a medium quality video transmission. Pictured in Figure 9.2c is a frame from a high quality video transmission. The images in these frames are of the Tilghman Island shoreline. The high quality images have much better resolution than the lower quality images. The robust nature of the communication channel was demonstrated by the capability to send lower quality images when the link was suffering severe turbulence conditions.

a)



b)



c)

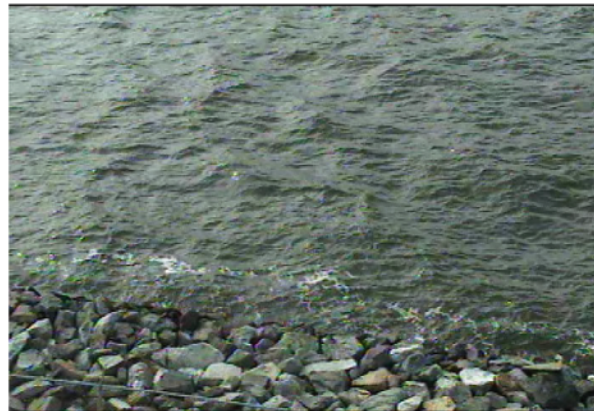


Figure 9.2: Video link frames transferred across the 16 km MRR FSO link over the Chesapeake Bay
a) low quality, b) medium quality, c) high quality

9.1 Video link performance with redundant transmission

To avoid lost frames, prerecorded video frames can be transmitted multiple times. This transmission approach did not incorporate acknowledgment of packet reception. It simply sent each frame a fixed number of times before moving onto the next frame. The degree of redundancy was selected based on the prevailing scintillation conditions. Pictured in Figure 9.3 is an image from the prerecorded video that was transmitted across the FSO link using redundant frames. The finger counting seen in these frames proceeded smoothly when transmitted across the FSO link despite the scintillation induced channel fading. Using redundant frame transmission, the channel fading merely resulted in a reduced frame rate. The live video lost resolution during high fading while prerecorded video lost only frame rate.

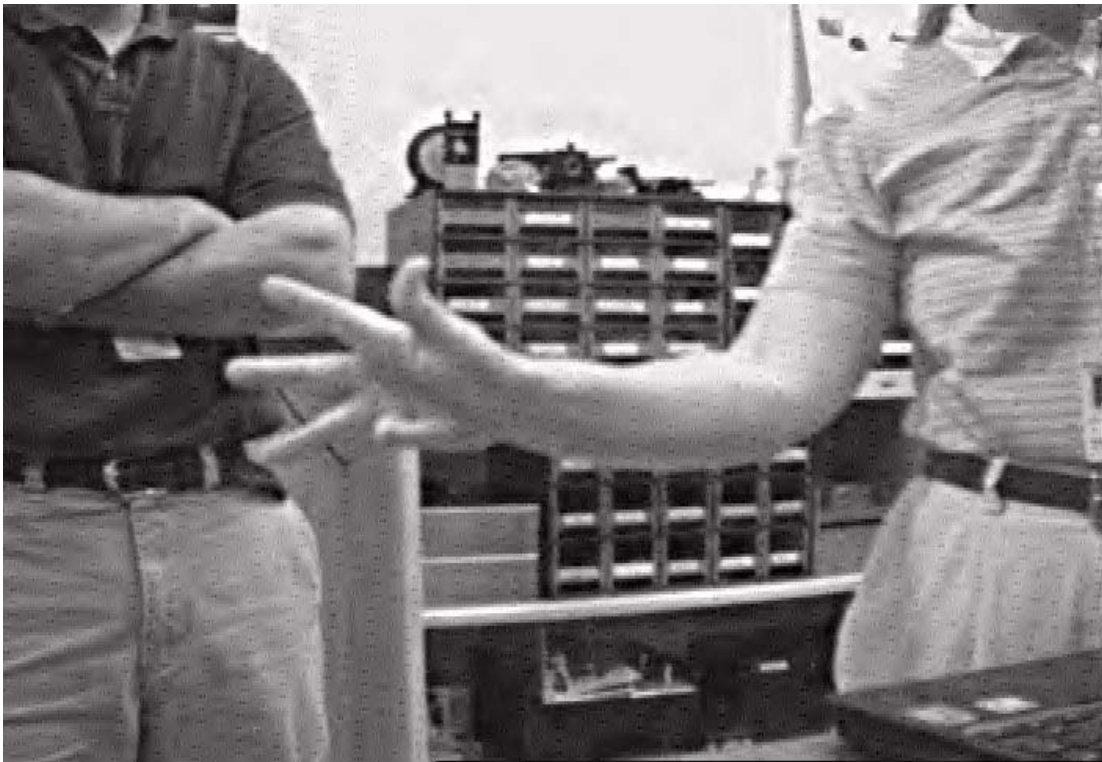


Figure 9.3: Prerecorded video frame transmitted over FSO link with frame redundancy

9.2 Half-duplex data link performance

When the photodetector was enabled on the MRR array, bi-direction data transfer was possible. The bidirectional link was a duplex Ethernet link running at 2 Mbps. The data compression electronics on both sides of the link provided the translation of the 2 Mbps link data to 100 BASE-T Ethernet for connection to laptop computers. To test the throughput of the data link, a file transfer program was used which provided transfer statistics as the designated file was transferred across the link. The packet size could be configured to optimize data throughput across the fading communications channel. Smaller packet transmissions performed better in strong scintillation conditions because they get across the link between the scintillation fades. Longer packets incur errors and required retransmission. Longer packets performed better in weak scintillation as more data was transferred with less overhead.

The half-duplex data transfer was tested on three days; 9/25/2006, 9/29/2006, and 10/18/2006. Listed in Table 9.1 is a summary of the data transfer statistics for the three days of testing. During data transfer testing, the packet size and direction of transfer was varied. Multiple data transfers were completed for each packet size and data direction. The results presented in Table 9.1 are averages over all data sets with similar testing scenarios.

Scenario Number	Date	Packet Size [Bytes]	Transfer Direction	Scintillation Index	Mean Received Power [nW]	Throughput [kbps]
1	9/25	512	Upload	0.35	22	186
2	9/25	1024	Upload	0.35	22	223
3	9/25	2048	Upload	0.35	22	418
4	9/25	4096	Upload	0.35	22	406
5	9/25	8192	Upload	0.35	22	470
6	9/25	512	Download	0.35	22	326
7	9/25	1024	Download	0.35	22	395
8	9/25	2048	Download	0.35	22	386
9	9/25	4096	Download	0.35	22	404
10	9/25	8192	Download	0.35	22	326
11	9/29	512	Upload	1.89	65	13
12	9/29	1024	Upload	1.89	65	16
13	9/29	2048	Upload	1.89	65	19
14	9/29	4096	Upload	1.89	65	14
15	9/29	8192	Upload	1.89	65	3
16	10/25	512	Download	0.48	62	631
17	10/25	1024	Download	0.48	62	778
18	10/25	2048	Download	0.48	62	991
19	10/25	4096	Download	0.48	62	1289
20	10/25	8192	Download	0.48	62	838
21	10/25	512	Upload	0.48	62	225
22	10/25	1024	Upload	0.48	62	291
23	10/25	2048	Upload	0.48	62	347
24	10/25	4096	Upload	0.48	62	535
25	10/25	8192	Upload	0.48	62	502
26	10/25	512	Download	0.48	31	84
27	10/25	1024	Download	0.48	31	64
28	10/25	2048	Download	0.48	31	50
29	10/25	4096	Download	0.48	31	42
30	10/25	8192	Download	0.48	31	0

Table 9.1: Bidirectional link performance statistics

The results in Table 9.1 are plotted in Figure 9.4. This graphical representation makes it easier to pick out trends in the data. When the scintillation index was high (scenarios 10-15), the throughput was low for all packet sizes. Very little data gets through, regardless of packet size, when the link suffers severe fading. It can also be seen that when the received power was high and the scintillation was low (scenarios 16-25), the throughput was the highest. Data scenarios (16-25) also show that data throughput was greater on downloads to Tilghman Island than on uploads from Tilghman Island. This was due to the much larger received optical power at Tilghman Island. The link to Tilghman Island had higher link margin (24 dB) than the link margin back from Tilghman Island (13 dB). Finally, in data scenarios 16-20 there was an optimum packet size for transmission through scintillation fading. The optimum packet size for data 16-20 was 4096 bytes. The packet size optimization was often difficult to realize as the effect of the packet size was often overwhelmed by the larger effects of the received power level and scintillation. However, when the atmospheric effects were not severe there was a definite benefit to a variable packet size.

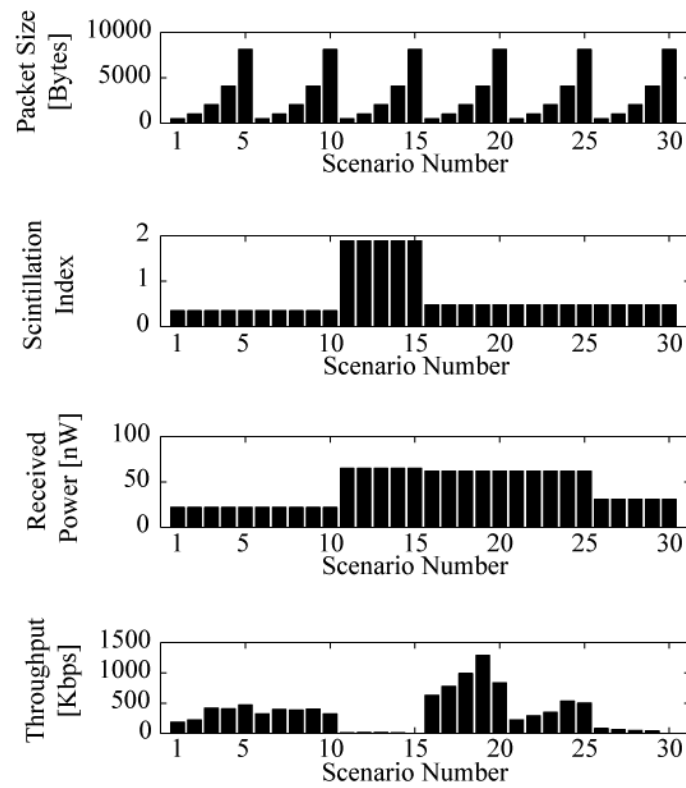


Figure 9.4: Bidirectional data transfer statistics in graphical representation

Chapter 10 Conclusions

A 16 km free-space optical link to a modulated retro-reflector array was achieved using a highly sophisticated interrogator terminal developed by the author. This link was the longest high-data rate MRR FSO link ever accomplished at the time of the writing of this paper. The MRR FSO link was achieved with an array of 3 modulated retro-reflectors interrogated by a bi-static interrogator with active pointing and tracking. Data was transferred across the link with a maximum data rate of 2 Mbps. The author's testing of this link included the demonstration of link acquisition, operation through scintillation, successful pointing and tracking, and various data transmission schemes.

Link performance in the presence of various atmospheric effects was reported. The relationship between visibility and received optical power was demonstrated. Also, the effects of atmospheric scintillation were presented. It was shown that scintillation index values from 0.2 to 2.2 were typical on this FSO link and that the scintillation index could be as high as 3.6. Spatial diversity in the MRR array was demonstrated to reduce the adverse effects of scintillation.

The prevailing atmospheric turbulence induced angle of arrival error was measured and presented. The angle of arrival error due to atmospheric scintillation typically had a standard deviation of 25 μrad . It was demonstrated that the active tracking system could reduce the angle of arrival error to 8 μrad .

Active pointing and tracking was demonstrated on this FSO link. The sensitivity of quadcell circuit designed by the author was sufficient to allow *in situ*

controller optimization of the tracking system. It was shown that the closed loop bandwidth of the pointing system was 175 Hz. It was also shown that the closed loop bandwidth of the tracking system was 125 Hz. The synchronization of the transmitter pointing with the receiver tracking was demonstrated with a coupling bandwidth of 30 Hz. Hence, the pointing and tracking system designed and implemented by the author was demonstrated successfully on the 16 km link.

In total, this 16 km FSO MRR link was a tremendous success. At the time of the writing of this paper, this link was the longest FSO link to a MRR (data rate > 1Mbps) that had ever been completed. The successful operation of this link provided many important link parameters required to develop longer more reliable MRR FSO links. Finally, it was demonstrated all the required functionality of the FSO terminal designed by author performed to the specifications laid out the author for successful link operation. No systems were ineffective and all performed as designed by the author.

Appendix A

Listed in this appendix is the Matlab code for the link diffraction calculation.

```
%%%%%%%%%%  
  
%Script      Range_Loss.m  
  
%  
  
%Org:        LPS UMD ECE  
  
%Author:     Mark Plett  
  
%Updated:    2/1/07  
  
%  
  
%Description:      Script to calculate diffraction range losses  
  
%  
  
%Outputs:          H - Movie of return beam on RX aperture over fringe  
  
%                  TL – TX Range Loss  
  
%                  RL – RX Range Loss  
  
%  
  
%%%%%%%%%%  
  
clear all  
  
k=2*pi/1.55e-6;      %wavenumber [1/m]  
  
R=2500;              %8 inch 100 microrad div [m]  
  
S=0.3;               %Array separation [m]  
  
l=4;                 %Grid size [m]  
  
for j=1:16           %loop over fringe motion
```

```

dx1=0.005

x1=-1:dx1:1;

dx2=1/max(x1)*1.55e-6*16000/2;

[X,Y]=meshgrid(x1,x1);


%8 inch projection aperture

TX_Aperture=[(X.*X+Y.*Y)<0.1^2];

TX_Aperture=TX_Aperture.*[(X.*X+Y.*Y)>0.03^2];

TX_Aperture=TX_Aperture.*exp(i*k*(X.*X+Y.*Y)./2./(R));


%Calculate TX footprint

TX_Footprint=fftshift(abs(fft2(TX_Aperture)).^2);

TX_Footprint=TX_Footprint./sum(sum(TX_Footprint));


x2=x1./dx1.*dx2;

X=X.*dx2./dx1;

Y=Y.*dx2./dx1;


%Generate Array Structure

Y_off=S/2*sin(30/180*pi);

X_off=S/2*cos(30/180*pi);

Phase=(j-1)/16*4*pi/2;           %Phase shift for array motion

Array1=exp(i*Phase).*[((X-X_off).^2+(Y-Y_off).^2)<0.008^2];

```



```
Array2=exp(-i*Phase).*[((X+X_off).^2+(Y-Y_off).^2)<0.008^2];
```

```
Y_off=S/2;
```

```
Array3=[((X).^2+(Y+Y_off).^2)<0.008^2];
```

```
Array=Array1+Array2+Array3;
```

```
clear Array1 Array2 Array3
```

```
%Calculate reflection off array
```

```
Reflection=TX_Footprint.*Array;
```

```
%Calculate TX range loss
```

```
TX_Loss=10*log10(sum(sum(abs(Reflection))))
```

```
%Calculate return beam
```

```
RX_Footprint=fftshift(abs(fft2(Reflection)).^2);
```

```
RX_Footprint=RX_Footprint./sum(sum(RX_Footprint));
```

```
dx3=1/max(x2)*1.55e-6*16000/2;
```

```
x3=x2.*dx3./dx2;
```

```
X=X.*dx3./dx2;
```

```
Y=Y.*dx3./dx2;
```

```
%8 inch telescope collection aperture
```

```
RX_Aperture=1*[((X).^2+(Y).^2)<0.1^2];
```

```
RX_Aperture=RX_Aperture.*[((X).^2+(Y).^2)>0.03^2];
```

```

RX_TX_Offset=0.22;

RX_Footprint=circshift(RX_Footprint,[0 floor(RX_TX_Offset./dx3)]);

%Calculate range loss

RX_Loss=10*log10(sum(sum(RX_Aperture.*RX_Footprint)))

%Cutout the relevant portion of the beam from plotting

subset=min(find(abs(x3)<0.4)):max(find(abs(x3)<0.4));

RX2=RX_Aperture(subset,subset);

Spot2=RX_Footprint(subset,subset);

%Plot return beam on RX aperture for movie

figure(2),set(gcf,'Renderer','zbuffer');

surf(Spot2.*RX2),shading interp,view(2)

colormap(gray)

axis square,axis off

H(j)=getframe;

TL(j)=TX_Loss;

RL(j)=RX_Loss;

end

%End of Range_Loss script

```

Appendix B

Listed in this appendix is the Matlab script for calculating quadcell noise.

```
%%%%%%%%%%%%%%%%%%%%%%%%%%%%%%%%%%%%%%%%%%%%%%%%%%%%%%%%%%%%%%%%%%%%%%%%%%  
  
%Script      quad_noise.m  
  
%  
  
%Org:        LPS UMD ECE  
  
%Author:     Mark Plett  
  
%Updated:    2/1/07  
  
%  
  
%Description:      Script to calculate quadcell SNR  
  
%  
  
%Outputs:          SNR - Quadcell SNR  
  
%  
  
%%%%%%%%%%%%%%%%%%%%%%%%%%%%%%%%%%%%%%%%%%%%%%%%%%%%%%%%%%%%%%%%%%%%%%%%%%  
  
clear all  
  
%Physical Constants  
  
q=1.6e-19;      %Electron charge  
  
R=0.9;          %InGaAs responsivity  
  
OMI=0.15;       %Tone OMI  
  
P=0.2e-9;       %Input light  
  
B=40e-9;        %Background Light  
  
Id=1e-9;        %Dark current  
  
k=1.38e-23;     %Boltzmann's Constant
```

```

T=300;          % Temperature

%Frequency Span

Wo=2.*3.14.*20000;

dF=1;

F=10:dF:1000000;

s=2*3.14*(F);


%Electronics Constants

F_gbp=;        %Gain Bandwidth Product of TIA

Cd=;           %Detector Capacitance

Rd=;           %Detector Shunt Resistance


Cf=;           %Feedback Cap

Rf=;           %Feedback Resistor

Cc=;           %Coupling Cap between Detector and TIA

Cout=;         %Cap to ground on output for LPF

Rout=;         %Series resistor on output for LPF


In=()^2;       %Current Noise Density

Vn=()^2;       %Voltage Noise Density

Is=2.*q.*(R.*(P/4+B/4)+Id); %Shot noise

If=4.*k.*T./Rf; %Thermal Noise


%Shot noise circuit filter

```

$$H1 = (R_f / (1 + s \cdot C_f \cdot R_f)) \cdot (s \cdot C_c \cdot R_d) / (1 + s \cdot R_d \cdot (C_c + C_d)) \cdot (s \cdot R_{out} \cdot C_{out} / (1 + s \cdot R_{out} \cdot C_{out})).^2;$$

% Thermal Noise Filter

$$H2 = (R_f / (1 + s \cdot C_f \cdot R_f)) \cdot (s \cdot R_{out} \cdot C_{out} / (1 + s \cdot R_{out} \cdot C_{out})).^2;$$

% Op-amp current noise filter

$$H3 = (R_f / (1 + s \cdot C_f \cdot R_f)) \cdot (s \cdot R_{out} \cdot C_{out} / (1 + s \cdot R_{out} \cdot C_{out})).^2;$$

% Op-amp voltage noise filter

$$H4 = ((1 + R_f / (1 + s \cdot C_f \cdot R_f)) / (R_d / (1 + s \cdot C_d \cdot R_d) + 1 / s / C_c)) \cdot (s \cdot R_{out} \cdot C_{out} / (1 + s \cdot R_{out} \cdot C_{out})).^2;$$

% Signal Filter

$$H5 = R_f / (1 + W_o \cdot C_f \cdot R_f) \cdot (W_o \cdot C_c \cdot R_d) / (1 + W_o \cdot R_d \cdot (C_c + C_d)) \cdot (W_o \cdot R_{out} \cdot C_{out} / (1 + W_o \cdot R_{out} \cdot C_{out}));$$

% Apply gain-bandwidth limitation of op-amp

$$H1 = H1 \cdot (F_{gbp} / (s + F_{gbp})).^2;$$

$$H2 = H2 \cdot (F_{gbp} / (s + F_{gbp})).^2;$$

$$H3 = H3 \cdot (F_{gbp} / (s + F_{gbp})).^2;$$

$$H4 = H4 \cdot (F_{gbp} / (s + F_{gbp})).^2;$$

$$H5 = H5 \cdot F_{gbp} / (s + F_{gbp});$$

% Anti-aliasing Filter MAX274 Filter

$$H6 = 2 \cdot 3.14 \cdot 25000 / (s + 2 \cdot 3.14 \cdot 25000) \cdot s / (s + 2 \cdot 3.14 \cdot 15000);$$

$$H6 = H6 \cdot H6 \cdot H6 \cdot H6;$$

$$H6 = H6 / \max(H6);$$

% Pll Filter

```
H7=2*3.14*20010./(s+2*3.14*20010).*s./(s+2*3.14*19990);
```

```
H7=H7./max(H7);
```

```
%Integrate Noise Sources
```

```
SHOT=sum(Is.*H1.*H6.*H7).*dF
```

```
THERM=sum(If.*H2.*H6.*H7).*dF
```

```
CUR=sum(In.*H3.*H6.*H7).*dF
```

```
VOLT=sum(Vn.*H4.*H6.*H7).*dF
```

```
%RSS Noise Sources
```

```
NOISE=sqrt(SHOT+THERM+CUR+VOLT)
```

```
%Calculate Signal Power
```

```
SIGNAL=P*OMI/4*R.*H5(2000);
```

```
SNR=(SIGNAL/NOISE).^2
```

```
%Plot Transfer Functions
```

```
figure(1)
```

```
semilogx(F,20*log10(H1./max(H1)))
```

```
figure(2)
```

```
semilogx(F,20*log10(H2./max(H2)))
```

```
figure(3)
```

```
semilogx(F,20*log10(H4./max(H4)))
```

```
% End of Quadcell Noise Script
```

Appendix C

Listed in this appendix is the Matlab code for modeling the phase-locked loop.

```
%%%%%%%%%%%%%%%%%%%%%%%%%%%%%%%%%%%%%%%%%%%%%%%%%%%%%%%%%%%%%%%%%%%%%%%%%
```

```
%Function    pll.m
```

```
%Org:       LPS UMD ECE
```

```
%Author:    Mark Plett
```

```
%Updated:   2/1/07
```

```
%
```

```
%Description:    Function to model pll lock-in performance
```

```
%
```

```
%Inputs:    PLL_Kp - short int proportional gain term
```

```
%          No    - Noise standard deviation
```

```
%Outputs:    PHASE_ERR - Pll phase error
```

```
%
```

```
%%%%%%%%%%%%%%%%%%%%%%%%%%%%%%%%%%%%%%%%%%%%%%%%%%%%%%%%%%%%%%%%%%%%%%%%%
```

```
function [t,PHASE_ERR]=pll(PLL_Kp,No);
```

```
%Initialize Variables
```

```
Fs=;
```

```
t=0.0000051:(1/Fs):1.000001;
```

```
PHASE=zeros(size(t));
```

```
PHASE_ERR=zeros(size(t));
```

```
DPHASE=;
```

```
PLL_Ki=2^16-PLL_Kp;
```

```

PLL_Ko=1;

INPUT=1*sin(2*pi*20000*t+2*pi/2);

NOISE=No*rand(size(t));

NOISE=NOISE-mean(NOISE);

INPUT=INPUT+NOISE;


%Main Loop
for k=2:200000

    QC_SUM=sign(INPUT(k));

    if(QC_SUM==0)QC_SUM=1; end;

    LO=sign(PHASE(k));

    if(LO==0) LO=1; end;


% Mixer Phase Discriminator

    Ud=(QC_SUM.*2^7)*(LO*2^7); %2^14 correspondes to pi/2


% Low Pass Filter

    temp1=PLL_Ki*PHASE_ERR(k-1);

    temp2=PLL_Kp*Ud;

    PHASE_ERR(k)=floor((temp1+temp2)./2^16);


% Phase Accumulator

    PHASE(k+1)=PHASE(k)+DPHASE+PLL_Ko.*floor(PHASE_ERR(k)./2^8);

    if(PHASE(k+1)>32767) PHASE(k+1)=-32767+mod(PHASE(k+1),32767);end;

```



```

    if(PHASE(k+1)<-32767) PHASE(k+1)=mod(PHASE(k+1),32767);end;

    %Calculate LO for demodulation

end

T=tf([PLL_Kp/2^16 0],[1 -1*PLL_Ki/2^16],0.000005)

bandwidth(d2c(T))/2/pi

%End pll function

```

Appendix D

Listed in this appendix is the Matlab code for modeling the fast steering mirror controller.

```
%%%%%%%%%%%%%%%%%%%%%%%%%%%%%%%%%%%%%%%%%%%%%%%%%%%%%%%%%%%%%%%%%%%%%%%%%
```

```
%function
```

```
%[A,A_d,B_d,R_d,K]=compensator_model2(d,f,T,GM,Km,kl,kp,ki,kd,LP_P,LP_I);
```

```
%
```

```
%Org:      LPS UMD ECE
```

```
%Author:   Mark Plett
```

```
%Updated:  2/2/07
```

```
%
```

```
%Description:      Function to calculate PID coef and tf models for closed
```

```
%                loop operation.
```

```
%%%%%%%%%%%%%%%%%%%%%%%%%%%%%%%%%%%%%%%%%%%%%%%%%%%%%%%%%%%%%%%%%%%%%%%%%
```

```
function
```

```
[A,A_d,B_d,R_d,K]=compensator_model2(d,f,T,GM,Km,kl,kp,ki,kd,LP_P,LP_I);
```

```
%Calculate mirror parameters
```

```
w=2*pi*f;
```

```
a=d*w;
```

```
b=w*sqrt(1-d^2);
```

```
km=1;      %Place holder for future real DC gain value
```

```
%Calculate mirror model
```

```

A=tf(Km*w^2,[1 2*d*w w.^2]);

%Calculate mirror driver model

Q=tf(2*pi*7500,[1 2*pi*7500]);

Q_d=c2d(Q,T);

%Convert to discrete model (Matlab defaults to ZOH method)

A_d=c2d(A,T);%Does zoh mapping

A_d=Q_d*A_d;

%Calculate Lowpass filter model

F=tf([LP_P/2^16 0],[1 -LP_I/2^16 ],1/200000)

D_d=d2d(F,0.0001);

A_d=A_d*D_d;

%Calaculate Loop gains to null resonance

%Used for simplified modeling commented out for full modeling

%kl=1;

%kp=-A_d.den{1}(2)-2*A_d.den{1}(3);

%kd=A_d.den{1}(3);

%ki=1-kp-kd;

%Compensator

B_num=kl*[(kp+ki+kd) -1*(kp+2*kd) kd];

B_den=[1 -1 0];

B_d=tf(B_num,B_den,T);

```

```

%Close the loop

R_d=feedback(A_d*B_d,1);

%Calculate gain margin

U=allmargin(R_d);

%kl=U.GainMargin(1)/GM; Only used for simple model

%Package loop gains for output

K=[kl,kp,ki,kd];

%Recalculate loop with adjusted gains

B_num=kl*[(kp+ki+kd) -1*(kp+2*kd) kd];

B_den=[1 -1 0];

B_d=tf(B_num,B_den,T);

AB=A_d*B_d;

R_d=feedback(AB,1);

%Normalize coefficients

K(1)=K(1).*K(3);

K(2:4)=K(2:4)./K(3);

return

%End function compensator_model

```

Bibliography

- [1] H. Willebrand, B. Ghuman, *Free-Space Optics*, SAMS, 2002
- [2] V. Chan, "*Free-space Optical Communications*", IEEE Journal of Lightwave Technology, Vol. 24, No. 12, Pg. 4750-4762, 2006
- [3] S. Betti, V. Carrozzo, E. Duca, "*Optical Intersatellite System Based on DPSK Modulation*", IEEE Wireless Communications Symposium 9206, Pg. 817-821, 2005
- [4] A. Biswas, D. Boroson, et al., "*Mars Laser Communication Demonstration: What it would have been*", Proc. SPIE 6105, Pg. 02:1-12, 2006
- [5] D. O'brien, G. Faulkner, "*Integrated Transceivers for Optical Wireless Communications*", IEE Journal of Selected Topics in Quantum Electronics, Vol. 11, No. 1, Pg. 173-183, 2005
- [6] T. Tsumura, N. Komatsu, et al., "*Vehicle to Vehicle Optical Two Way Communication by Use of Laser and Corner*", IEEE Photonics Technology Letters, Vol. 34, No. 1, Pg. 787-790, 1997
- [7] S. Lambert, W. Casey, *Laser Communication in Space*, Artech House, 1995
- [8] D. Boroson, "*An overview of Lincoln Laboratory development of lasercom technologies for space*", Proc. SPIE 1866, Pg. 30-39, 1993

- [9] S. Milner, C. Davis, "*Hybrid free space optical/RF networks for tactical operations*", MILCOM IEEE Military Communications Conference , Pg. 409-415, 2004
- [10] *American National Standard for the Safe Use of Lasers*, American National Standards Institute , ANSI Z136.1, 2000
- [11] *Safety of Laser Products*, International Electrotechnical Commission , 60825-1, 2001
- [12] T. Ebben, C. Varner, et al., "*Pointing, Acquisition, and Tracking Demonstration System for Laser Communications*", Proc. SPIE 2699, Pg. 81-92, 1996
- [13] K. Wilson, "*An overview of the compensated Earth-Moon-Earth Laser link experiment*", Proc. SPIE 2132, Pg. 66-74, 1994
- [14] C. Swenson, C. Steed, "*Low power FLC-based retromodulator communications system*", Proc. SPIE 2990, Pg. 296-310, 1997
- [15] W. Rabinovich, R. Mahon, et al., "*45 Mbps Cat's Eye Modulating Retro-reflector Link over 7 km*", Proc. SPIE 6304, Pg. 0Q:1-11, 2006
- [16] W. Rabinovich, G. Gilbreath, et al., "*Infrared Data Link using a Multiple Quantum Well Modulating Retro-reflector on a Small Rotary Wing UAV*", IEEE Aerospace Conference Proc. 3, Pg. 93-100, 2000
- [17] E. Hallstig, J. Ohgren, et al., "*Retrocommunication utilizing electroabsorption modulators and nonmechanical beam steering*", Optical Engineering, Vol. 44, No. 4, Pg. 1-8, 2005

- [18] W. Rabinovich, R. Mahon, et al., "*Free-space optical communications link at 1550 nm using multiple-quantum-well modulating retroreflectors in a marine environment*", Optical Engineering, Vol. 44, No. 5, Pg. 1-12, 2005
- [19] W. Rabinovich, R. Mahon, et al., "*A Cat's Eye Multiple Quantum-Well Modulating Retro-reflector*", IEEE Photonics Technology Letters, Vol. 15, No. 3, Pg. , 2003
- [20] C. Jenkins, W. Johnstone, et al., "*MEMS actuated spherical retro-reflector for free-space optical communications*", ELECTRONICS LETTERS, Vol. 41, No. 23, Pg. 1-2, 2005
- [21] T. Mikaelian, M. Weel, et al., "*A high-speed retro-reflector for free-space communication based on electro-optic phase modulation*", Canadian Journal of Physics, Vol. 81, No. 1, Pg. 639-650, 2003
- [22] G. Spirou, I. Yavin, et al., "*A high-speed-modulated retro-reflector for lasers using an acousto-optic modulator*", Canadian Journal of Physics, Vol. 81, No. 1, Pg. 625-638, 2003
- [23] D. Rockwell, G. Mecherle, "*Wavelength selection for optical wireless communications systems*", Proc. SPIE 4530, Pg. 27-35, 2001
- [24] L. Andrews, R. Phillips, *Laser Beam Propagation through Random Media*, SPIE, 1998
- [25] R. Pierce, et al., "*Optical Attenuation in Clouds and Fog*", Proc. SPIE 4530, Pg. 58-71, 2001

- [26] B. Flecker, M. Gebhart, et al., "*Results of attenuation-measurements for Optical Wireless channels under dense fog conditions regarding different wavelengths*", Proc. SPIE 6303, Pg. 0P:1-11, 2006
- [27] A. Grieger, C. Ting, et al., "*3.5 micron free-space laser communications*", Proc. SPIE 6304, Pg. 1L:1-9, 2006
- [28] M. Achour, "*Free-space optics wavelength selection: 10 micron versus shorter wavelength*", Proc. SPIE 5160, Pg. 234-246, 2004
- [29] M. Achour, "*Simulating Atmospheric Free-space Optical Propagation Part II: Haze, Fog and Low Clouds Attenuations*", Proc. SPIE 4873, Pg. 1-12, 2002
- [30] E. Korevaar, I. Kim, B. McArthur, "*Debunking the recurring myth of a magic wavelength for free-space optics*", Proc. SPIE 4873, Pg. 155-166, 2002
- [31] A. Arnulf, J. Bricard, "*Transmission by Haze and Fog in the Spectral Region 0.35 to 10 microns*", Journal of the Optical Society of America, Vol. 47, No. 6, Pg. 491-498, 1957
- [32] G. Carhart, M. Vorontsov, et al., "*Atmospheric laser communication system with wide-angle tracking and adaptive control*", Proc. SPIE 5892, Pg. 11:1-15, 2005
- [33] C. Rago, M. Huff, et al., "*Optical path tracking in high scintillation scenarios*", Proc. SPIE 4380, Pg. 261-268, 2001
- [34] M. Oppenheimer, M. Pachter, "*Algorithm Development for Real-Time Control of the Airborne Laser*", Proc. SPIE 4034, Pg. 201-212, 2000

- [35] W. DeShelter, J. Dillow, et al., "*Kalman Filter Tracking*", Proc. SPIE 4376, Pg. 77-87, 2001
- [36] P Merrit, R. Brunson, R. Telgarsky, "*Testing of Tracking Algorithms under Airborne Turbulence*", Proc. SPIE 3706, Pg. 240-248, 1999
- [37] J. Riker, "*Air Force Research Laboratory Program in Active Tracking*", Proc. SPIE 5160, Pg. 143-152, 2004
- [38] A. Gibson, "*Laser Pointing Technology*", Proc. SPIE 4034, Pg. 165-174, 2000
- [39] M. Borrello, "*A Multi-Stage Pointing Acquisition and Tracking Control System Approach for Air to Air Laser Communications*", American Control Conference , Pg. 3975-3980, 2005
- [40] J. Maynard, D. Begley, "*Airborne Laser Communications: Past, Present and Future*", Proc. SPIE 5892, Pg. 1-13, 2005
- [41] M. Gangl, D. Fisher, et al., "*Airborne laser communication terminal for intelligence, surveillance and reconnaissance*", Proc. SPIE 5550, Pg. 92-103, 2004
- [42] M. Guelman, A. Kogan, et al., "*Acquisition and Pointing Control for Inter-Satellite Laser Communications*", IEEE Transactions on Aerospace and Electronic Systems, Vol. 40, No. 4, Pg. 1239-1248, 2004
- [43] D. Begley, W. Casey, et al., "*Proposed near-term, 1 Gbps space laser communications demonstration system*", Proc. SPIE 2699, Pg. 24-37, 1996

- [44] D. Rollins, J. Baars, Mark Plett, et al., "*Installation environments for free-space optical terrestrial communications links*", Proc. SPIE 4635, Pg. 236-247, 2002
- [45] P. Merrit, J. Donaldson, D. O'brien, "*Angular vibration survey of various aircraft*", Proc. SPIE 5087, Pg. 35-45, 2003
- [46] P. Barbier, P. Polak-Dingels, et al., "*Shack-Hartmann wavefront sensing measurements of near-ground propagated laser beams*", Proc. SPIE 3125, Pg. 384-295, 1997
- [47] B. Levine, E. Martinsen, et al., "*Horizontal line of sight turbulence over near ground paths and implications for adaptive optics corrections for laser communications*", Proc. SPIE 3125, Pg. 354-365, 1997
- [48] G. Tyler, "*Bandwidth considerations for tracking through turbulence*", Journal of the Optical Society of America, Vol. 11, No. 1, Pg. 358-367, 1994
- [49] G. Mecherle, R. Carlson, P. Bandera, "*Active Pointing for Terrestrial Free Space Optics*", Proc. SPIE 4975, Pg. 158-163, 2003
- [50] R. Watkins, H. Chen, et al., "*Optical Beam Jitter Control*", Proc. SPIE 5338, Pg. 204-213, 2004
- [51] T. Knibbe, E. Swanson, "*Spatial tracking using an electro-optic nutator and a single-mode optical fiber*", Proc. SPIE 1635, Pg. 309-317, 1992
- [52] G. Franklin, J. Powell, A. Emami-Naeini, *Feedback Control of Dynamic Systems*, Addison-Wesley, 1994

- [53] T. Ho, S. Milner, C. Davis, et al., "*Fully optical real-time pointing, acquisition and tracking system for free space optical link*", Proc. SPIE 5712, Pg. 81-92, 2005
- [54] T. Ho, S. Milner, C. Davis, "*Pointing, Acquisition and Tracking System with Omnivision*", Proc. SPIE 5892, Pg. 219:1-12, 2005
- [55] T. Ho, S. Trisno, C. Davis, et al., "*Studies of pointing, acquisition, and tracking of agile optical wireless transceivers for free space optical communications networks*", Proc. SPIE 5237, Pg. 147-158, 2004
- [56] D. Harvison, B. Hardy, "*Precision Pointing Mechanism for Laser Communication Mission*", Proc. SPIE 2807, Pg. 142-147, 1996
- [57] Q. Wang, M. Giles, "*Coherence reduction using optical fibers*", Proc. SPIE 5892, Pg. 0N:1-11, 2005
- [58] C. Davis, I. Smolyaninov, et al., "*Effect of Atmospheric Turbulence on Bit-Error-Rate in an On-Off-Keyed Optical Wireless System*", Proc. SPIE 4489, Pg. 126-137, 2002
- [59] A. Mendez, V. Hernandez, et al., "*Design and evaluation of a virtual quadrant receiver for 4-ary pulse position modulation/ optical code division access (4-ary PMM/O-CDMA)*", Proc. SPIE 6457, Pg. 0H:1-6, 2007
- [60] Z. Xin, Z. Zheng, et al., "*Performance Analysis of Optical DPSK Modulation for High Speed Satellite to Ground Laser Communications*", Proc. SPIE 5985, Pg. 1F:1-5, 2005

- [61] S. Trisno, C. Davis, "*Performance of Free Space Optical Communication Systems Using Polarization Shift Keying Modulation*", Proc. SPIE 6304, Pg. 0V:1-9, 2006
- [62] S. Trisno, I. Smolyaninov, C. Davis, et al., "*Characterization of a time delayed diversity to mitigate fading in atmospheric turbulence channels*", Proc. SPIE 5892, Pg. 15:1-10, 2005
- [63] A. Majumdar, J. Ricklin, "*Effects of the atmospheric channel on free-space laser communications*", Proc. SPIE 5892, Pg. 0K:1-16, 2005
- [64] L. Wasiczko, C. Davis, "*Aperture averaging of optical scintillations in the atmosphere: experimental results*", Proc. SPIE 5793, Pg. 197-208, 2004
- [65] R. Mahon, W. Rabinovich, et al., "*Coherent effects and aperture averaging in retro-reflected light*", Proc. SPIE 6304, Pg. 1Y:1-11, 2006
- [66] H. Yuksel, C. Davis, "*Aperture Averaging Analysis and Aperture Shape Invariance of Received Scintillation in Free Space Optical Links*", Proc. SPIE 6304, Pg. 1E:1-11, 2006
- [67] N. Perlot, D. Fritzsche, "*Aperture Averaging - Theory and Measurements*", Proc. SPIE 5338, Pg. 233-242,
- [68] E. Korevaar, J. Schuster, et al., "*Description of STRV-2 lasercom flight hardware*", Proc. SPIE 2990, Pg. 38-49, 1997
- [69] L. Thompson, "*Adaptive Optics in Astronomy*", Physics Today, Vol. Dec., No. 1, Pg. 24-31, 1994

- [70] M. Plett, P. Barbier, D. Rush, "*Compact adaptive optical system based on blind optimization and a micromachined deformable membrane mirror*", Applied Optics, Vol. 40, No. 3, Pg. , 2001
- [71] P. Barbier, D. Rush, M. Plett, P. Polak-Dingels, "*Performance improvement of a laser communications link incorporating adaptive optics*", Proc. SPIE 3432, Pg. 93-102, 1998
- [72] M. Abtahi, P. Lemieux, et al., "*Suppression of Turbulence-Induced Scintillation in Free-space Optical Communication Links*", IEEE Journal of Lightwave Technology 12, Pg. , 2006
- [73] C. Moore, H. Burris, et al., "*Free-space high-speed laser communication link across the Chesapeake Bay*", Proc. SPIE 4821, Pg. 474-485, 2002
- [74] M. Suite, C. Moore, et al., "*Steering compensation for strong vertical refraction gradients in a long distance free-space optical communication link over water*", Proc. SPIE 5892, Pg. 1-9, 2005
- [75] S. Bloom, E. Korevaar, et al., "*Understanding the performance of free-space optics*", Journal of Optical Networking, Vol. 2, No. 6, Pg. 178-200, 2003
- [76] D. Rollins, J. Baars, et al., "*Background light environment for free-space optical terrestrial communication links*", Proc. SPIE 4873, Pg. 99-110, 2002
- [77] G. Agrawal, *Fiber Optic Communication Systems*, Wiley, 1997
- [78] A. Makynen, J. Kostamovaara, R. Myllyla, "*Position Resolution of the Position-Sensitive Detectors in High Background Illumination*", IEEE

Transactions on Instrumentation and Measurement, Vol. 45, No. 1, Pg. 324-336, 1996

- [79] K. Bertilsson, E. Dubaric, et al., "*Simulation of a low atmospheric-noise modified four-quadrant position sensitive detector*", Nuclear Instruments and Methods in Physics Research, Vol. , No. , Pg. 183-187, 2001
- [80] R. Best, *Phase-locked loops*, McGraw-Hill, 2003
- [81] S. Haykin, *Communication Systems*, Wiley, 1994
- [82] K. Kiasaleh, "*Beam Tracking in FSO Links Impaired by Correlated Fading*", Proc. SPIE 6304, Pg. 1L:1-11, 2006
- [83] S. Basu, D. Voelz, "*Analysis of a Ground to Satellite Optical Link with a Cooperative Satellite*", Proc. SPIE 6304, Pg. 1M:1-7, 2006
- [84] P. Merrit, S. Peterson, et al., "*Performance of Tracking Algorithms under airborne turbulence*", Proc. SPIE 4376, Pg. 99-106, 2001
- [85] G. Ortiz, A. Portillo, et al., "*Functional demonstration of accelerometer-assisted beacon tracking*", Proc. SPIE 4272, Pg. 112-117, 2001
- [86] C. Chen, H. Memmati, et al., "*Simplified Lasercom System Architecture using a Disturbance-Free Platform*", Proc. SPIE 6105, Pg. 05:1-6, 2006
- [87] B. Jost, K. Carlson, et al., "*Stationary high-bandwidth beacon-tracking lasercom experiments and the evolution to a mobile lasercom capability* ", Proc. SPIE 5550, Pg. 11-19, 2004